The University of Sydney

School of

Aerospace, Mechanical
and Mechatronic Engineering

Influence of Obstacle Location and Frequency on the Propagation of Premixed Flames

Ross Hall BE (Aero)

Supervisors

Prof. Assaad Masri and Dr Sten Starner

ABSTRACT

Turbulent propagating premixed flames are encountered in spark ignition engines, gas turbines, industrial burners, as well as in vented gas explosions. In all these applications, the flame fronts interact with complex solid boundaries which not only distort the flame structure but directly affect the propagation rate in ways that are not yet fully understood. This thesis aims to provide both a quantitative and qualitative understanding of the link between overpressure, flame front wrinkling and turbulence levels generated in the propagating medium. This is an issue of importance for the provision of improved sub-models for the burning rates of premixed flames.

An experimental chamber was constructed where controlled premixed flames were ignited from rest to propagate past solid obstacles and/or baffle plates strategically positioned in the chamber. Laser Doppler Anemometry was used to measure the velocity field and turbulence fields while pressure transducers were used to obtain pressure-time traces. In addition to this Laser-Induced Fluorescence of the Hydroxyl radical is was to image the flame front as it consumes the unburnt fuel captured in the re-circulation zone behind the main obstruction. The thesis reports on the effects of various parameters such as the inclusion of grids and obstructions, blockage ratio, and repeated obstacles to explore possible correlations between the pressure and the flow-fields.

Pressure, velocity and LIF images were correlated and analysed to prove the significance of grid location and number on overall turbulence intensity. Corresponding flow field parameters such as flame front wrinkling, peak overpressure and RMS all combine to conclusively demonstrate their interaction and influence to turbulence intensity. By progressively positioning more grids further downstream, consequent rises in the flow field parameters and the establishment of positive trends indicates the overall significance of kernel development and flow disturbances in relation to turbulence generation.

TABLE OF CONTENTS

TABLE OF FIGURES

TABLE OF TABLES

TABLE OF EQUATIONS

TABLE OF ABBREVIATIONS

CFD	Computational Fluid Dynamics
CMC	Constant Mean Curvature
EM	Electromagnetic
FSD	Flame Surface Density
LDA	Laser Doppler Anemometry
LDV	Laser Doppler Velocimeter
LES	Large Eddy Simulation
LIF	Laser Induced Florescence
Nd: YAG	Neodymium-doped Yttrium Aluminum Garnet
PIV	Particle Imagery Velocimetry
PUVCE	Percussive Unconfined Vapour Cloud Explosion
RANS	Reynolds-averaged Navier-Stokes
RMS	Root Mean Square
SHG	Second Harmonic Generation
UV	Ultra Violent

ACKNOWLEDGMENTS

During the research for this thesis, time was not only dedicated by myself, but more so by my two enthusiastic supervisors Prof. Assaad Masri and Dr Sten Starner. Separately they willingly provided advice and encouragement and collectively they provided development and progress. Assaad was continually able to find new ways to challenge and test the brain while at the same time and quite simply, Sten kept the wheels turning at a laboratory level.

My thanks and appreciation also goes to my fellow combustion researchers in the laboratory, Matt, Robert, James and Pavel. All of whom have not only imparted knowledge and assistance but assurance when the going got tough.

Naturally my family acted as fantastic thesauruses and proof readers, never complaining much about the arduous task at hand. Most of all the continual praise, support and kindred spirit helped one push that little bit further that hopefully resulted in a well constructed thesis.

Finally I thank my friends who were more than willing to offer Matlab advice when it seemed like Matlab no longer worked. I also provide an apology to anyone who had to interact with me during the final few weeks of production.

STATEMENT OF CONTRIBUTION

I assisted Dr. Pavel Yaroshchyk with the initial location and alignment of the LIF system.

I prepared the area surrounding the combustion chamber for an OH&S inspection with help from Dr. Ian Hall.

I performed the optimisation experiments and determined the appropriate changes to the system required to increase the validation rates, accuracy and coherence. This also includes being a guide and mentor for Matt a final year undergraduate student.

I, on several occasions performed, assisted and observed procedures to trouble shoot the LDV and LIF system along with Dr. Sten Starner, Dr. Pavel Yaroshchyk, and Matthew Dunn.

I conducted all the experiments to obtain the results for this thesis with help from the undergraduate student Matt in the collection of the initial pressure results. Also I ordered, installed and tested the new pressure transducers as well as establishing a calibration method.

I compiled and processed the results, including writing all the MatLab codes to do so.

I wrote all the material appearing in this thesis. In addition to this I took all the laboratory photos and draw the diagrams reproduced throughout this thesis.

I conceived all the main arguments appearing in the discussion and conclusion with valuable input from Prof. Assaad Masri

_____   _____

        Ross Hall   Prof. Assaad Masri

1. INTRODUCTION

The 21st century has seen a massive improvement in the field of combustion research due to the continually increasing diagnostic power of advanced laser analysis techniques. However, turbulent combustion is still very complex and many areas of uncertainties remain and require investigation in order to improve the accuracy and efficiency of the mathematical modelling and simulations. Understanding the mechanisms behind a propagating turbulent flame front as it interacts with its surrounding has a myriad of practical applications that extend beyond the simulations. Improvements in these models will result in improved efficiency for propulsion systems powering everything from automobiles and planes to naval and space craft. These developments applied to large scales applications such industrial burners and coal-fired power stations have the potential to reduce emissions, such as green house gasses and other air pollutants that are contributing to global warming. On the topic of safety, detailed prediction of how an explosive deflagration will propagate through a building or room will allow engineers and architects to better design and locate fire escapes as well as hazardous material storage sites. Finally yet significantly in the field of fire suppression systems, engineers will be able to better design and locate protection equipment such that loss of life and property is reduced in explosive situations.

This thesis focuses on turbulent premixed combustion where a long term objective of research is to enable the computation of burning rates, emission characteristics and compositional structure of flames that cover the entire regime diagram [1-13] and may undergo significant interaction with turbulence. Such an objective is gradually being approached by virtue of the recent advances of modelling capabilities and the advent of detailed measurements in well defined laboratory flames [13-17]. Earlier experimental studies in this field focused on large-scale experiments [12, 13, 16, 18-20] which were impractical for detailed diagnostics and which were rather limited to pressure-time histories. More recently, laboratory-scale experiments have become the preferred method of investigation, utilising simple

geometrical configurations that more easily lend themselves to complex diagnostics and subsequent validation of numerical models. Studies have been performed using many vessels, including enclosed cylindrical vessels [2], cylindrical vessels with turbulence inducing rings [14, 21, 22], spiral tubing [23] and circular plate obstructions [17], square vessels with wall baffles [24], and, recently, square cross section chambers with various rectangular, cylindrical and flat plate obstructions [7, 12, 13, 15, 25].

Calculations of turbulent premixed flames are gradually improving with the development of advanced models for the burning rates and powerful numerical approaches such as LES. The flame surface density (FSD) is rather promising in being able to compute finite rate chemistry effects albeit in this flow only [12, 13, 16]. CMC and PDF approaches are also potentially useful in premixed flames calculations over the entire regime diagram but such capabilities have not yet been fully exploited. The challenge remains to develop numerical capabilities for premixed flames covering the entire spectrum of reaction zone structures. This, however, requires that availability of data in relevant flame that lend themselves easily to modelling.

The objective of this thesis is to advance current understanding of turbulent premixed flame propagation with particular focus on the affects of obstacle location and number on flame structure. This thesis specifically expands on work by Hall [7] in 2006, further analysing the factors governing burning rates, flame front velocity, integral length scales and overpressures (relative pressure in the chamber). By using an experimental configuration that lends itself easily to modelling, allow the investigations of turbulent premixed flames propagating past solids obstacles. Such a configuration is also useful for the study of deflagrations and the development of an improved understanding of how the flame front interacts with solid obstacles in an experimentally tractable domain.

This study will further expand the knowledge specifically relating to flames propagating in a turbulent environment [1-4, 6-17, 21, 22, 26-43] thus considering realistic and plausible conditions for fire scenarios. Practically speaking, enclosures where such gas explosions are likely to occur contain obstructions that generate turbulence in the unburnt gases ahead of the advancing flame front. Hence it is

necessary to analyse the stochastic nature of the flow field by generating turbulence in a controlled and experimental environment.

Earlier work [7, 12, 13, 15, 36, 37] focused on a large chamber with a volume of 20 L. Data reported from this chamber reveals the effects of obstacle geometry and blockage ratio on the explosions overpressure and burning rates. It is revealed that obstacles of triangular shapes as well as rectangular cross sections lead to the highest overpressure. The main drawback with this chamber was that its size required very long LES, whick was impractical. The current design marks an improvement over the previous chamber in that the burnt volume is less than 1 litre, and the chamber allows the use of repeated obstacles to generate high levels of turbulence without the risk of deflagration to detonation transition. The small size minimises computational time required for LES, whilst broad optical access is incorporated into the design to facilitate a wide range of experimental diagnostic techniques. Since the work conducted on the chamber used obtain the velocity data in 2006 [7] or Rig 1, further modifications have been made in addition to the aforementioned. These modifications were aimed at reducing errors associated with the fundamental operation of the experiment, such as fixing the displacement of the venting flap and removing all particulate material from the fuel lines. This thesis therefore continues the work started by Kent et al [15]. Current research has concentrated on various obstacle and grid locations never before studied with respect to turbulence levels. Distal and proximal grid placements relative to a consistent obstruction influence a range of key flow field parameters that inturn produce a repeatable and predictable turbulent propagating flame front. Presented is a cross section of flow field data collected from multiple pressure transducers and a two-dimensional Laser Doppler Velocimeter (LDV) system, for a series of configurations. These Configurations were then grouped into families with a logical progression of one or more grids, located downstream away from the ignition point and towards the main obstruction. The experimental setup facilitated the analysis of the effects of geometry, stoichiometry and baffle plate location on peak pressure, velocity and relative turbulence intensity.

Laser-Induced Fluorescence (LIF) imaging was also used to obtain accurate flame front data as the reaction zone interacts with the recirculation region behind the obstacle. These data complement the velocity and pressure data previously collected

further advancing the picture associated with each configuration setup. In order to obtain an acceptable signal to noise ratio, all the LIF measurements were taken in a second identical combustion chamber, but with optical windows suitable for UV light for LIF. The second combustion chamber (Rig 2) had identical internal dimensions to that of Rig 1, whilst maintaining the ability to examine the geometrical variation. For this work two sets of configurations, family 1 and 3 were examined enabling detailed analysis as the flow interacted in the wake behind the small obstruction.

Results are presented for a family of configurations where each family corresponds to a single baffle plate but placed at a different location from the ignition point. Families of cases are studies with one, two and three baffle plates and with a small and large obstruction having a square cross section. The LIF measures are presented in section 6.4 with the pressure and LDV results reproduced in sections 6.1 and 6.3 respectively.

The ongoing research issues arising from Hall's work [7] are primarily concerned with the processing and analysis of the turbulence associated with the flow data. These issues have been considered and improvements made to the overall approach adopted for data processing, specifically relating to LDV results. In addition to this peak overpressure was examined in parallel with expected turbulence levels and compared to both LDV and LIF results in order to obtain proportionality constants.

2. LITERATURE REVIEW

The complex combustion process has been the subject of research for decades in an attempt to better understand the factors influencing the various flow parameters. Recently even more emphasis has been placed on obtaining data specifically for use in establishing and confirming mathematical models and simulations that can predict flow field factors. Improvements in simulations that ultimately come from experimentally verified theories will lead to an efficiency increase across the industry, which will in turn lead to a reduction in greenhouse gasses and air pollutants. Currently several academics across a range of research institutions are working on computational solutions specific to measurements, conducted at Sydney University.

2.1 LAMINAR PREMIXED FLAMES

Laminar premixed flames, are distinctly premixed, diffusion or partially premixed. They are extremely useful in understanding the chemistry and the effects of strain on that chemistry and flame structure. In turbulent flames, some complex processes are introduced such as turbulent mixing, however many modellers make the assumption that the turbulent flame is an ensemble of laminar flames and that these turbulent mixing processes bring together local mixtures which can then react according to laminar flamelet rules. For this reason it is important to understand the principles controlling the reaction zone propagation in standard non turbulent conditions. Also understanding the parameters that influence laminar premixed combustion is crucial in untangling the complexities behind turbulence premixed flames. In both laminar and turbulent flows, the same physical processes are active so much so that most turbulent flame theories are based on underlying principles derived from laminar combustion analysis. For this reason the initial steps into analysing turbulent combustion were the quantitative and theoretical analysis of laminar flow situations. By introducing the stochastic turbulence variable into the laminar flow experimentation, data can also be obtained to examine the instability of the resulting

flame. Considering the flame as a reaction wave, where each element propagated only in a direction normal to the surface, flame curvature can be assessed [38].

Palm-Leis and Strehlow [38] performed a quantitative analysis of flame curvature effect and flame instability in laminar flow situations. This research released in 1982 considers the flame front as a reaction wave. Initially four different experimental cases were considered namely;

1. The wake flame held on a bluff body in a duct
2. Attached turbulent flames on open ports
3. Flat turbulent flames stabilised in flow field
4. The outward propagating spherical flame in a turbulent flow

Combining the results obtained for the turbulent burning velocity in the simplified one dimensional case further provides a better understanding of the complex turbulent characteristics in three dimensional space. These characteristics also qualitatively described laminar premixed flames from which developed a simplified model that allowed analysis of parameters such as flame speed and flame thickness [44]. These then provided a basis for analysing the more complex nature of turbulent combustion. Specifically, the mathematical description of a turbulent flow, and the solution of the resulting governing conversion equations can be studied, however these are much more difficult than for laminar flow.

2.2 TURBULENCE ANALYSIS IN VARIOUS MEDIA

Another effective analysis tools for obtaining turbulence data is to consider a flow field in water rather than air. Although this removes the reaction zone from the experiment, researchers have been able to calculate components of turbulent velocity as the flow interact with grids [45, 46] and vortex tubes [47]. One of the most detailed analyses into velocity profiles behind grid generated turbulence was by Russian scientists Lai, Paka, Delisi, Arjannikov and Khanev [45] where three independent measurement techniques were adopted. The most notable was the electromagnetic (EM) velocity probe that was capable of measuring the three components of oceanic

turbulent velocities. The research proved the data obtained from the EM probes was consistent with that taken from the hot-film and airfoil probes thus improving the measurement techniques available to the turbulence industry. Research moved forward with scientists using a LDV systems [46] to capture flow data and therefore begin to calculate RMS values for turbulence. All of these studies have been crucial in expanding the understanding of the hydrodynamic aspect of turbulent combustion.

2.3 TURBULENT PREMIXED FLAMES

Turbulent flows result when instabilities are not sufficiently damped by viscous action and the fluid velocity at each point in the flow exhibits random fluctuations [44]. By analysing the factors that influence turbulence level in turbulent combustion, more can be identified about the interactions in ephemeral premixed combustion environments. Turbulent premixed flames have a significant practical importance in everyday applications from, internal combustion engines of all shapes and sizes to industrial burners and boilers. In most applications of premixed combustion the medium through which the flame is propagating is highly turbulent due to various obstructions impeding the flow. The highly stochastic nature of the flow means the reaction zone or flame front has significantly increased thus increasing the burn rates and velocity from equivalent laminar flows.

Turbulent combustion also extends to gas or flammable liquid vapour cloud explosions in both domestic and commercial situations. With fuel and air in the right proportions, a gas leak can be ignited extremely easily resulting in the phenomenon know as a PUVCE, or Percussive Unconfined Vapour Cloud Explosion. By predicting how the explosion will interact with the surrounding environment, the excessive amounts of heat and the destructive shock wave can be manipulated, saving life and property. Several publications have been printed on the topic of turbulent combustion [1-8, 10-17, 20, 21, 23, 24, 26, 28-31, 33, 35-43, 45-59] which analyse the various aspects of the combustion parameters. This research combines with results from computation data to provide a better physical and mathematical understanding of the concepts that influence the turbulence levels. Superior understanding of time

dependant flow characteristics in the study of turbulent gaseous explosions is of obvious practical and of fundamental interest [60].

The factors that influence the intensity of the turbulence and overpressures are considered from past research and expanded on within this thesis. The generation of turbulence is achieved by directing the flow around solid obstacles [3, 7, 12, 13, 21, 36, 37, 41, 48, 61], through grids [3, 7, 12, 13, 21, 26, 31, 36, 37, 41, 45, 46, 48, 62, 63], fan-stirred bombs [29, 64], and counter rotating fans [43] as well as specific apparatus such as a Taylor-Couette apparatus with counter rotating cylinders [4, 58]. All of these consider the parallels between turbulence and the relative dependencies of specific combustion parameters with the view of deriving a mathematical theory suitable for turbulent combustion.

2.3.1 Solid Obstructions

In order to simulate realistic conditions a solid obstacle is placed in the direct path of the propagating flame front. As the flow interacts with the obstruction the flow parameters are changed as the flame front becomes contorted and the flow turbulent. Data can then be obtained relating the effects of varying geometry and relative blockage ratio to that of burn rate and over pressures. Over the past decade researchers at the University of Sydney have investigated the specific effects of obstruction geometry [7, 12, 13, 36, 37, 48] in order to examine and then predict the effects of a gas explosion. The geometry of the obstruction initially included circular, triangular and square cross sections [13] and was expanded in [12] to incorporate diamonds and plates or walls. These experiments were able to examine the mechanisms which enhance explosion overpressures by studying flame structure and acceleration through the use of pressure transducers and high speed video imagery. The result confirmed that the flame speed was found to significantly increase with the increase in flame surface area, brought about by the turbulent fragments in the flame front.

Geometry, as well as blockage ratios and venting pressure were all examined in relation to overpressures resulting from premixed flame deflagration in [12]. With

blockage ratios from 10% to 75%, it was found that several parameters are directly proportional. An increase in the deflagration overpressure resulted in corresponding increases with increasing venting pressure. Also proportional, is that the maximum overpressure increases, with increasing blockage ratio, however the rate of change depends on the geometry of the obstruction.

These results combine with laser induced fluorescence (LIF) images of the hydroxyl radical OH and particle imagining velocimetry (PIV) [37] to further expand the flow field data. A detailed comparison between the images from the LIF - OH and the burning rates calculated using Large Eddy Simulation (LES) highlighted the extent to which the flow contorts around the obstruction. The laser techniques used for flow imaging are discussed further later in this chapter.

The transient interactions of flame fronts with obstacles were also considered by Linstedt and Sakthitharan to be a key phenomenon in determining the severity of turbulent gaseous explosions [60]. This work, along with [65] by Phylaktou reinforced the findings that the influence of obstacles was to increase flame speed, increase rate of pressure rise, shorten the duration of the explosion and give a higher maximum pressure. Finally in other work by Parka *et al* [61] the effects of alternately shaped obstructions are examined in relation to propagation properties of a flame front. Similarly to work performed at the University of Sydney, four different single obstructions were used, namely; triangular, circular, square and rectangular cross sections with blockage ratios of 5 and 10%. In this case is was found that for different blockage ratios and constant obstacle cross section no significant change was observed in relation to flame displacement speeds. A comparable result was obtained when the cross section was varied and in fact the flame propagating speed remained close to the laminar burning velocity.

2.3.2 Grid Generated Turbulence

In most cases analysis of flow fields' interaction with solid obstacles occurs in conjunction with an arrangement of grids or baffle plates up stream to increase turbulence levels. Not all cases examined a transient propagating flame process as in

the work by Hall [7] and others at the University of Sydney [3, 12, 13, 36, 37], however a series of grids is still utilised for the production of the turbulent flow. In [46] Shy, Tang and Fann use a pair of vertically oscillating grids to create a region of turbulence that is almost equal and stationary in all directions with in fluids contained in a water tank. In many non-transient flows, grids are used to generate turbulence that can be considered isotropic or homogeneous as above in [4, 46], which introduces further boundary conditions thus simplifying the computation.

One of the earliest studies into modern premixed combustion in a turbulent atmosphere was by Ballal [26] from the Cranfield Institute of Technology in 1978. In this study a large 250×200 mm combustion chamber, similar to that adopted by Masri *et al* [12, 13, 16, 37] was used in conjunction with a range of varied parameters to investigate changes in the flow field. A variety of grid geometries, turbulence intensity scales and approach scales were altered independently to examine the effects for turbulence on a propagating flame. This work found that strong links exist between the mechanisms of turbulence flame propagation and flame-generated turbulence. These flow properties are now forming the basis of turbulence models and are continually being researched [7, 36, 37, 57] to further develop the theory and thus improve the computational simulations.

2.3.3 Rotating Cylinders (Taylor-Couette Apparatus)

The Taylor-Couette apparatus consists of two counter rotating cylinders inside one another that are capable of up to 3450 revolutions per minute. In research conducted at the University of California [4], the described apparatus was used to generate turbulence that was nearly homogeneous and isotropic over many integral lengths and time scales.

It was found that turbulent-flame propagation in high intensity was not influenced by the factors such as Darrieus-Landau instability and heat loss to the walls of the apparatus which influence laminar flame propagation. Also, interestingly, the report considers heat release and the transition to a non-flamelet combustion regime influenced by large scale flame-front wrinkling.

2.3.4 Fan Induced Turbulence

Another technique used to analyse premixed turbulent gaseous explosions is in an explosion bomb. The combustion chamber in this case is a 380 mm diameter stainless steel sphere, or bomb, capable of withstanding the pressures and temperatures generated through out the experiment. The fan-stirred bomb showed that mass burning rate depended upon the product of area, density and burning velocity, while the flame brush thickness increased with flame radii [29, 43, 52]. In a continuation of the experiment, premixed isooctane and methane air flames were ignited at 1 and 5 bar and a range of fan speeds to assess and derive calculations of flame curvature, turbulent flame curvature and wrinkling [52]. This also included investigation of non-stabilised flames ignited under laminar and turbulent conditions.

2.4 VELOCITY MEASUREMENT TECHNIQUES

Over the history of fluid mechanics research many techniques have been adopted to obtain accurate flow field measurements. These include Hot-film Anemometers [31, 45, 51, 58], the Bomb Method [64], Ion-probe Sensors [43], Thermocouples [21], High Speed Video [13, 36, 48] and more recently utilising Laser Diagnostics [3, 7, 32, 37, 41, 46, 48, 49, 55-57, 62, 66-72]. One of the major difficulties in determining fluid velocity is that the early techniques were intrusive and hence interfered with the flow thus to an extent discrediting the data. Rapid flame and pressure development in accidental explosions accelerated the drive for more accurate analysis techniques that didn't corrupt the flow field. This also gave a basis to treat the ultimate coupling between flows, turbulent heat release, mixing and pressure rise by use of sub-models for each of the elementary processes [35]. Gaining insights into turbulence intensity and thus being able to calculate the turbulence level of both the stream-wise and normal component velocity became possible with the various advanced laser diagnostic techniques.

2.4.1 Hot-film Anemometers

Hot-wire and film probes were utilised in [31, 45, 51, 58] to measure the characteristics of the flame front curvature and velocity statistics of turbulent premixed flows. A hot-wire anemometer is able to measure the velocity of a fluid by noting the heat convected away. This heat loss to fluid convection is then proportional to the velocity of the fluid and transmitted into the medium in accordance with convective theory [73]. However these measurements can only be performed in the cold regions of the flow. Measurements of the stream-wise integral length scale and root mean square of the velocity are compared to that of the normal component obtain at the exit of a plate array in work by Guillaume *et al* [51]. This was preformed to ascertain the dependence of the wrinkle scale of propane–air turbulent premixed flames on the flame curvature as the flow is traversed through a pipe with various modifications. Estimates of strain rate in the unburnt gases [31] and the velocity [58] can be deduced with a hot-wire anemometer both with and with out combustion taking place. The aforementioned turbulent burning velocities are then compared with theoretical correlations [58]. While in work by Lai *et al* [45] the velocity obtained by the hot-wire probe is used to calibrate and confirm results taken by experimental EM probes capable of measuring velocity in three dimensions.

2.4.2 Particle Image Velocimetry

Particle Image Velcoimetry (PIV) is an invaluable non-intrusive optical technique for collecting velocity and other flow properties of a fluid. Using a high powered double pulsed laser, a light sheet is created inside the measurement section that laminates the seeding particles, which can then captured on a digital camera. Velocity of an individual particle is deduced for the relative particle displacement over the time delay between the successive images. The images are then able to be analysed in this way for every particle passing through the location to create an accurate mean velocity of the medium as well as velocity profile of the entire measurement section. The technique has been utilised in fluid dynamics research for

over 20 years with multiple applications in combustion research from a variety of institutions [3, 36, 41, 48, 49, 56, 57, 70].

Work into flame front shape and velocity profiles were examined at Cambridge University in the decade leading up to the work described at Sydney. This work [49] looked at turbulence levels in front of the flame front and found that the effects of turbulence were greatly increased when the explosion was confined. A laser sheet formed by multiple reflections between two concave mirrors was used to illuminate micron-sized silicon oil droplets [41, 49]. Computational Fluid Dynamics (CFD) was then applied to the turbulent diffusion flame combustion, however this predictive technique was found to be inadequate when compared to the experimental data, which has fuelled further research into turbulent dynamics. Development of a high speed laser sheet flow visualisation technique was undertaken in the early 1990's at the University of Leeds. This was able to characterise the interactions between flame and multiple solid obstacles causing an increase in translational flame speed with the number of obstacles [41].

One of the advantages of PIV measurements over the aforementioned is that relative accurate data correlating flame front shape and length to burning velocity can be obtained. In work by Cadwallader *et al* [48], PIV measurements are collected simultaneously with pressure-time traces and high speed camera images as a flow passes over solid obstacles and turbulence generating grids. It was concluded that obstacles and turbulence generating grids in the flame path led to higher over-pressure and flame speeds, as well as faster gas velocities. The experiment was very repeatable and hence consistent results could be obtained, thus correlating accurate data for flame wrinkling that was linked to burning velocity and overpressures. These are found to all be effected by the generated turbulence as the PIV is able to map the flow field in the selected region.

Continuing the work outlined above, Masri *et al* [37] performed an experimental and numerical study of turbulent pre-mixed flames propagating past solid obstacles. In this case particular emphasis was placed on the burn rate and structure of the flame front more than the geometry and blockage ratio. This research again utilised PIV measurements however this time simultaneously with laser induced

fluorescence images of the hydroxyl radical OH^{-} to give further insight into turbulent flame front shape. Several modifications occurred before the 2005 publication, namely the volume of the combustion chamber was reduced in order to increase the velocity and therefore Reynolds number, however a glow plug was still the ignition source. These changes to the experimental setup have been adopted into all turbulence premixed combustion research at The University of Sydney [7, 36]. The modifications were found to produce more accurate and repeatable results. A high speed camera was again used to collect simultaneous flow measurements with these results being published in detail in Kamardin's thesis [36].

A problem addressed with corresponding LIF images is the location of the flame front or reaction zone. With both PIV and LDV measurements that are relying on the particulate material suspended in the flow to obtain data, the location of the flame front is unclear. Researches began taking simultaneous high speed camera images [37], however the results acquired using this method only reveal approximate flame location due to available resolution and set up. The use of OH LIF images adds to the information that can be deduced from PIV images, namely the definition between burnt and un-burnt regions in the combustion chamber [3, 56, 57]. These results show a sharply defined edge between burnt and un-burnt regions of the transient flow as it traverses a series of baffle plates and an obstacle. Kent *et al* [3] used computational methods of describing the wrinkling scales present in a controlled flame front while identifying the relationship between flame structure, flame surface density and turbulence intensity. The method provided a quantifiable means to relate the changes in instantaneous flame front structure (contortion) with changes in turbulence levels using the instantaneous imaging. However, due to the finite timescales involved, even with the laser imaging velocity measurements it was difficult to obtain any degree of accuracy [3].

2.4.3 Laser Doppler Velocimeter

The use of LDA or LDV in a transient premixed flame has further expanded the laser analysis techniques available to the industry by being able to provide additional flow data to that achieved by Particle Imagery. A LDV system has the main advantage that continuous and accurate flow field data can be collect for any given location in the measurement section. Although only a single location is examined for any given run, data collected by a LDV system can only be used to develop flow field results for a single point in time, and hence coupling the two systems provides a unique data collection resource.

A dual-beam fringe anemometer is the most common optical arrangement for systems such as Laser Doppler Velocimeter, where two equal intensity light beams intersect at a mutual focal point [65]. These beams interfere and superimpose creating an interference pattern (regions of light and dark) such that when a particle crosses these fringes the intensity of the scattered light varies generating a Doppler burst. Therefore the measured frequency difference, V_D, is directly proportional to the instantaneous component of the velocity of the particle lying in the plane of the beams and normal to their bisector, u [65]. The equation is reproduced below (equation);

$$v_D = 2 \frac{u \sin\left(\dfrac{\theta}{2}\right)}{\lambda}$$

Equation 2.1: Frequency Difference [65]

where λ is the wavelength of the incident laser beam and θ is the beam intersection angle.

Using laser optical investigation techniques the turbulent transportation of temperature ahead of the preheated zone in a premixed flame can also be analysed. The work carried out by Kortischik, Plessing, and Peters [55] used Laser Doppler Anemometry (LDA) and proposed that a turbulent Eddy is a statistical concept rather than a physical entity and that turbulence is intermittent and stochastic.

One of the major problem encountered by Hall [7] in 2005 was the difficulty in seeding the flow to facilitate the collection accurate and comprehensive data. As outlined above both the PIV and the LDV systems require particulate material to be suspended in the flow in order to obtain results. For velocity measurements to be obtained by using a laser optical investigation technique, the particulate material is assumed to move with the flow, not move independently, thus providing flow data. Consequently the accuracy of any given experiment is limited to the amount of seed and the resulting seeding rate repeatability and consistency. For many researchers the issues arising from the use of particulate material have less effect due to the process having an infinite time scale and therefore a high seeding rate is not essential.

In the case of transient turbulent combustion as in [7] the time scale becomes important and thus the type of particulate material and the seeding rate become crucial to the accuracy of the results. All the research thus far at the University of Sydney has used sub-micro aluminium oxide particles to seed to combustion chamber [3, 7, 37, 48]. An alternative source of seeding particles namely Silicon Oil, which has been employed by Chew [49] at Cambridge University. Silicon oil smoke particles were used as seeding for the LDV system to obtain a direct comparison for the turbulent burning velocity to the flame perimeter ratio as the flow propagates. Flame wrinkles in 3D are found to be associated with larger flame surface area than that determined from the flame perimeter ratios data. Interestingly, the research shows how the global flame curvature develops due to heat loss at the wall responsible for lowering the flame speed. However this was a technique which was successful for applications that are time independent.

Turbulent premixed combustion is a dynamic process, and involves complex interactions between turbulence and combustion chemistry. The industry has been continually evolving and diversifying in the attempt to understand the nuances of the complex combustion process. Following on from the work already conducted by Hall [7] in 2006, the experimental procedure and results are further expanded to delve deeper into the natural and characteristic of turbulent combustion. Using the results obtained from the two dimensional LDV system the results are re-processed to maximise the data's potential and extract all relevant flow field information.

Ultimately the results will continue to add to the global archive of knowledge and advance the development of computer simulation accuracy.

2.4.4 Characteristics of Velocity Measurements Methods

Each of the aforementioned velocity measurements techniques have advantages ideal for specific applications. Work conducted by Yamamoto *et al* [70] in Japan was able to validate PIV measurements by direct comparison with LDV data. Using PIV reliable data was collected, particularly in relation to sampling number and spatial resolution. The research [70] suggested that in order to determine statistical quantities such as mean velocity and RMS of velocity fluctuations, a sampling number of 1000 was required which is also supported by Hall [7]. Shown below is a comparative table linking the attributes for three data collection techniques namely Hot-wire anemometry, PIV and LDV.

	Advantage	Disadvantage
Hot-wire Anemometer	• High resolution of time • Not expensive	• Intrusive • Not for combustion field • Point measurement
Laser Doppler Velocimeter	• Non-intrusive • High resolution of time and space	• Point measurement • Seeding particless • Expensive
Particle Image Velocimetry	• Non-intrusive • 2D measurement	• Errors ingrained • Seeding particles • Very Expensive

Table 2.1: Characteristics of measurement Methods [70]

2.5 LASER-INDUCED FLUORESCENCE

Laser-Induced Fluorescence is used to detect specific species for flow visualisation and measurement purposes. The spectroscopic method examines a specific molecule that is excited by the laser sheet fired into the measurement section. The excited species spontaneously de-excites and emits light at a wavelength larger than the excitation wavelength [34, 74, 75]. This light or fluorescence is then collected by a digital camera for analysis. The technique is successfully applied to obtain quantitative measurements of concentrations and therefore is able to show the flame front location. LIF is now used extensively [32, 34, 36, 37, 56, 57, 62, 66-68, 71, 72, 75] to obtain accurate data relating to flame wrinkling and flame front length scales as well as temperature and pressure. As this analysis method does not give results relating to flow field velocity, it is frequently used in conjunction with either PIV of LDV measurements. In this thesis the velocity results of Hall [7] have been re-processed and combined with LIF images collected separately to further expand the available data relating to turbulence levels in premixed transient combustion.

Previously at the University of Sydney [32, 37, 67], LIF of both the hydroxyl radical OH and N_2 have been used and developed to study the structure of the flame front. In [32, 67] Chen *et al*, laser measurements of three-dimensional flame-front structures for turbulent lean burning Bunsen flames are discussed. Since the flame residence time relevant to the turbulent flames present is smaller than the unstretched laminar value, the combustion regime diagram can't be used. The research was able to show that the anisotropic local flame-front orientation is biased by the forward propagation of the turbulent flame brush. This then implies that regarding the front surface of a turbulent flame front as a passive surface is incorrect [67] but that the local flame front orientation in three dimensional space is close to an isotropic distribution as the surface wrinkling in nonpassive [32].

In one of the first experiments examining transient turbulent premixed combustion at The University of Sydney, Masri *et al* [37] put particular emphasis on the burning rate and structure of the flame front. In this case High-speed images, PIV and OH – LIF again collected separately, were used for a range of flame propagating

conditions. An array of baffle plates and various geometrical obstructions provided a myriad of turbulence levels for examination similar to that used by Kamardin [36] and then Hall [7] but on a larger scale. Modifying the combustion chamber by reducing the dimensions alowed greater turbulence levels to be generated as well as several other advantages that are outlined in [7]. Utilising the LIF images, a significant degree of interaction between the flow and the propagating flame front was found. The higher turbulence levels were found to be induced by vortical structures that then increased burning rates and hence the overpressure at a rate faster than the flame speed [37]. This will be re-examined to an extent with the new combustion chamber with the results being used to qualify LES simulations.

Due to the increasing performance of mathematical simulations that can now numerically describe the effects of turbulence, the demand for high quality flow data in rising. Several researchers have looked into the specific accuracy and repeatability of laser-bases methods to obtain the required information without severely disturbing the observed effects whilst maintaining the needed temporal and spatial resolution [34, 75]. New developments in technology affect all aspects of laser-based combustion research, which in turn affects measurements techniques, implementations, applications and problems.

2.6 COMPUTATIONS

In today's modern age, prediction is the key to successful engineering, trial and error techniques have long since been replaced with computational simulation and analysis. For combustion, this means improving turbine efficiency by a fraction of one percent, it means predicting smoke movement in a structure fire and it means designing safety equipment that saves lives in the event of a fire or explosion. The stochastic nature of turbulent combustion has hindered the advancement of combustion models until now with the advancement of laser diagnostic techniques outlined above. Many researchers [6, 16, 28, 30, 32, 34, 37, 50, 54, 59, 75-78] work closely with modellers to follow the process from the lab to the final result.

The prediction of turbulent combustion is classically performed by numerical integration of modelled equations. For this the crucial quantities are the time scale for the destruction of temperature or concentration fluctuations [28]. This considered several proposed equations with the assumption that the time scale was simply proportional to the corresponding time scale fluctuations in the in velocity profile. For turbulent or wrinkled flames it was stated that the reaction doesn't play a significant role in effecting the time scale.

Predictions of turbulent premixed flame propagation in explosion tubes were used by Catlin *et al* [30] to developed a mathematical model capable of predicting the over-pressures generated by gaseous explosions. The combustion process was described and developed using a semi empirical method which admitted both chemical kinetics and flow field influences [30]. This was done whilst still maintaining a realistic flame thickness throughout the flame propagation and therefore nearer the experimental conditions. The opposing method of assessing the model through the numerical simulations of properties of turbulence in premixed flames was conducted at Michigan University [50]. Several properties of turbulent premixed flames were measured including, local stretch rates, wrinkling, flamelet extinction and the turbulent burning velocity of Bunsen flames. The effect of eddies on flame lengthening was combined to provide data for future assessment of the direct numerical simulations and models.

Similarly, numerical data for the thickness of the instantaneous flamelets in a turbulent flame brush on a weak-swirl burner was compared to experimental and theoretical data [6, 59]. For this Goey *et al* [6] used correlated images of both OH-LIF and Rayleigh scattering to measure the flame thickness. From analysis of the numerical, theoretical and experimental data that the low temperature edge of the flame was thickened by the presence of turbulent eddies, yet these structures do not penetrate the inner layer. This means that the inner layer of the flame front was not distorted by the production of eddies along the low temperature flame front.

A comparison between the recorded flow data and the burn rates calculated using Large Eddy Simulation (LES) was also considered by Masri *et al* [37]. It was concluded that the simulations are consistent with the experimental data considering

the simplicity of the combustion model used [37]. Turbulence levels were also shown to increase notably as the flame front propagated past the array of baffle plates and the obstacle. Finally, with the use of the laser imaging of the hydroxyl radical OH, Masri *et al* was able to show a significant correlation with the integration of the flow and the propagating flame front. This research was able to reinforce the past works, conforming that higher turbulence levels increase the burning rates and hence the over-pressure, yet the turbulence levels were still to be quantified.

On the topic of global warming researchers at the University of Japan are specifically examining turbulent premixed combustion [54] to help reduce emissions of carbon dioxide and nitrogen oxide. Usually lean combustion of hydrogen or methane air mixtures is adopted to diminish the greenhouse gas production by achieving more complete combustion. In order to accomplish this, researchers must establish connections between physical flow parameters in a turbulent environment to be able to provide accurate data for simulation purposes. The particular work by Kadowaki [54] found that the shape and motion of the of premixed flames are strongly influenced by intrinsic instabilities which highlights one of many advances made in the industry through simulations.

One of the outstanding pieces of information required for accurate modelling and simulations is the turbulence field in premixed propagating flames. This includes the need for a numerical approach that is applicable to all regions on the premixed regime diagram, however specifically for this research, explosion and deflagrations mainly fall in the wrinkled flame regime. The work conducted for this thesis is aimed at, not only providing an insight into the complex mechanics, but also proposing solutions and theory surrounding turbulence generation characteristics. With the current advancement with both RANS equations and LES detailed results for turbulent and realistic situations are slowly becoming a viable and accurate source of data. This will continue on from the work conducted by Hall [7] by accurately accounting for velocity fluctuations for both the longitudinal and transverse directions and then correlate this data to corresponding OH LIF images.

3. EXPERIMENTAL SETUP

The research for this thesis engages data from two specially designed combustion chambers. Both chambers have identical dimensions, flow constrictions and turbulence generating obstacles. The first Perspex chamber was successfully used by Kamardin [36] for his undergraduate thesis in 2005 and then with minor modifications used again by Hall [7] in 2006. The vessel's current shape and size is the result of a progression of modifications as the requirements and technology changed [3, 7, 12, 13, 36, 37, 48]. The chamber enables the researcher to easily change the arrangement of the obstacle and baffle plate to generate a wide range of flow conditions. A maximum of three baffle plates and a square obstacle of varying cross sectional dimensions can be placed in the flow. The second chamber has all the aforementioned qualities however it also has several quartz windows to allow the laser sheet for the LIF images to enter and egress without permanent deformation to the chamber.

The combustion chambers described above are a Perspex prism, with inner dimensions $50 \times 50 \times 250$ mm. Within the chamber, are several turbulence generating grids each with 6 slots 5 mm wide that can be placed at three locations up stream of the obstacle. As the flow propagates through the grid, flame jets, and most importantly turbulent flow is produced. Finally the chamber has two possible obstacles centrally located, 96 mm from the ignition point which causes significant disruption to the laminar flow by increasing the blockage and forcing the flow through the narrow channels. The smaller of the two obstacles has a square cross section resulting in a blockage ratio of 25% while the larger, also square cross section has a blockage ratio of 50%. At maximum velocity, approximated from the collected LDV data, and at the egression from a baffle plate the Reynolds number of the flow can be estimated using Equation 3.1 below:

$$\mathrm{Re} = \frac{\rho V D}{\mu}$$

Equation 3.1: Reynolds Number

Assuming standard atmospheric conditions for the density and pressure for air, and a grid spacing of 5 mm, an approximate Reynolds number of 1.31×10^4 is obtained. This outlines the turbulent nature of the flow however highlights the fact the conditions are not extreme and do not contain large scale eddies.

The results used to analyse turbulent premixed combustion for this thesis are a combination of LDV data collect by Hall [7] in 2006 and LIF images coupled with pressure data collected specifically for this research. The LDV data has been reworked with specific attention to the acoustics of the chamber and the shot to shot variation.

The final set up concentrated on the following six areas:-

1. Laser-Induced Fluorescence (LIF)
2. Laser Doppler Velocimeter (LDV)
3. Combustion Chambers
4. Ignition System
5. Operating System
6. Pressure Transducers

3.1 LASER-INDUCED FLUORESCENCE

Using a Laser-Induced Fluorescence diagnostic system, measurements of the transverse hydroxide density profile can be achieved non-destructively. The system required core instrumentation specific to the excitation wavelength of the observed OH, namely a laser excitation sources, focusing and collection optics and an image recorder. The maximum excitation of the OH is at the wavelength corresponding to the largest cross section, which is then used to select the appropriate lasing medium. Using a second harmonic generation crystal, the 566 nm output is transformed from the visual to the ultraviolet spectrum with a wavelength of 283 nm that corresponds to the excitation wavelength of the hydroxyl molecule. The high intensity beam is then focused within the chamber to induce fluorescence of the OH present through out the reaction zone.

3.1.1 Dye Selection

A Quanta-Ray PDL-3 Pulsed Dye Laser manufactured by Spectra-Physics needed to be in this case, pulsed through a dye mixture to produce a 566nm visible yellow burst. Dye selection is crucial as the point of maximum energy must coincide with the excitation wavelength of the free radical to be examined. The figure below shows the output energy curve for Rhodamine and indicates the point at which maximum population inversion occurs. Also indicated in Figure 3.1 is the excitation wavelength for hydroxide, located at the vertical line (566/283 nm). It illustrates that after the beam traverses the doubling crystal the peak output for Rhodamine corresponds to the required excitation for OH. The second harmonic of the Nd:YAG laser is pumped through Rhodamine 590 or Rhodamine 6G, which has a lasing range between 553 nm and 577 nm, that is tuned to 566 nm, then frequency doubled to the required 283 nm. Typical turning efficiencies for alternate dyes as well as the full specification sheet for Rhodamine is reproduced in Appendix C.
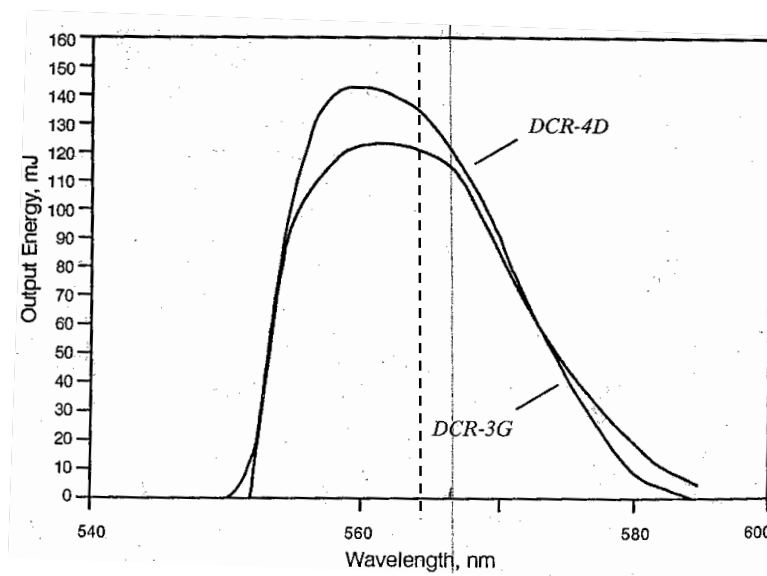
Figure 3.1: Population Inversion for Rhodamine 590 [79]

3.1.2 Optical and Hardware Setup

The complexity surrounding the optical setup for this LIF experiment is in both altering the wavelength of the pulse and in the accurate collection of the data. Firstly the 1064 nm beam produced by the YAG laser has to ultimately be modulated into that of the excitation wavelength of OH. With reference to the schematic diagram in Figure 3.2, the beam egresses from the Nd:YAG laser in the Infrared spectrum (1064 nm) and enters the Second Harmonic Generation (SHG) crystal to have it frequency doubled and wavelength halved. This 532 nm pulse is then used to pump the dye laser (PDL-3) and fired through the Rhodamine 590 solution producing a yellow beam of wavelength 566 nm. Finally the pulse enters another SHG crystal, specifically a KDP crystal to have the wavelength reduced to the required 283 nm which is focused and directed through the measurement section.
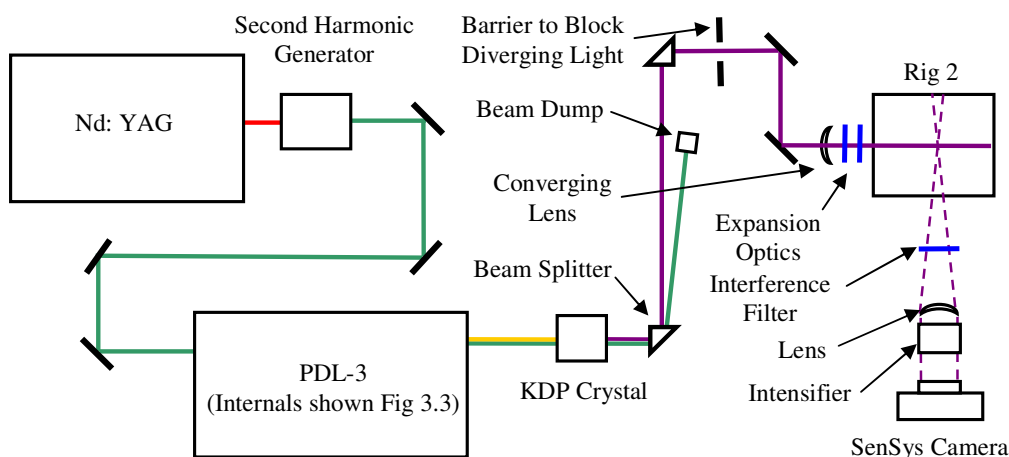
Figure 3.2: Schematic of LIF Optical Components

Collection of the emitted light is achieved using a Photometrics SenSys camera which consists of the camera body containing all the electronic components and the shutter covers. Light produced as the OH species de-excites was passed through an interference filter (10nm width) to insure that only ultra-violet light of wavelength 283 nm in aloud to propagate. Once filtered, the image is focused and disseminated into an intensifier that is opened for a total of 4 ms to completely allow for the beam to traverse the measurement section. A description of how image

intensifiers work is publicised in Appendix D: Intensifier. Finally the intensified image is collected by the camera and digitally transmitted to the Macintosh computer for processing. The final result illustrates the instantaneous relative intensities of the OH concentration across the measurement section.
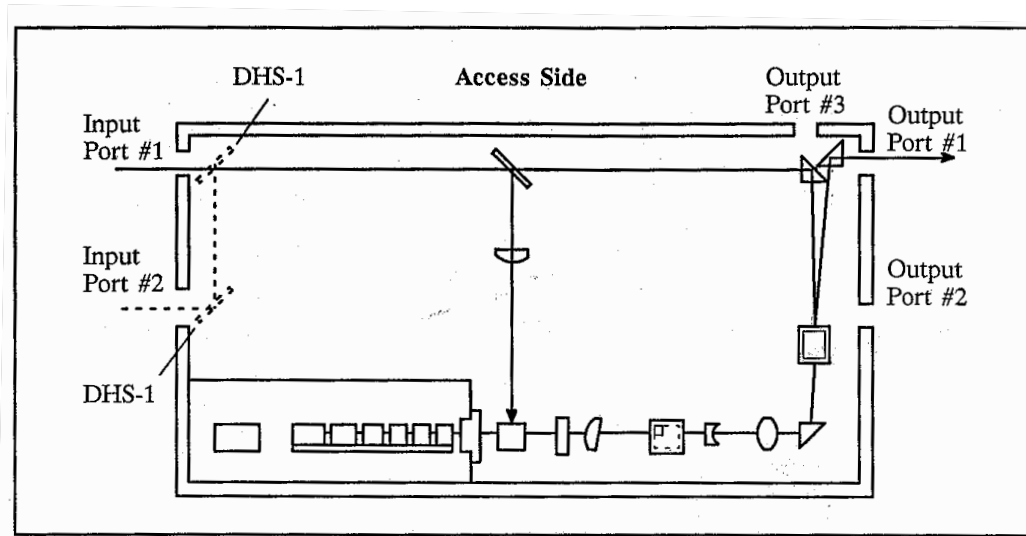
Figure 3.3: Schematic Diagram of PDL-3 [79]

3.1.3 Tuning the Dye Laser

Several parameters associated with both software and hardware significantly improve the signal to noise ratio and thus increase the accuracy and coherentness of the output. As with all lasing equipment subtle shifts in alignment of optical components can produce significant increases in power output. To achieve the maximum obtainable power output for the particular unit the following influential factors were considered.

- Dye concentration
- Beam location through optics
- Oscillator and Amplifier beams correspond
- Only OH is being excited/examined
- No reflections

In the case of dye concentration, both the oscillator and amplifier cells had to be mixed to the required ratio as outlined on the material data sheet (Appendix C). In both cases the dye mixture is combined using methanol as the solvent. For efficiency improvements with the beam trajectory, care was taken to ensure that in all cases where a beam was manipulated the optics themselves were free of imperfections and dust. This also meant that the beam profile passed through the centre of the optics and that the oscillator and amplifier beam profile combine as required. Finally the set up is tested to insure only emissions from excited OH is being collect and not alternate species or unwanted reflections. Figure 3.4 below shows how when the Dye laser is turned off the excitation wavelength of OH nothing is observed. This confirms the validity of the hydroxyl results.
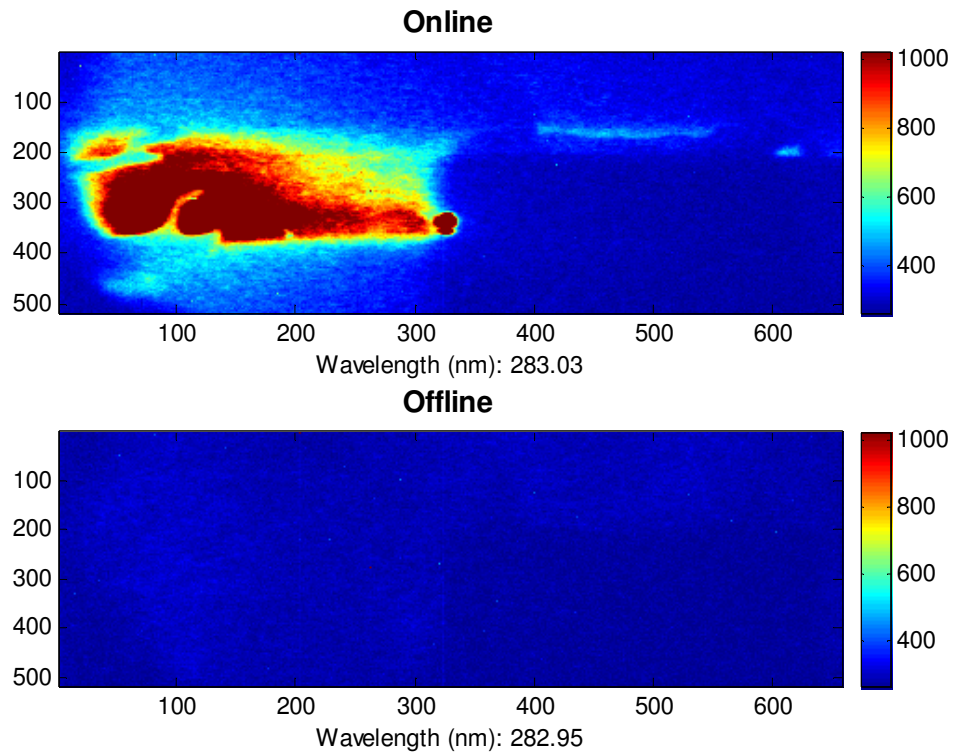
Figure 3.4: On and Off Line Results for OH

3.1.4 Integration of the System Components with Respect to Time

Collection of the LIF data required a complex timing system to fire the various lasers and open both the intensifier and camera within the 20 ms taken for the flame front to propagate the entire length of the chamber. Due to a functional error within the electronics of the LIF YAG, the Lamp is unable to be externally triggered and therefore is set to pulse at 10Hz and hence the need for such a complex integrated system. The main components of the system are the logical gates or "and gates" and delay generators that together integrate the pulsing lamp output of the LIF YAG Laser and the initial user input. The signal diagram below, Figure 3.5, outlines the delays used such that from a given reference pulse of the LIF YAG, the ignition YAG can be fired so that the flames front is crossing the measurement section when the next LIF pulse occurs.
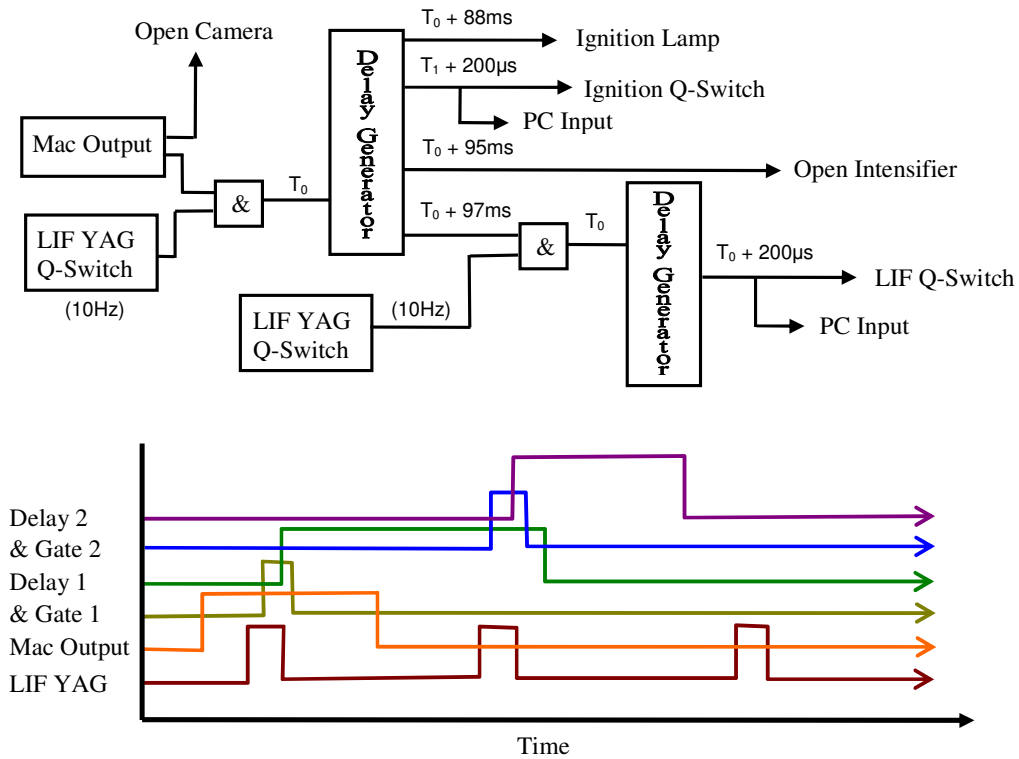
Figure 3.5: Timing Diagram

In addition to setting the timing to coincide with the next LIF pulse, by adjusting the delay for firing the lamp for the ignition YAG, the location of the flame

front is varied from shot to shot. Given the turbulent nature of the flow, accuracy for determining the flame front location is within ±1 ms.

3.2 LASER DOPPLER VELOCIMETER

The Laser Doppler Velocimeter is a system which allows a direct qualitative analysis of particles in a flow as they enter the focal area. Each realisation of the LDV is a measure of the instantaneous transverse and longitudinal components of velocity. Combination of each individual run results in a collection of sample data that can be used to determine fluctuations and treads from a given approximate mean. By assuming the mean follows a smooth polynomial the root mean square for a given time scale will indicate relative turbulence levels present for each configuration. Full experimental set up for the LDV system can be found in Flow Field Measurements in Transient Premixed Flames [7].

3.2.1 Locating the LDV

The LDV system requires the two beams to focus in the combustion chamber at the location of interest perpendicular to the direction of propagation. Both wavelengths, 488 nm (blue light) and 514.5 nm (green light) are then scattered by the seeding particles and received by the photo detector mounted as shown in the schematic diagram below in figure 3.6.
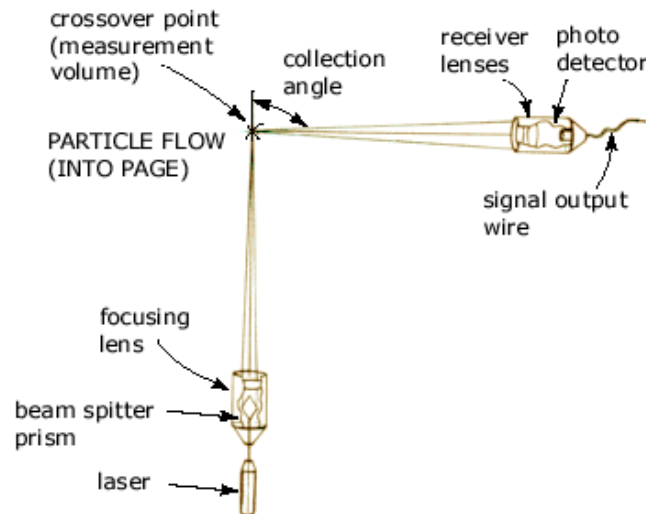
Figure 3.6: Typical LDV Layout [80]

In this case the receiver was placed almost 180° round from the emitter due to reflection problems. As a consequence the system was limited with poor data validity rates and hence the receiver was angled to improve the apparent cross over length (explained 3.2.2).

3.2.2 Focussing the LDV

Accuracy of the results obtain from the experiment relied on the alignment of the emitted and reflected beams. Focusing can occur at three stages throughout the system each as crucial as each other. The first is turning the wavelengths for the two beams which are emitted from the argon ion laser. This alters the intensity of the light produced, allowing minor adjustments to ensure both similar wavelength beams have the identical wattage.

The next stage in focusing the LDV is to ensure that the two pairs of beams are emitted parallel and focus or cross at the same point in the combustion chamber. This is essential as the width of the slot in the receiver is only 100 nm as shown in Figure 3.7. Once the beams are confirmed to be parallel, the exact focus point of the two wavelengths can be ascertained using a lens located at the focus point. This showed that all four beams converged to a single point.

Slot in the receiver
(width = 100μm)

Focus for
both beams

$\lambda = 488nm$

$\lambda = 514.5nm$
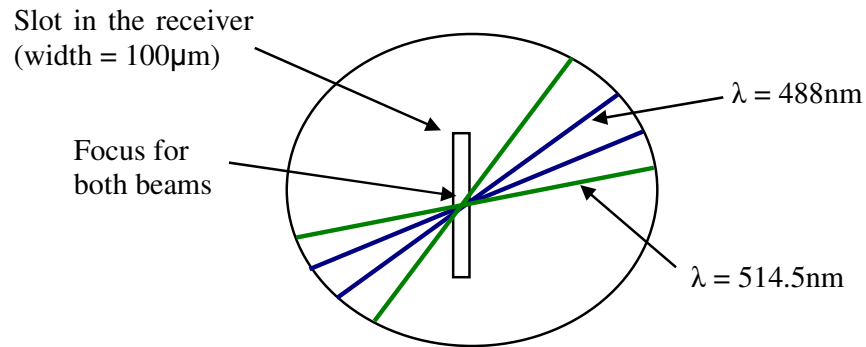
Figure 3.7: Receiver Focus

Finally the receiver is tuned to ensure the observation point included both foci. Figure 3.7 highlights how the intersection of both the green and the blue light lay within the limits of the slot in the optical receiver.

3.2.3 Factors for Measurement Accuracy

One of the main factors influencing measurement accuracy is the reduced volume of the combustion chamber, as this prevents the velocity gradient from broadening. In this case with seeding comprising of Talcum Powder (Hydrous magnesium silicate – $Mg_3[Si_4O_{10}](OH)_2$) of which the diameter of the individual particles was required to be 1 μm for a precision of 1% in velocities with frequencies up to 10 Hz [81]. The high temperature changes through out the experiment created a density gradient which in turn affected the results. As the flame front propagates through the focal point, the seeding density changes with the hot gas products, however as long as the optical and signal analysis settings take this into account accurate results can be obtained [81]. For all the experiments the adjustments remained constant with the velocity limits ranging well over those obtained and frequencies accommodating the full spectrum of data.

3.2.4 Introducing Particulate Material

Seeding must be injected into the flow in order to interact with the interference pattern created by the intersection of the light beams. As the particulate material crosses the fringes, as shown below in Figure 3.8, Doppler bursts were generated changing the intensity of the scatted light. The frequency difference was then proportional to the instantaneous component of velocity for that particle in the plane of the intersection beams.
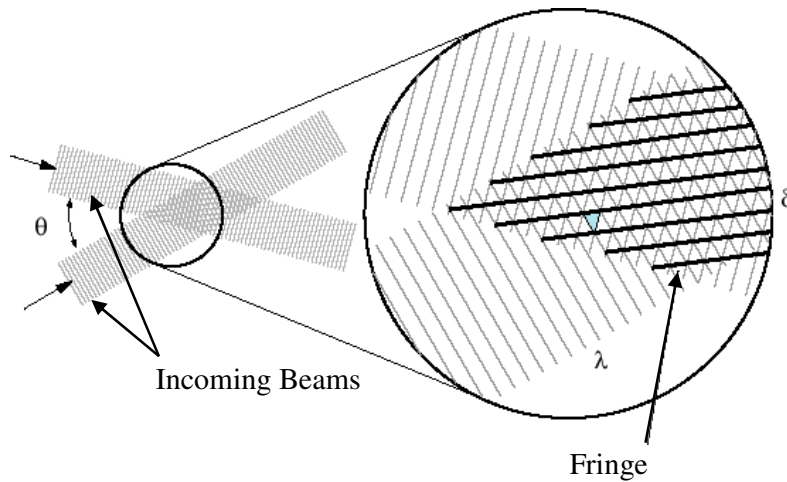
Figure 3.8: Interference Pattern at Focus [80]

As the particles have to be suspended in the flow in order to obtain instantaneous velocity measurements, the particle size is of great importance. For the particles to be in dynamic equilibrium with the flow, the drag on the particle has to significantly surpass the momentum. If the particle are oversized dynamic equilibrium is not achieved, there is a relative velocity that is a function of size, geometry and velocity which needs to be considered [81]. A full breakdown into the mass flow rate and duration for the introduction of particulate material into the system is outlined in Appendix E.

3.3 THE COMBUSTION CHAMBER

The combustion chamber as stated above is a Perspex prism with a volume of 0.625 L corresponding to dimensions of $50 \times 50 \times 250$ mm. Within the chamber the turbulence generating grids and obstruction geometry are arranged in 18 different configurations to produce a cross section of turbulence intensity levels. Configurations are such that they emphasise the importance of grid location on peak pressure and turbulence intensity. The configurations are a progression from distal to proximal grid location in relation to the upstream obstacle, with the set being repeated for both the small and large obstacle.

3.3.1 The Combustion Chamber

An exterior prism constructed from 20 mm thick Perspex was used to contain the thinner 5 mm Perspex combustion chamber. This design encapsulates the inner chamber both helping it to maintain its rigidity and secondly to add additional strength to withstand the shock waves encountered during the explosion.

The inner assembly of Rig 1 comprised of several sections which can be interchanged to achieve the desired layout. Spacers ranged in length from 24 mm to 30 mm so as to allow up to three baffle plates to be inserted without changing the relative height of the up stream face of the obstacle and therefore maintain consistency with any configuration. Where applicable, results are compared to those obtained by Kamardin [36], thus validating the new equipment and procedures.

A dimensioned drawing of the combustion chamber is shown in Figure 3.10, with all grid locations indicated and the square obstructions in position. Grids are 50×50 mm aluminium turbulence generators constructed from 3 mm thick sheet as shown in Figure 3.9. A single grid consists of five 4 mm wide bars each with a 5 mm wide space separating them, rendering a blockage ratio of 40%. In all configurations concerned with grid location the bars are aligned at 90 degrees to the obstacle.

4

50

5

All Dimension in mm
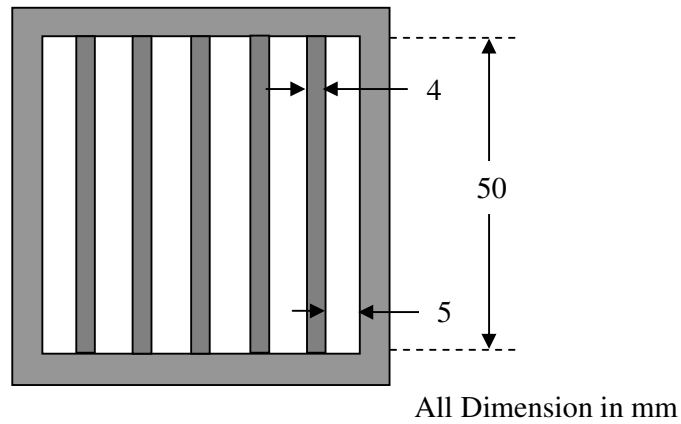
Figure 3.9: Turbulence Grids

Due to the simplicity of the combustion chambers design, changing the order of the spacers and grids to achieve each configuration is relatively simple.

A special chamber (Rig 2) for the collection of the OH-LIF images was constructed so as to allow the high intensity laser sheets to pass through quartz windows without permanent deformation to the chamber walls. The second chamber has dimensions identical that that of the aforementioned however instead of the inner assembly the grids are retained in slots cut directly into the outer wall. Both the obstructions are screwed directly into the side wall. In order to prevent permanent deformation to the inner surface and focus the incoming ignition pulse, a lens was set into the Perspex wall of both Rigs (as shown in Figure 3.10 and 3.11 below).
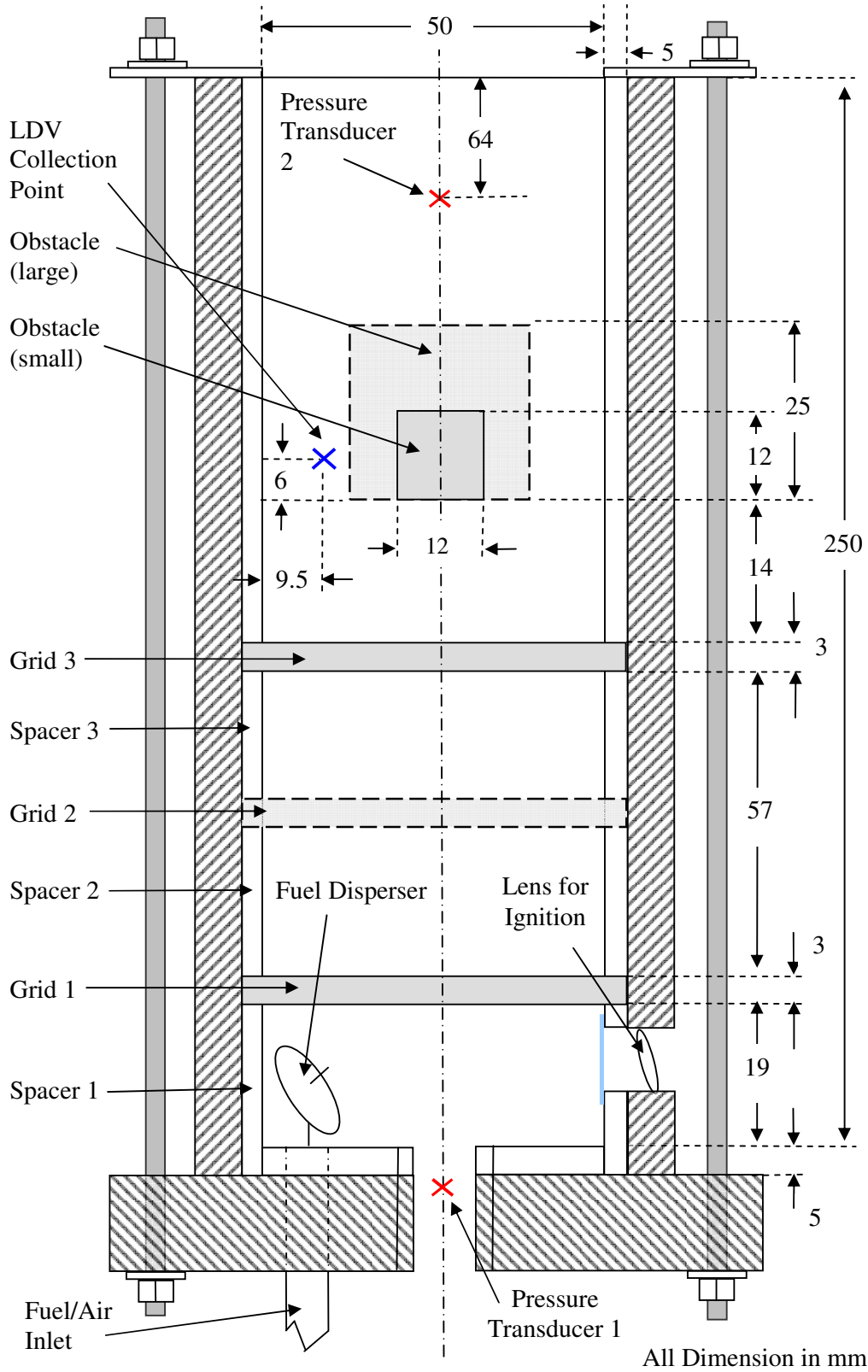
Figure 3.10: Rig One Layout
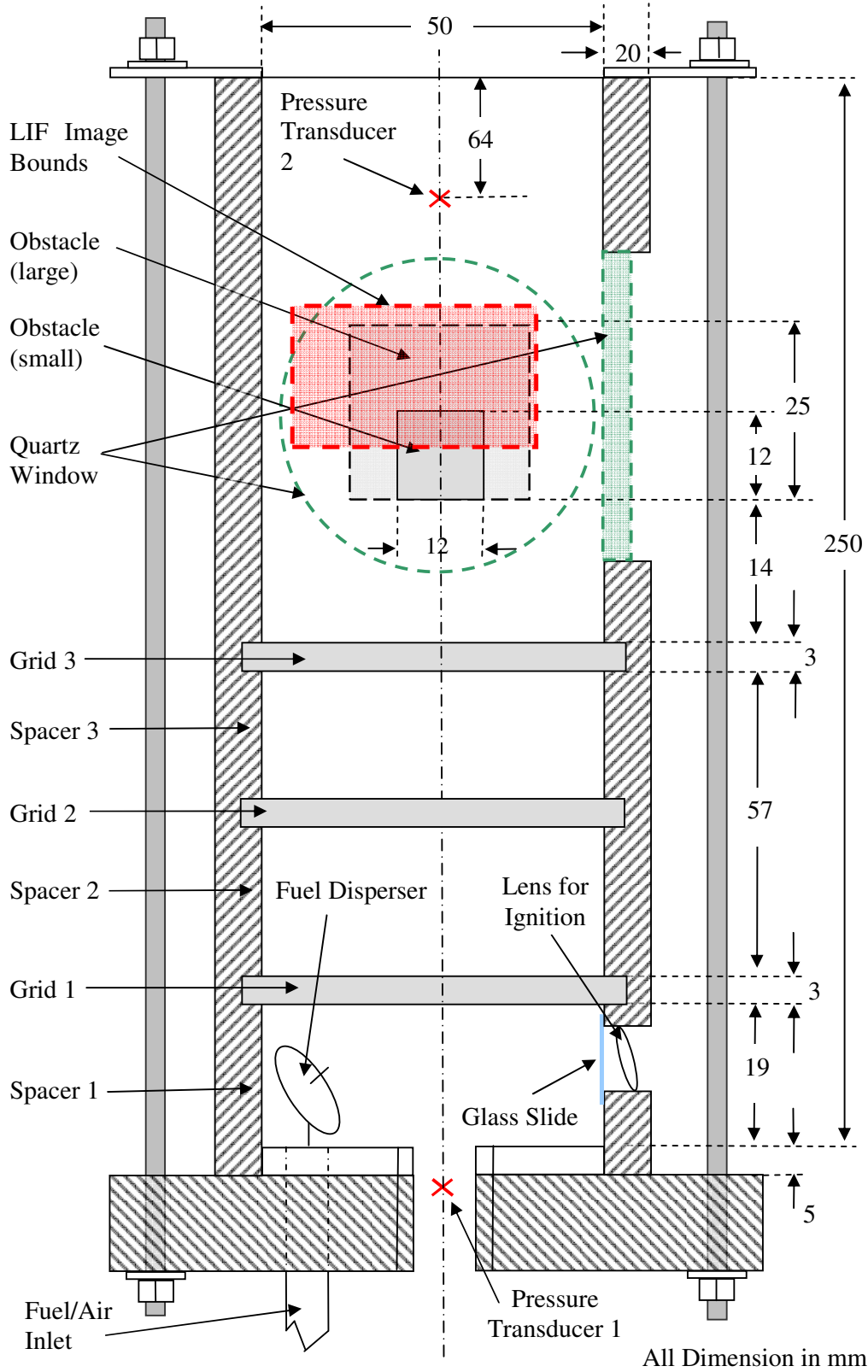
Figure 3.11: Rig Two Layout

Combustion products are expelled through a flap at the top of the chamber that is opened for the duration of the experiment. One of the latest modifications to the both chambers was an aluminium flap to replace the cardboard design used previously. This rigid flap maintains a constant and repeatable venting and fuelling position that was not achievable with previous designs. The flap is pneumatically operated and is integrated into the main experimental control code. To maintain a consistent stoichiometry of air to fuel the flap is kept close during fuelling.

3.3.2 Accommodating the LDV

The Perspex walls of the chamber required modification for the inbound and outbound monochromatic laser beam. As the traversing spectra was being reflected at both the interior and exterior interfaces, multiple convergent point occurred with in the measurement location thus corrupting the data. As shown in Figure 3.12, the reflection produced several parallel beams in the combustion chamber (Rig 1) which interfered and detracted from the primary focal point. At each boundary approximately 4% of the beam was being lost hence reducing the intensity of the beam available from scattering the seeding particles. This problem was solved by removing the material from the outer layer of Perspex on both the in and outbound side of the chamber walls. Removal of the 25 mm Perspex wall from both the in and outbound sides left only the 5 mm inner wall for the beam to traverse, which was not thick enough to interfere with the accuracy of the experiment.
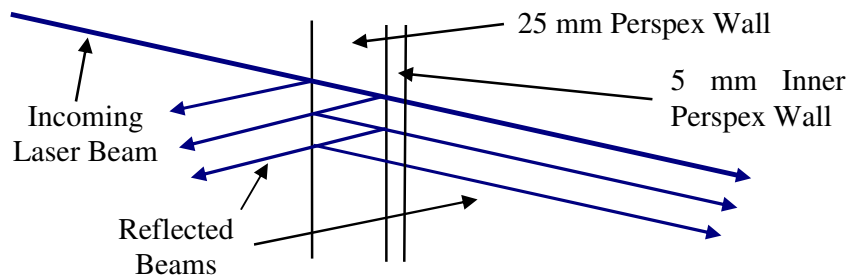
Figure 3.12: Spectra Reflection Though Perspex

3.4 IGNITION SYSTEM

Accurate and consistent ignition of the fuel within the combustion chamber is crucial in obtaining repeatable results and limiting the shot to shot variation. For this experiment, ignition is achieved by using a focused laser beam from a neodymium-doped yttrium aluminum garnet ($Nd:Y_3Al_5O_{12}$) solid-state laser. This focused laser pulse ionizes the atoms in the chamber, consequently creating a spark. Laser ignition allows for a precise and repeatable ignition point with a definable reference time and energy output. In addition by focusing the laser just above the bottom of the combustion chamber, any surface interference is removed, hence achieving a higher level of consistency.

The Nd:YAG laser produces two simultaneous beams of wavelength 1064 nm, in the infrared and 532 nm as visible green light. The visible beam's primary role is to make tracking the path taken by the pulse possible for aligning purposes as the infrared spectrum is not visible to the naked eye.

A schematic diagram of the ignition system is shown below in Figure 3.13:

Figure 3.13: Schematic Diagram of the Ignition System

Adjusting the intensity and frequency of the laser pulse is achieved through an external control console. The user is able to define the lamp energy and most importantly the Q-switch delay. The pulse is controlled by an optical Q-switch inserted in the laser cavity that times the maximum population inversion in the neodymium ions before releasing the pulse. The wave then traverses the cavity, depopulating the excited laser medium at maximum population inversion.

3.5 OPERATING SYSTEM

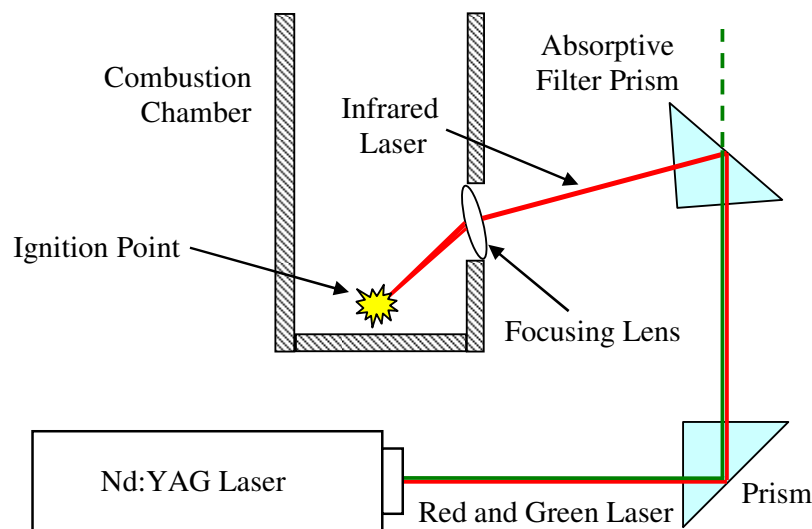The system is controlled by a Macintosh computer operating all the data collection equipment and solenoid valves in a predetermined sequence outlined in a developed macro. The operating system controls the flow of fuel either filling the chamber or re-directing it out the extraction system as well as the flap, ignition system and either LDV or OH-LIF data collection.

3.5.1 Data Collection

Due to technical requirements each data system is independent from the central controlling unit, namely the Macintosh computer. For this reason each computer is linked to the PC responsible for collecting the pressure data, allowing all results to be time resolved and zeroed to a common reference point.

For the LDV system the most significant task performed in terms of data acquisition was the inhibiting of the velocity data collection. All data was stored on a separate PC operated independently from the MAC. This prevented data from being collected until the ignition sequence had begun and therefore the first data point coincided with the point of ignition exactly. Through post-data processing the first point in the data series was then zeroed and a reference time established.

LIF data collection required an elaborate timing regime that was outlined in section (3.1.4). This integrated the MAC outputs into a usable signal timing box that

was able to integrate the pressure PC and the data being saved on the MAC with respect to time.

3.5.2 Directing the Fuel Mixture

The system uses to two two-way valves in series as shown below in the schematic flow diagram (Figure 3.14). Seeding the chamber was only required for the LDV system and thus bypassed when collecting OH-LIF and pressure data.
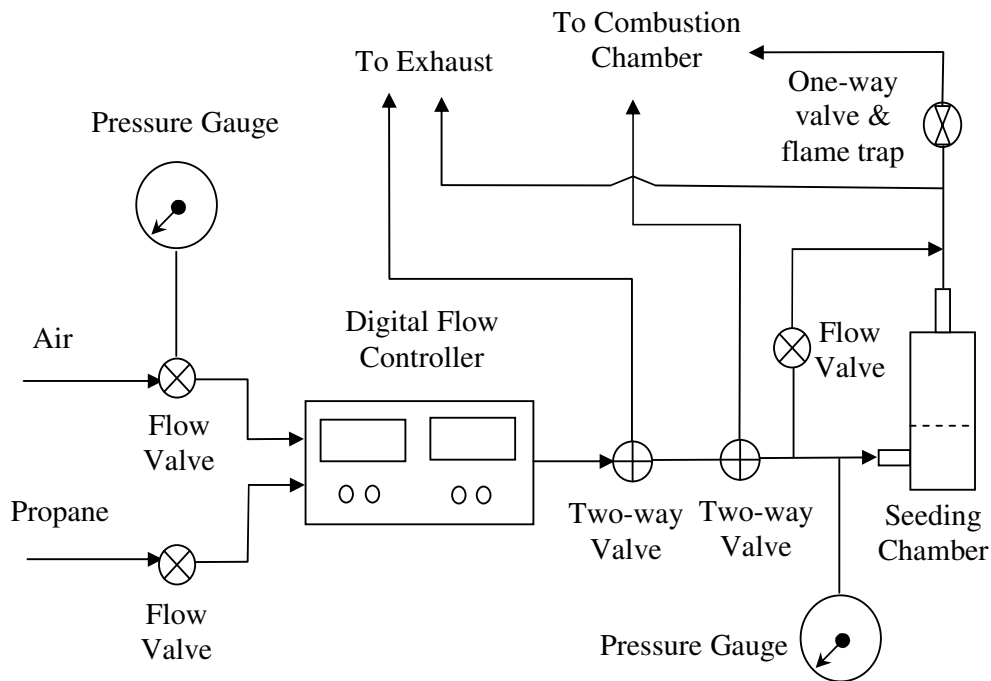
Figure 3.14: Fuel Direction System

3.6 PRESSURE TRANSDUCER

Recent advancements in DC coupled Diaphragm pressure transmitters have meant that pressure data in both chambers was collected with a pair of Keller PR-21S transducers. These transducers are located in the base of the chamber and downstream and perpendicular to the obstacle, both of which are indicated in Figures 3.10 and 3.11.

Before accurate pressure measurements could be obtained both pressure sensors were calibrated against a mercury manometer in standard lab conditions. As seen in Figure 3.15, the scatter of values for the calibration constant is shown to be within 0.5% for both units and thus within the acceptable limits for experimental accuracy. At each of the indicated pressures a reading was taken, from this an average was developed that corresponds to the output volts per measured gauge pressure in kilo Pascals (V/kPa). The Flow diagram for the pressure calibration is reproduced in Appendix (B).
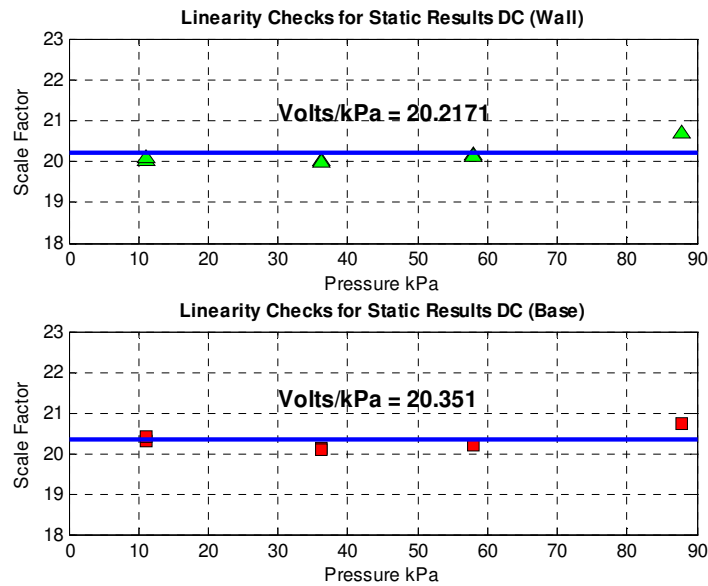
Figure 3.15: Pressure Sensors Calibration (V/kPa)

4. EXPERIMENTAL PROCEDURE

4.1 EXPERIMENTAL PREPARATION

Several key areas had to be attended to before the experiment was both safe to operate and ready to collect data. The areas included:-

1. Occupational Health and Safety Issues
2. OH-LIF
3. LDV
4. Ignition System
5. Operating System
6. Fuel Delivery System

4.1.1 Occupational Health and Safety in the Laboratory

Before any work was conducted in the combustion laboratory, the work station must be free from any unnecessary risks to both the researcher and other lab staff. A safe work practice must be maintained at all times, including:-

1. Removal of any slip, trip and fall hazards. These may include electrical and optical cables, as well as fuel and air lies which lie across thoroughfares.
2. Replacement of all tools not required.
3. Engage exhaust fan two.

4.1.2 OH-LIF Operation

The LIF system has two main components namely the Nd:YAG laser used to produce the initial pulse and the Dye Laser used to manipulate the beam to the

required frequency and wavelength. As with all optical equipment the system must be run for approximately 30 minutes to ensure all lenses and mirrors have reached equilibrium so a stable power output in obtain. The procedure is as follows:-

1. Turn on dye pump.
2. Ensure the cooling water is flowing through the system
3. Turning on the YAG laser requires:
    a. The safety key to be in the on position
    b. Turn the Laser on at the power supply
    c. Turn the Oscillator on at the control consol
    d. Turn the Amplifier on at the power supply and control consol
    e. Confirm simmer lights on the Oscillator and Amplifier are laminated
    f. Oscillator; Regulate "Laser lamp energy" to maximum (90 Joules/Pulse)
    g. Amplifier; Regulate "Lamp energy adjust" to 80% ($\approx$ 72 Joules/Pulse)
4. Align the KDP doubling crystal to obtain maximum output (to be continually confirmed and adjusted through out experiment).
5. Ensure all beam reflections are collected or terminated and all lenses and mirrors are free from dirt and imperfections.
6. Turn SenSys Camera on.
7. Turn intensifier on and adjust voltage, then power down when not in use.
8. Acquire several normalisation and back ground images before experimentation can commence.

4.1.3 LDV Operation

The LDV requires a few minutes to warm up, and will remain on indefinitely as long as the cold cooling water is continually supplied. The procedure is:-

1. Turn on the water pump.
2. Ensure the cooling tower is in operation and all the valves are allowing water flow through the system.
3. Turning on the Argon Laser requires:
    a. The main power switch to be turned on
    b. The console key to be turned to Plasma On and the green light to illuminate
    c. Turn the current to 25 amps
    d. Confirm no red light is on in the interlock status section
4. Check the power output of the laser by switching the meter to read watts. Typically this should be of the order of 4.5 W.
5. Turn the inhibiter on, located at the rear of the main control box.

4.1.4 Ignition System Setup

Assuming the cooling system is already in operation, the procedure is:-

1. Turn the laser on at the wall, the main power and cooling unit and the control box.
2. Confirm the laser is firing and is aimed in the centre of the chamber approximately 2 mm from the lower surface. Use the Q-Switch delay to insure a spark is produced every pulse.
3. Switch the laser to external input on the control box.

4.1.5 Fuel Delivery System

The start-up procedure is:-

1. Turn on the fuel at the gas bottle and the compressed air with the valve on the wall.
2. Turn on the mass flow meter and confirm the pipes and valves are not leaking. Note: Propane is a colourless gas however it has a distinctive odour.

4.1.6 Computer Control System and Checks

The system works from three independent computers; a MAC and two PC which are not networked and must be operated simultaneously to collect the data for each run. The MAC was responsible for running the experiment from the programmed macro, while the first PC was connected to the LDV system and the second connected to the pressure sensor. Both the PC's where responsible for correlating all the results. For LIF the LDV PC is not required however the delay generators have to be powered up and initiated in order to receive and distribute the MAC commands. The startup procedure was:-

1. Turn on the MAC and PC's. Logon the LDV PC as a TSI user and the Pressure PC as Combustion, password "Combustion".
2. On the LDV PC desktop open the "Flow Sizer" program, this will bring up the LDV software with the configuration setting from the last experiment. Not require for LIF as all LIF data is stored on the MAC.
3. On the Pressure PC desktop open the "LabView" software, to facilitate pressure recording. Use predetermined operation sequence.
4. Open the macro running program on the MAC titled "expl1". At this point all the apparatus should be tested by typing the following commands:-
    a. Upload the macro into the work space
       >> gm expl1: Uploads the macro "expl1"
       >> lm: Displays the current macro
    b. Test the flap actuator
       >> out 8: opens the venting flap
       >> out 0: restores the default conditions
    c. Test the ignition and LIF pulse
       >> out 4: fires both lasers as per sequence determined in the delay generators
    d. Test the seeding (not required for LIF)
       >> out 1: directs the fuel/air through the seeding vessel
    e. Finally test the operation
       >> rm: runs the macro once

4.2 EXPERIMENTAL SEQUENCE

The exact experimental sequence is governed by the macro code that operates the MAC computer and consequently the experiment. This code is outlined in Appendix (A.1) for LIF and Appendix (A.2) for LDV, along with syntax explanations. Once the experiment has started, both PC's must initiate data collection as follows:-
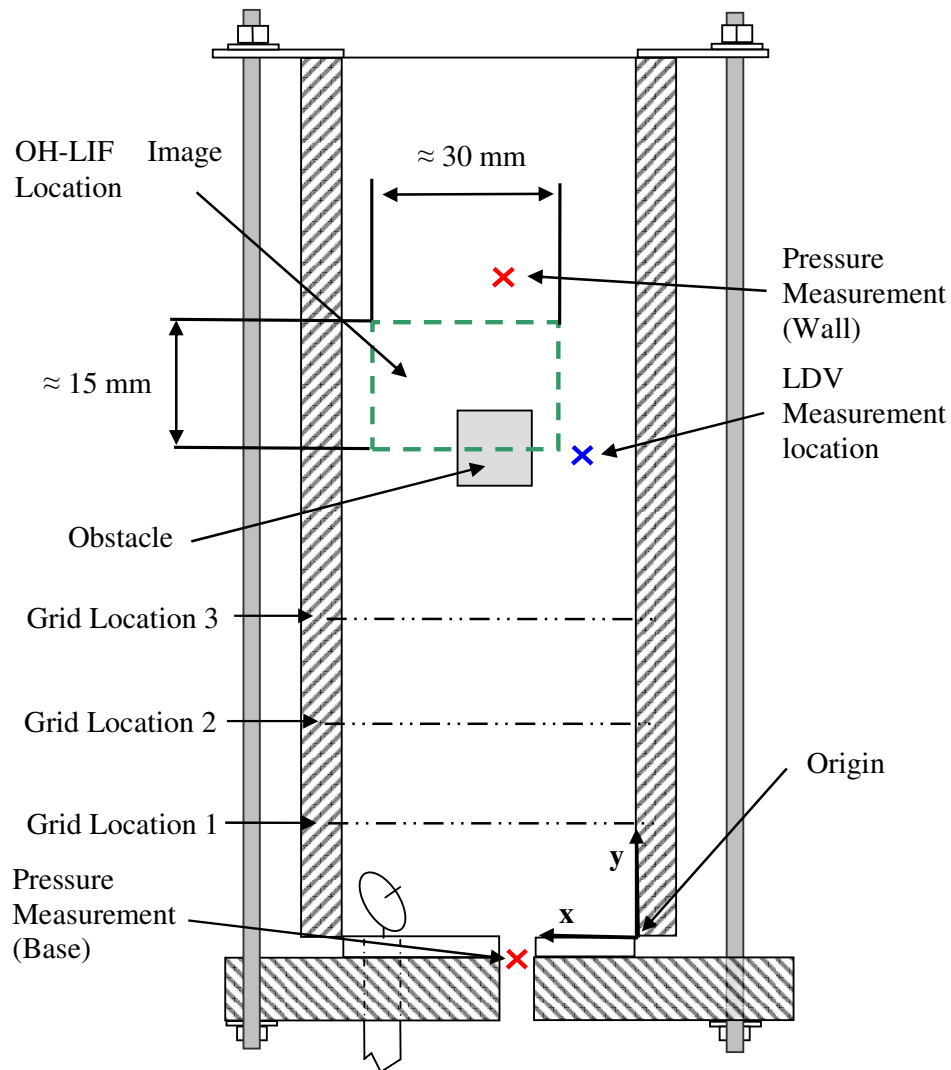
1. Establish an appropriate file directory on all computers to save recorded data.
2. Set the LDV PC to Capture Data (F9) (LDV only).
3. On the MAC set the camera to a gain of 3 and adjust the colour bar for displayed images (LIF only).
4. Set the Pressure PC to record after the second "beep" (records 1.2 seconds worth of data and saves automatically in the predetermined directory.
5. End Run (F5) on the LDV PC to consolidate data (LDV only).
6. Saving data:
    a. LDV PC: Quick Save (F10) saves data and opens a new file sequentially named (LDV only)
    b. MAC: Must transfer all data across the network to the larger MAC to ensure enough temporary memory is maintained (LIF only)
7. Repeat steps 2 to 6 for each experimental run.

4.3 EXPERIMENTAL CONFIGURATIONS

The focus location considered for the LDV, the LIF image boundary and the pressure measurement locations are shown in the diagram of the combustion chamber below in Figure 4.1 and in Table 4.1.

Measurement	X ordinate (mm)	Y ordinate (mm)
Pressure (Base)	25	-55
Pressure (Wall)	25	180
OH-LIF Image	$\approx 15 - 45$	$\approx 108\text{-}130$
LDV	9	104

Table 4.1: LDV, LIF and Pressure Measurement Locations

OH-LIF   Image
Location

≈ 30 mm

Pressure
Measurement
(Wall)

≈ 15 mm

LDV
Measurement
location

Obstacle

Grid Location 3

Grid Location 2

Origin

Grid Location 1

y

Pressure
Measurement
(Base)

x

Note: all dimensions as in Figure 3.11

Figure 4.1: Measurement Locations

In all instances the run set up was based on a variety of grid configurations in order to generate a range of turbulence levels within the chamber. Experimental parameters such as stoichiometry, seeding rate, settling time and the duration aloud for fuel to enter the chamber remained constant unless being the variable under specific investigation. The 18 individual grid and obstacles configurations have been broken up into families that consist of a logical progression of the grid or grids downstream towards the obstruction. In two cases, configurations 1 and 18, the effect of no obstruction is examined.

Configuration 1   Configuration 18

Configuration 2   Configuration 3   Configuration 4   Configuration 5

Configuration 6   Configuration 7   Configuration 8   Configuration 9

Configuration 10   Configuration 11   Configuration 12   Configuration 13

Configuration 14   Configuration 15   Configuration 16   Configuration 17
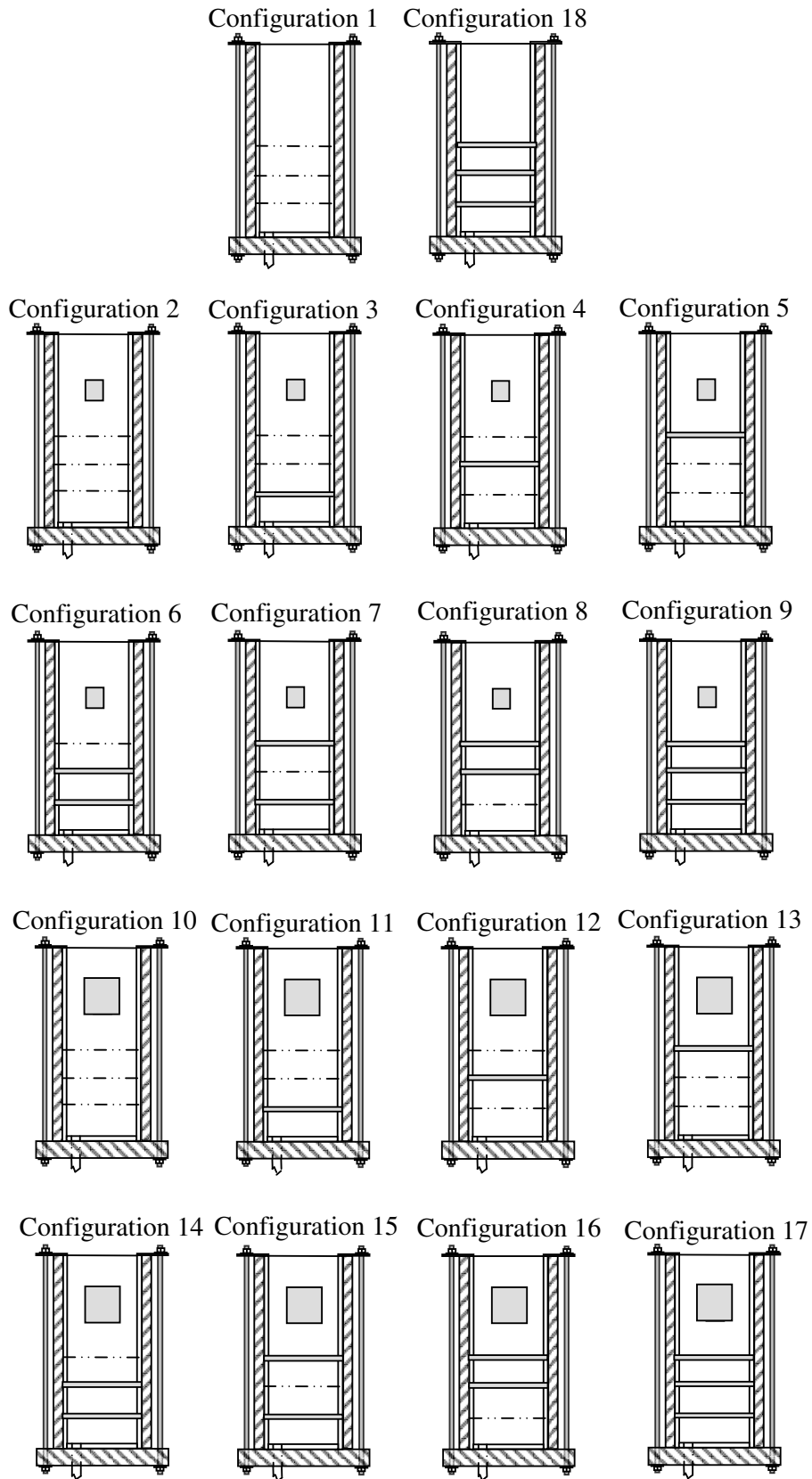
Figure 4.2: Experimental Configurations

Configuration Layout				
Configuration	**Grid 1**	**Grid 2**	**Grid 3**	**Obstacle Size**
1	-	-	-	-
Family 1 2	-	-	-	S
3	Y	-	-	S
4	-	Y	-	S
5	-	-	Y	S
Family 3 6	Y	Y	-	S
7	Y	-	Y	S
8	-	Y	Y	S
9	Y	Y	Y	S
Family 2 10	-	-	-	B
11	Y	-	-	B
12	-	Y	-	B
13	-	-	Y	B
Family 4 14	Y	Y	-	B
15	Y	-	Y	B
16	-	Y	Y	B
17	Y	Y	Y	B
18	Y	Y	Y	-

Table 4.2: Experimental Configurations (Grey Indicates LDV Data is Available)

The size of the obstruction was also changed to alter the blockage ratio from the small cross section featured through out to a cross section with twice the area. This larger obstruction was located as indicated above in Section (3.3). However it was found that the dimensions meant the passage between the wall and side of the obstacle blocked the focal point at location 1 from the view of the LDV receiver. In addition to this the light beams where being reflected off the wall and impediment numerous times as it traversed the narrow passage. This created interference patterns that corrupted the LDV data. In addition to this, LIF measurements were unobtainable for the large obstacle as the majority of the quartz window was obstructed. Therefore analysis of the large obstruction was only preformed using pressure results.

5. DATA PROCESSING

This research consists of several key areas in data processing related to correlation and presentation. For each aspect of the aforementioned data collection process a sound processing technique had to be developed that was able to integrate information from several sources and in the case of LDV and LIF measurements, data from completely independent experiments conducted over the course of year. The most instrumental factor in terms of data processing is the ability to establish a reference time and therefore a common T_o which marks the initiations of a flame kernel across all results. The processes considered include:-

1. Establishing Time Zero
2. LIF Processing
3. LDV Processing

5.1 ESTABLISHING TIME ZERO

The Pressure PC is responsible for collecting not only the multiple pressure time traces but also the Q-Switch signals for both the Ignition and LIF YAG lasers. These signals are voltage steps sent by delay generator after being queued by the Macintosh. For both signals, the step is maintained for long enough to ensure the 4 kHz sample rate collects a suitable and accurate amount of data points. In all cases the initial step is taken to be the reference point and the rest of the signal is discarded. Figure 5.1 below shows the raw data collected by the pressure PC during the LIF experiments. Establishing a reference time for the LDV data worked from a similar principle, except that the inhibit signal acted as the marker from which to correct T_0. This then meant that the time stamp for each validated data point was then with reference to the ignition Q-Switch and therefore in correlation with the pressure traces and the approximate initiation of the kernel. In addition to this the LIF images are referenced to the second Q-Switch signal and again relative to the ignition Q-Switch thus establishing a solid T_0 for all data collected.
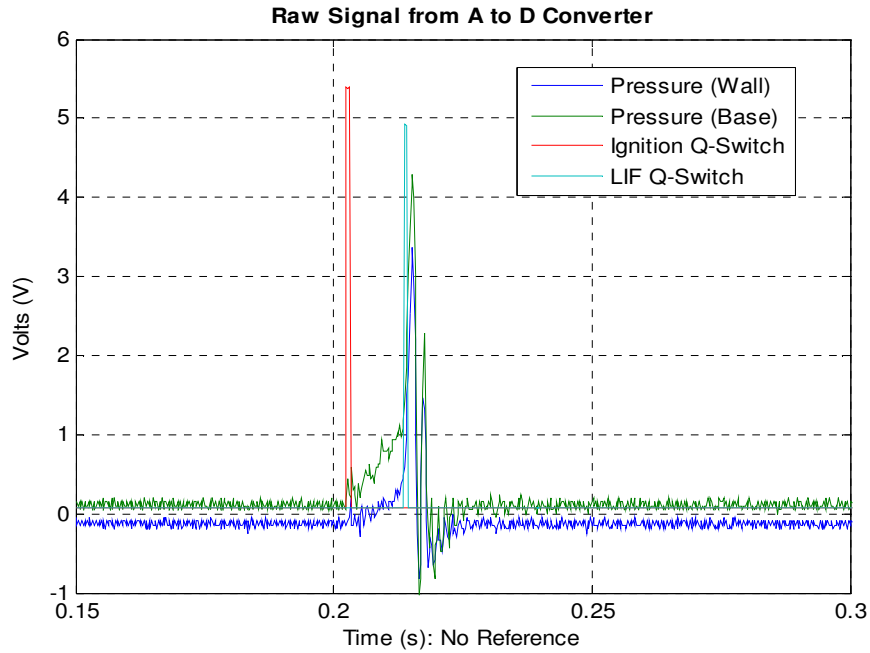
Figure 5.1: Raw Pressure and Q-Switch Signals

5.1.1 Errors and Inconsistencies Associated with the Pressure Data

All pressure results were obtained using new DC coupled pressure transducers and as a result the experimental fluctuation is negligible. For any given configuration the peak pressure variation is within 10% of the mean. This highlights the repeatability of the experimental procedure and the accuracy of all the data sets relative to any underlying shot to shot variation. The figure below shows an example of the maximum pressure values around the mean for a configuration in the mid turbulence range.
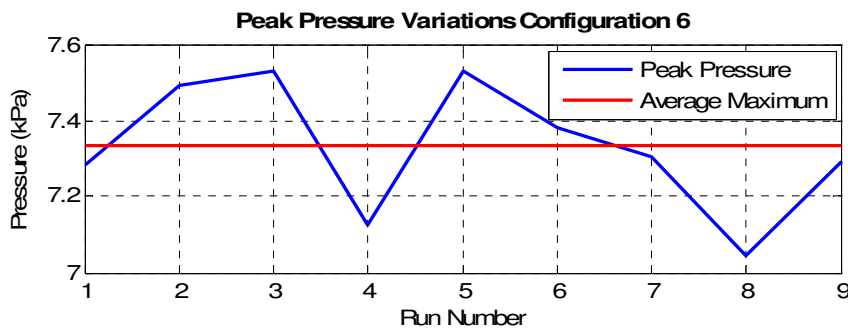

Figure 5.2: Peak Pressure Variation

In the time domain, errors still arise with the development of the kernel as well as errors inherent in the Q-switch from the YAG laser. For both the pressure and the velocity time traces, the approximation that the peak values align is assumed. This establishes a reference point independent of the kernel development time and any inconsistencies surrounding the energy of the ignition spark. Both these processing techniques are described in Section 5, however it is important to re-enforce how the data has been manipulated in each case.

5.2 LIF PROCESSING

To be able to use the LIF images for a qualitative analysis, all images had to be cropped, zeroed and normalised for the variation in beam profile and intensity. All processing was performed post experiment on MatLab after being converted from the Macintosh file format to a text file that can be opened on a window operating system. For each image the following steps were taken to process and present the data for qualitative analysis:-

1. Initially a background image is subtracted to remove noise and any direct reflections.

2. The image then had to be corrected for the beam profile variation. This is due to the LIF pulse not being perfectly uniform nor parallel to the plan of the camera and thus the intensity not homogeneous across the section. As a result the relative radical concentration does not reflect true values. A constant flame was imaged with a mean profile being produced in order to correct for this. By dividing the image by the resulting correction profile (shown Figure 5.3) the OH concentrations are restored and can be used for quantitative analysis.
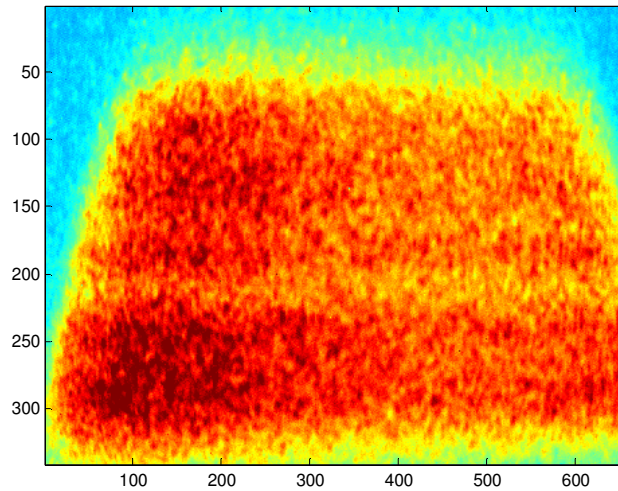
Figure 5.3: Normalisation Image

The figure above, Figure 5.3, shows how a constant source of OH can appear as a result of an uncorrected beam profile. In the vertical or longitudinal direction the band indicates that the cross section of the beam profile is not uniform and in fact changes intensity from top to bottom. Alternatively in the horizontal or transverse directions it can be seen that the plan of the beam is not perfectly parallel to that of the camera. The regions of higher intensity to the left hand side of the image indicate a better focus to that of the right hand side and thus more light has been collected. Both factors are corrected for.

3. After normalisation the raw images are smoothed in 2 dimensions to remove the graininess and any reflections or sharp changes in intensity. In both directions a 15 by 15 pixel box is used to produce an average which is used for the centre cell. The results for this process are shown in Figure 5.4 (a) and (b).
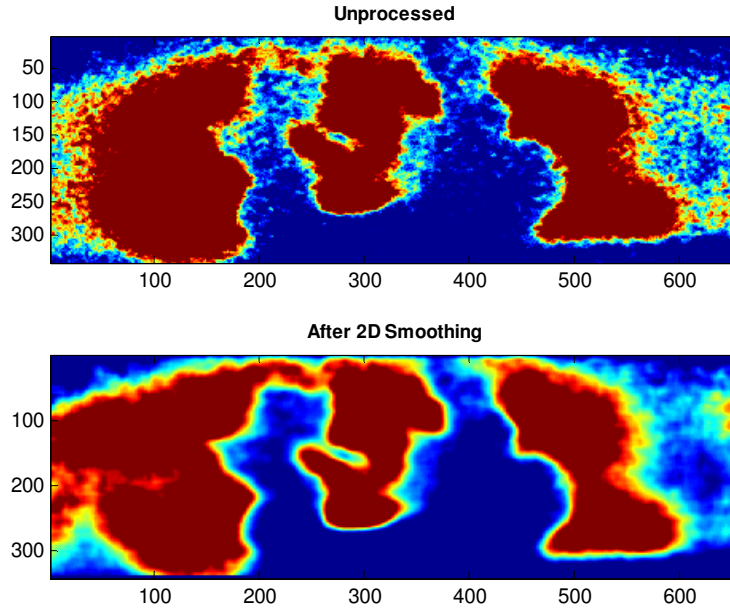
Figure 5.4: Smoothed and Raw Images

4. Finally the image is cropped to both remove redundant data that lies outside the beam width and to significantly reduce the overall file size.

5. In addition to individual image processing, all images were analysed as a collection so images with insufficient beam energy could be eliminated as well as images with no visible flame front. Each configuration had approximately 10% of the data removed.

5.3 LDV PROCESSING

Due to the large variation and limited number of valid velocity counts per run, results and conclusions are derived from an ensemble average. This technique creates an average velocity by analysing the entire data sample for each configuration to give a mean velocity for a given point in time. Since the velocity data is collected at random time intervals each point was rounded and filed with a time interval or bin size of a quarter of a millisecond. Before this each individual realisation has the peak velocity shifted to the mean peak location in order to remove a component of the shot to shot variation. This time shift eliminates the dependence on the kernel development and allows for the data to be analysed assuming equal intensity ignition pulse. Mean

velocity can then be plotted in conjunction with the raw data to give an indication of the underlying shot to shot variation associated with the turbulence intensity. From this point two alternate processing techniques are used to determine the RMS and thus turbulence intensity of the flow.

5.3.1 RMS from a Global Mean

Using the mean profile described above, a least squares fit polynomial is derived. This polynomial profile further eliminates errors imbedded in the flow data arising from the ensemble mean. By smoothing the mean profile, less natural variance is included in the calculation by removing slight deviations due to outlying or miss-fired data that cause shifts in the mean. Due to the small number of data points per bin, a single run has the potential to disrupt the mean profile and thus induce an error. The figure below (Figure 5.5) shows a typical case with the three stages of the data processing.
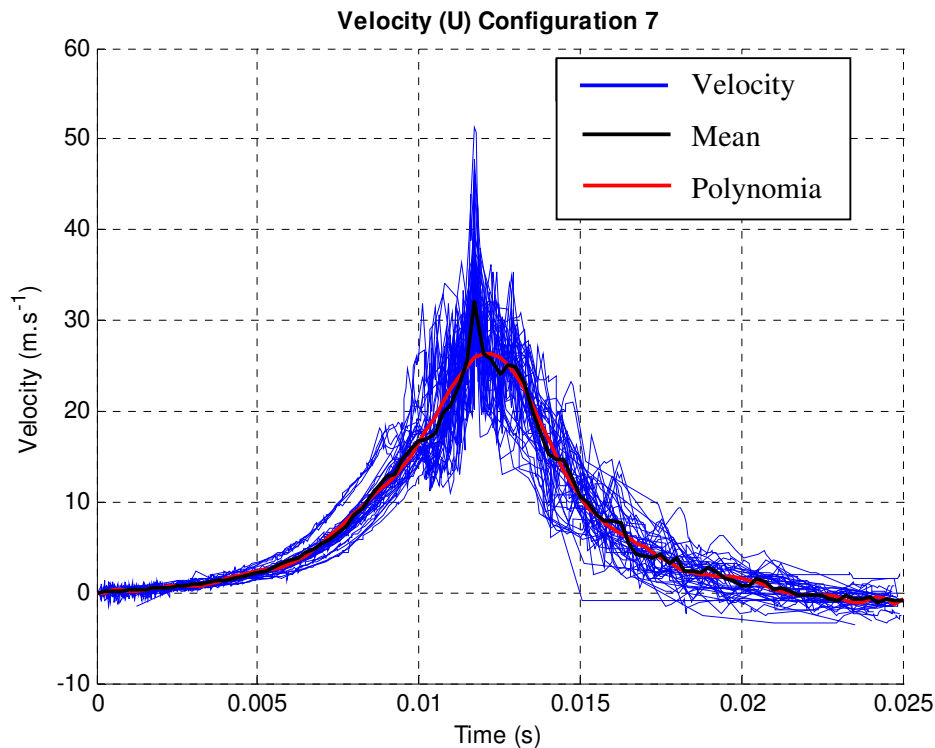

Figure 5.5: Velocity Time Traces with Mean

The order of the polynomial was varied to examine the effects of a high order and typically unstable curve. Since the flow does not follow a polynomial, stability is the most important factor in order to achieve an accurate flow field approximation from which to calculate the root mean square (all data relating to the order analysis that was conducted is reproduced in Appendix F). It was found that a polynomial of order 20 was able to handle the complex curves associated with the initial acceleration to peak velocity as well as the acoustic effects post peak. These acoustic effects are more pronounced in the pressure time traces however they add addition deviation to a mean that is not due to turbulence. As can be seen in the above figure, the polynomial approximation is a good smoothing technique.

Once the average velocity profile was obtained the root mean square was calculated to give a turbulence indication for the channel and thus as the flow progresses into the wake behind the obstruction. Using the same concept as described above, the RMS of the velocity data is calculated with a bin size of 0.25 ms from the equation shown below:

$$RMS = \sqrt{\left(\frac{1}{n}\sum\left(x_n - \bar{x}\right)^2\right)}$$
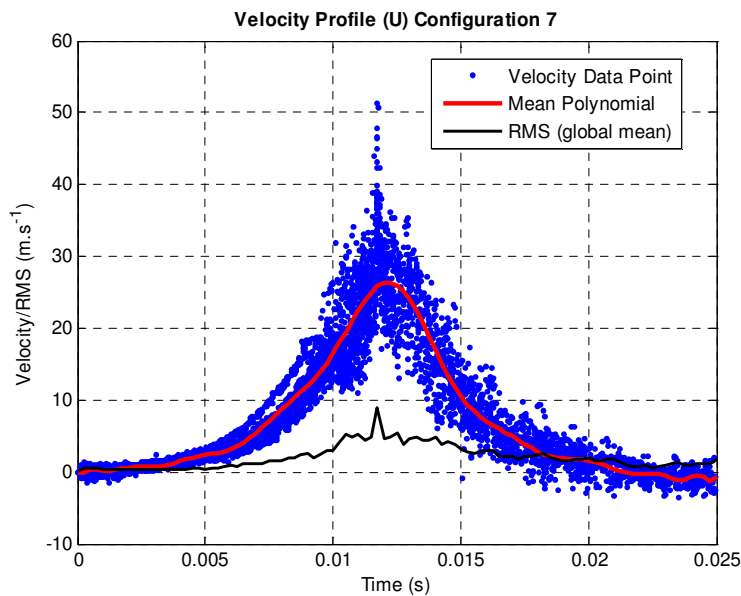
Equation 5.1: RMS

Figure 5.6: Velocity Data Points with Global Mean

This gives a variance value per time step that can be plotted as a function of time, therefore giving a turbulence intensity approximation as the flame propagates down the chamber. The final result is reproduced in Figure 5.6 on the previous page.

5.3.2 RMS from an Individual Polynomial

In contrast to the aforementioned procedure for calculating the root mean square, an alternate methodology was proposed and examined in an attempt to further reduce to the errors inherent in an ensemble average. This method differs from the previous in that a polynomial is fitted to <u>each</u> individual velocity time trace thus eliminating any timing errors associated with kernel development. Figure 5.7 below highlights the errors attached with the previous method, in that a given ensemble can not accurately describe a collection of completely independent realisations.
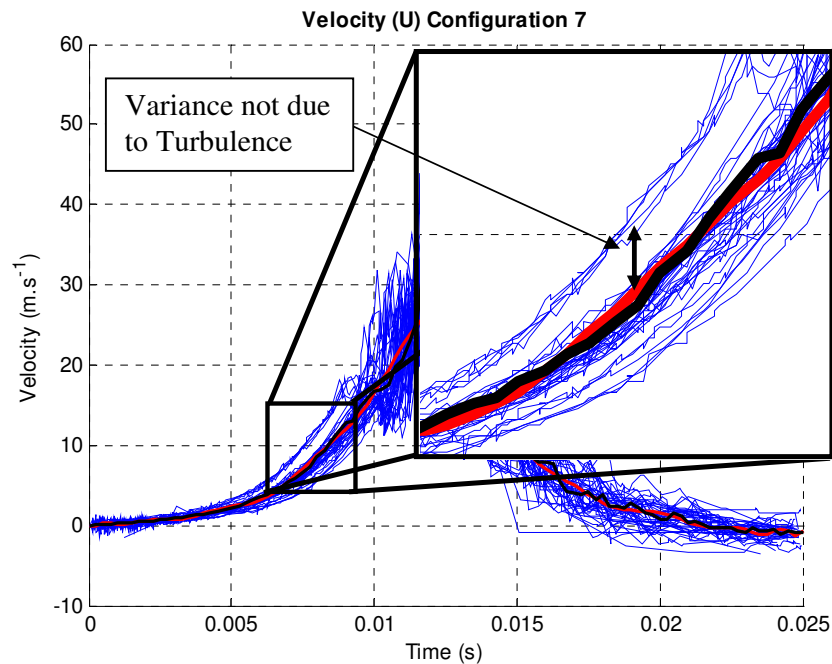

Figure 5.7: RMS Calculation Errors

By fitting a polynomial of the same order to each individual realisation a more accurate laminar profile on which to base RMS calculations is developed. This methodology incorporates variation in ignition energy and kernel development time

and thus produces a mean more suited to the individual run. Such a technique is similar to applying a high frequency filter to the data that is able to eliminate the underlying profile of the velocity and leaving only variations due to the turbulent environment. Closer examination of Figure 5.8 shows how the polynomial now follows the individual form of any given realisation.
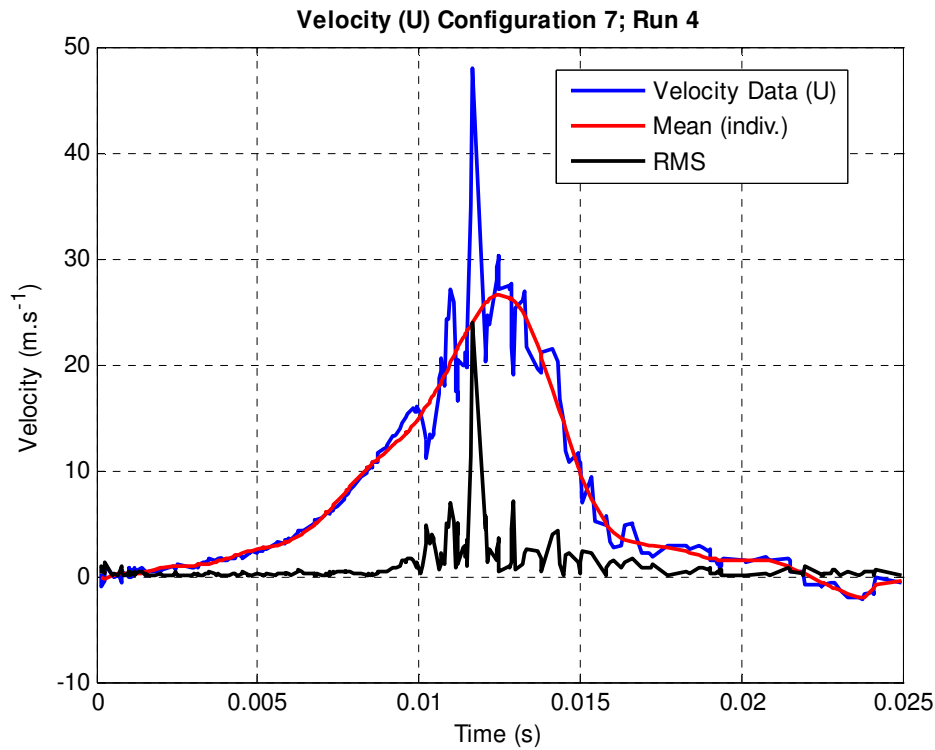

Figure 5.8: Individually Filtered Velocity RMS

Finally RMS data from each run is collected to give a mean using the identical binning technique described above. An ensemble root mean square result reasonably describes the subtle flow responses to a turbulent environment as regions of repeated high RMS can be assumed to be consistent across the data series. Individual fluctuations however, such as can be seen in the above figure, are lost when accumulated but this mean describes the approximate location, in terms of peak velocity, of heightened turbulence intensity for any given realisation.

5.3.3 Errors and Inconsistencies

In several cases the velocity profiles show a remarkably consistent correlation to the ensemble average. However in some cases, namely configurations 6 and 8, the scatter and deviation is greater than others, the theoretical reason for which is unclear and is therefore linked to experimental conditions. In all four cases that have accompanying LDV data, the set is a culmination of 50 individual runs taken sequentially and plotted by aligning the point of maximum velocity.

Further examination into the experimental procedure revealed a number of factors that could also be the cause of the variation, namely timing errors as outlined previously and a discrepancy with the ignition. Section 5.1 outlines the nature of the delay associated with establishing T_o from the Q switch in relation to the LDV inhibit signal. By referencing all the results to the ignition Q switch, the signal delay inherent in the processing speed was reduced.

Excess scatter and limited data validation corrupting some of the data was discussed, analysed and proved as the primary reason for inaccurate data by Hall [7]. As the data used is identical, this will not be considered further, however the method behind processing the data has been improved and will be analysed in this section.
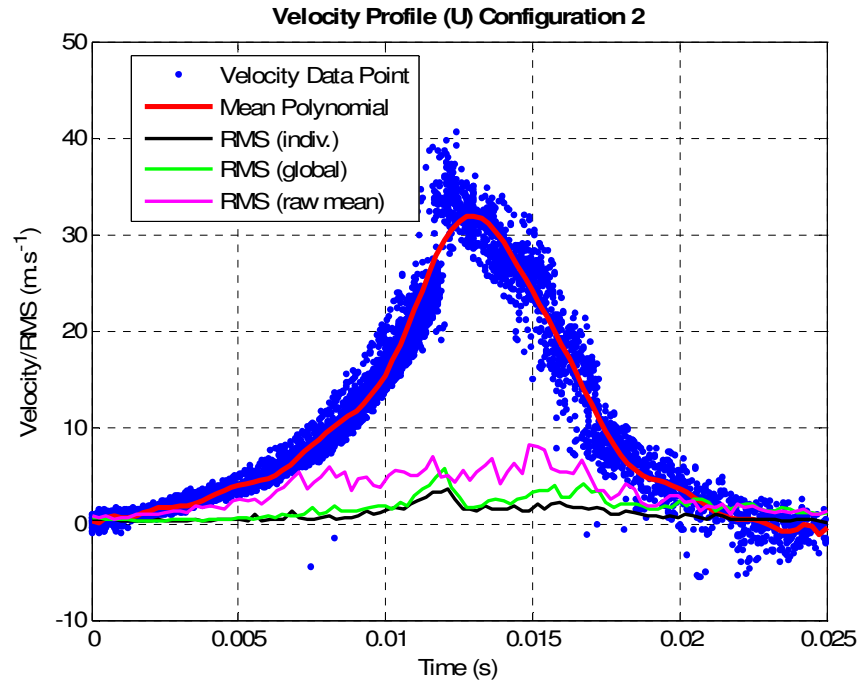
Figure 5.9: Comparison between the Various RMS Calculation Techniques

The most significant factor influencing the credibility of the RMS calculations is the method used to eliminate the intrinsic shot to shot variation with out corrupting the very stochastic nature of the turbulence itself. As shown with the pressure results experimental consistency is obtainable within a total range of approximately 10% of the ensemble mean. As outlined in Section 5.3.1 and 5.3.2 above, several methods to calculate the RMS of the flow have been trailed in an attempt to minimise the errors associated with such a calculation. Figure 5.9 above shows all three considered techniques with the magenta representing the RMS results previously obtained by Hall [7]. Examination of the black and green lines shows how using a global polynomial (red) includes a significant amount of variation due to kernel development and not necessarily turbulence. This is evident at peak velocity; where the global polynomial approximation does not realistically predict nor take into consider the random and dynamic nature of the flow. By using an individually fitted polynomial, a laminar profile is approximated to each realisation in order to eliminate such inconsistencies. For this reason RMS analysis will be using the individual polynomial technique outlined in this section an accurate and consistent method is analysed with only limited fundamental errors associated with the poor seeding rate discussed above.

6. RESULTS

The results presented for this thesis are a combination of data collected for an undergraduate thesis [7] in 2006 and specifically for this work in 2007. All results have been processed, as outlined in section 5 above allowing an insight into some of the flame front properties associated with a transient, propagating reaction zone. The results are shown for individual configurations as well as the family groups outlined in section 4.

6.1 EFFECTS OF STOICHIOMETRY

Effects of equivalence ratio (Φ) on the peak pressure of a given configuration where examined for all 18 configurations. In all cases the mean values followed a parabolic trend across the range of values examined from a lean mixture ($\Phi = 0.9$) to rich ($\Phi = 1.3$), as shown in Figure 6.1. It was found that the majority of cases peaked about an equivalence ratio of $\Phi = 1.1$ with a few configurations obtaining peak values in a slightly more rich mixture of $\Phi = 1.15$. For all configurations the following parameters were constant; flow rate, fill time, settling time and flap venting times.

A typical spread of results is shown for configurations 5 and 9 below in figure 6.1. Peak pressure at both locations is plotted against equivalence ratio and clearly shows a parabolic trend centred on an equivalence ratio of $\Phi = 1.1$. From these results stemmed the conditions for all future experiments, namely that that the air fuel mixture was at stoichiometry, independent of configuration.
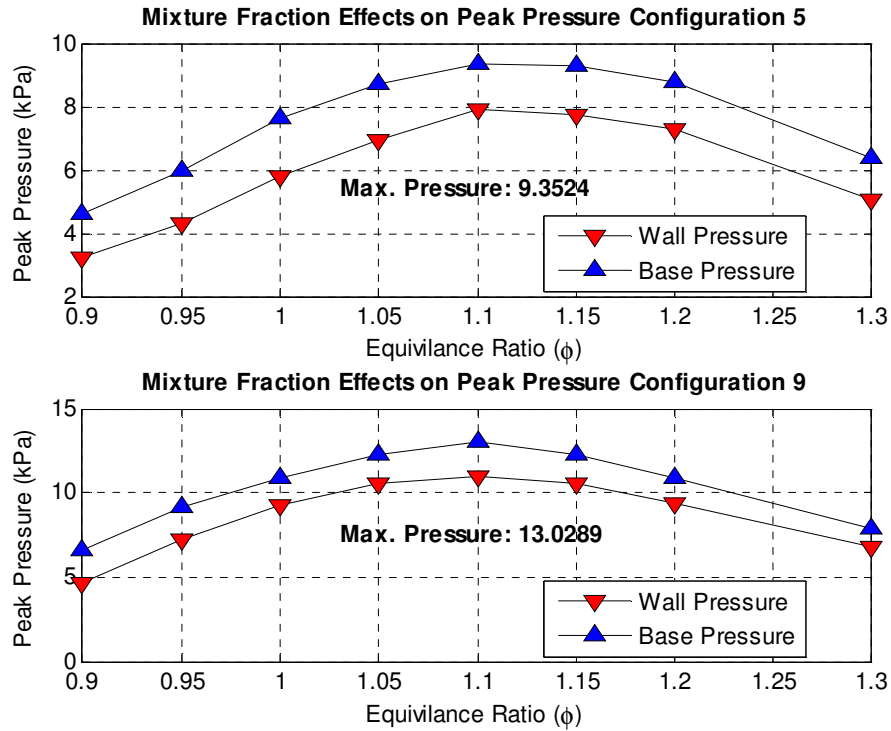
Figure 6.1: Equivalence Ratio Variation

6.2 PRESSURE RESULTS

Pressure time traces are shown below for all 18 configurations. The exceptional repeatability in all cases is highlighted in all cases. One aspect that is interesting to note is the acoustic effect evident in the resonance oscillations post peak pressure.
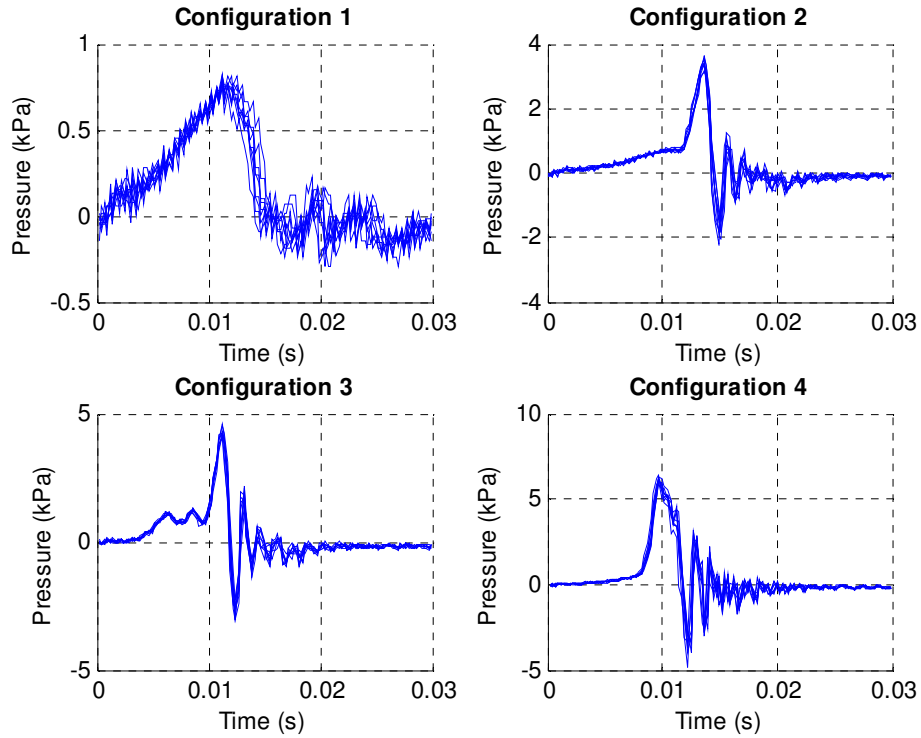
Figure 6.2: Pressure Time Traces Configurations 1 to 4
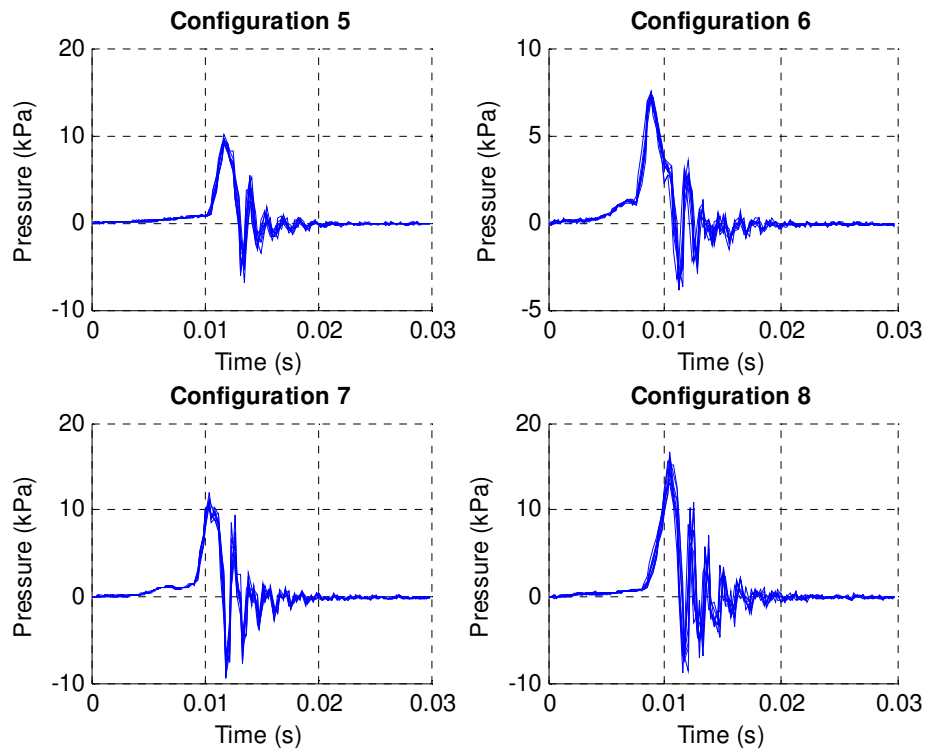

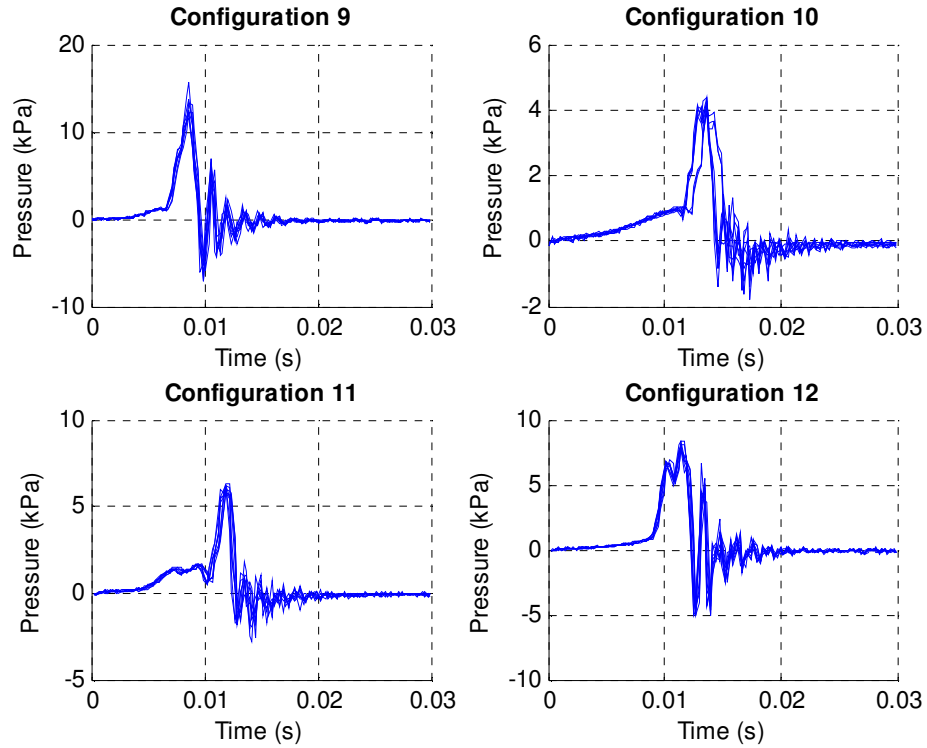Figure 6.3: Pressure Time Traces Configurations 5 to 8

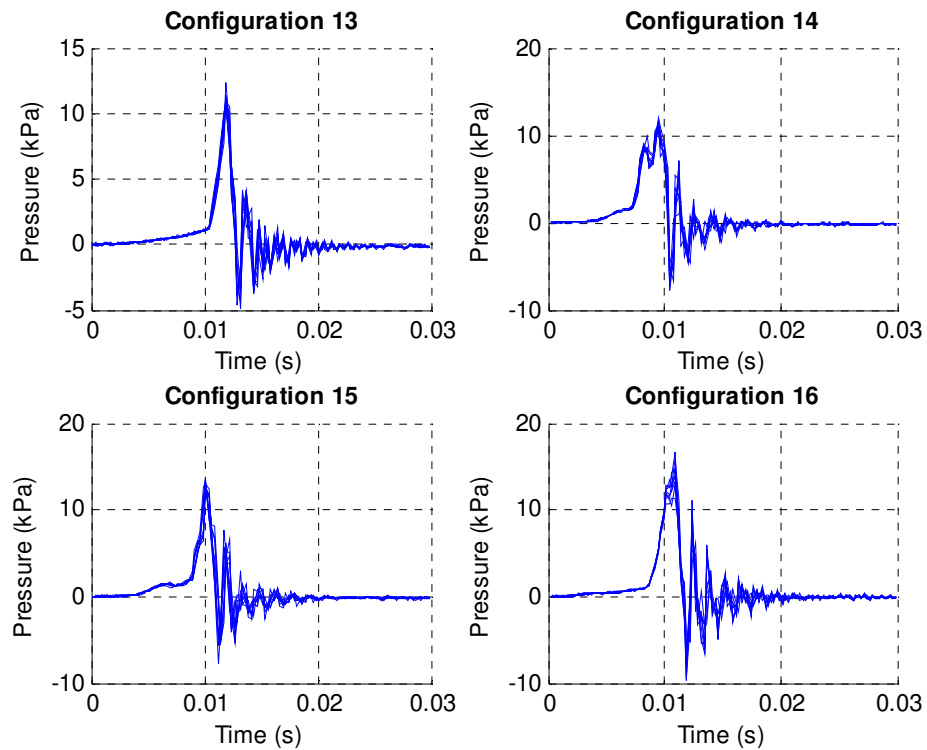Figure 6.4: Pressure Time Traces Configurations 9 to 12

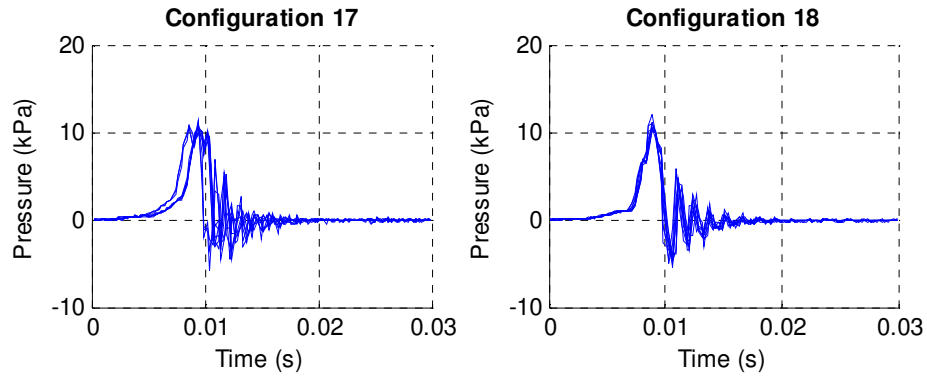Figure 6.5: Pressure Time Traces Configurations 13 to 16

Figure 6.6: Pressure Time Traces Configurations 17 and 18

For configurations 10 and 17 the processing algorithm used has an error associated with the first and second peak, in that the peak pressure is no longer clearly defined and thus the data is not aligned consistently. The code found maximum values for which to align T with, in the case where two points in the flow exhibit this property, perfect correlation between individual realisations does not occur. This ambiguity with peak pressure has no relevance to the average maximum data being collected and only affects the aesthetics of the presented graph.

Configuration Layout							
Config.	1	2	3	Obstacle	Peak Pressure (kPa)	Time to Peak (ms)	Duration of Stage 1 (ms)
1	-	-	-	-	0.7916	0.4168	N/A
2	-	-	-	S	3.4005	2.8747	11
3	Y	-	-	S	4.2804	3.9221	5
4	-	Y	-	S	6.1396	3.8596	8
5	-	-	Y	S	9.3491	7.9034	10
6	Y	Y	-	S	7.332	4.1711	5
7	Y	-	Y	S	10.8838	9.1472	5
8	-	Y	Y	S	15.0504	12.7128	8
9	Y	Y	Y	S	12.9848	10.9624	5
10	-	-	-	B	4.181	3.9934	12
11	Y	-	-	B	6.0557	5.4532	5
12	-	Y	-	B	7.9779	7.7806	9
13	-	-	Y	B	11.1068	8.4496	10
14	Y	Y	-	B	11.258	9.0255	5
15	Y	-	Y	B	13.0322	10.7661	5
16	-	Y	Y	B	14.1208	12.1085	8
17	Y	Y	Y	B	10.5669	8.9564	4
18	Y	Y	Y	-	10.7711	9.1395	4

Table 6.1: Peak Pressure Results

6.3 PRESSURE TRENDS ACROSS FAMILIES

For the purposes for turbulent analysis the 18 configurations were broken up into families that follow a logical grid progress or turbulence increase. For single grid configurations the baffle plate is moved from it proximal location near the point of ignition to that of the distal just upstream of the obstacle. All families are outlined in section 4 and as an image over each graph.

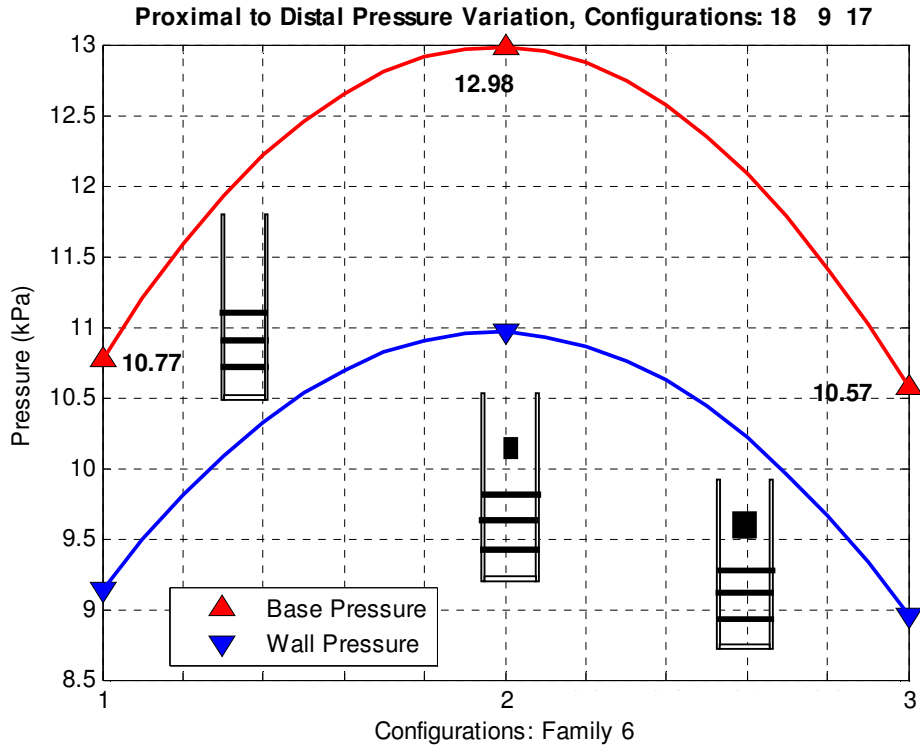Ross Hall Turbulent Combustion

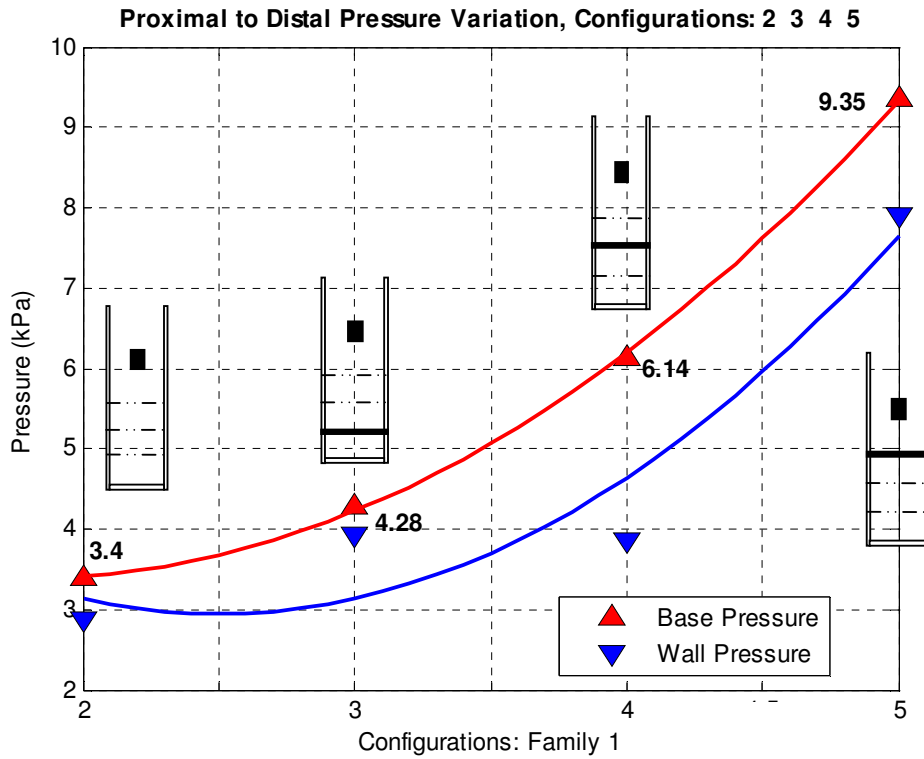Figure 6.7: Family 6 Peak Pressure Comparison

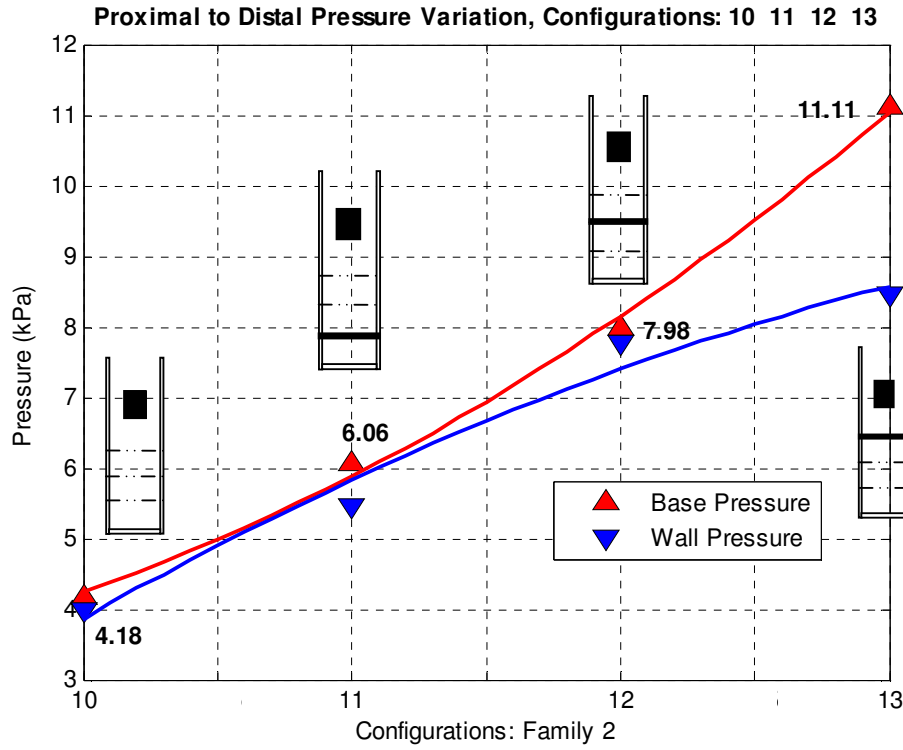Figure 6.8: Family 1 Peak Pressure Comparison

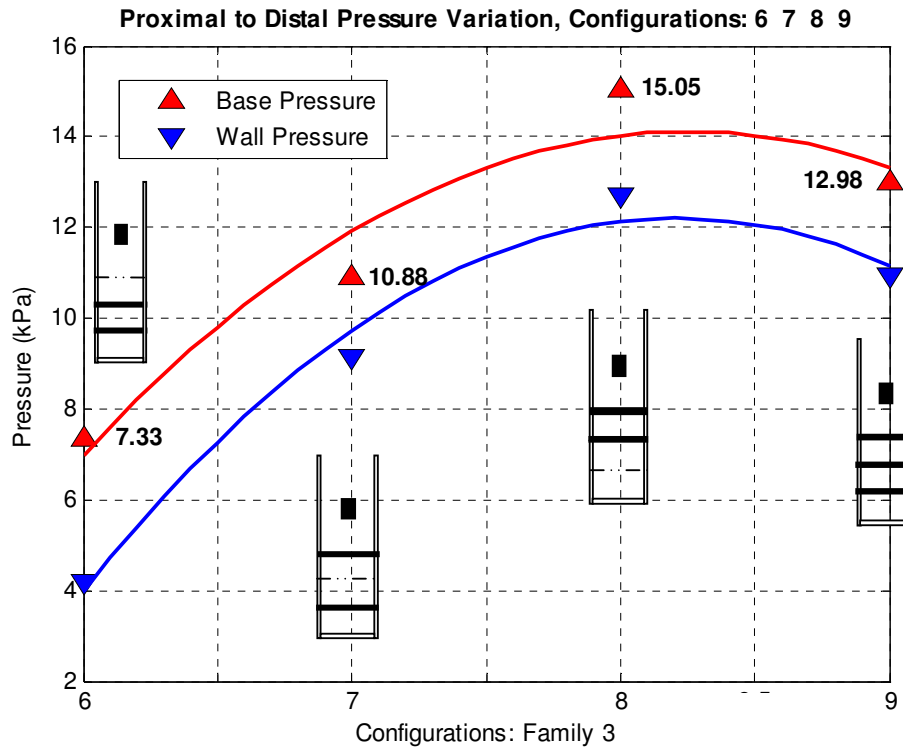Figure 6.9: Family 2 Peak Pressure Comparison

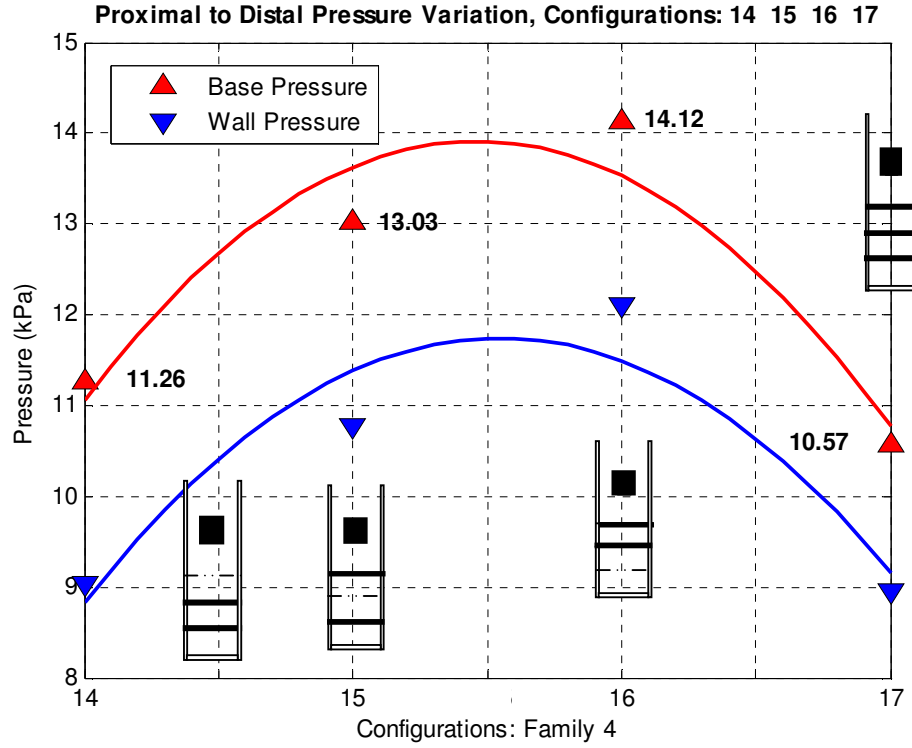Figure 6.10: Family 3 Peak Pressure Comparison
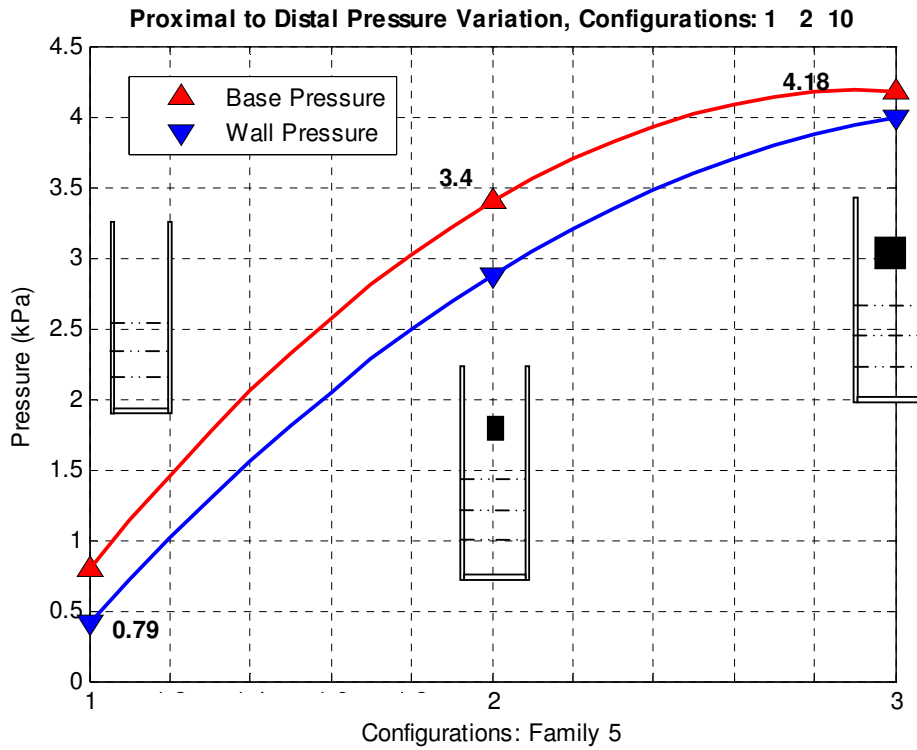
Figure 6.11: Family 4 Peak Pressure Comparison

Figure 6.12: Family 5 Peak Pressure Comparison

6.4 VELOCITY RESULTS

Velocity data is only available for a limited number of the configurations as the data sets were not collected concurrently. For the available configurations validated velocity data points are plotted with the mean profile and the relative turbulence intensity. The method used to calculate the RMS or turbulence intensity is a derivative from individually fitted polynomials, as outlined in the section 5.3.2 that are used to act as a high pass filter.

Results for both configurations 6 and 8 show significant evidence of insufficient particulate material being seeded into the flow, consequentially there was a low signal validation rate during the data collect process. Unavoidably any detailed quantitative analysis for these configurations is not a true representation of the flow field characteristics, however the data does add qualitatively to that of configurations 2 and 7. These results show that velocity of the flow in the channel peaks in a similar fashion to that of the pressure time traces.

Figure 6.13: Configuration 2 Longitudinal Velocity

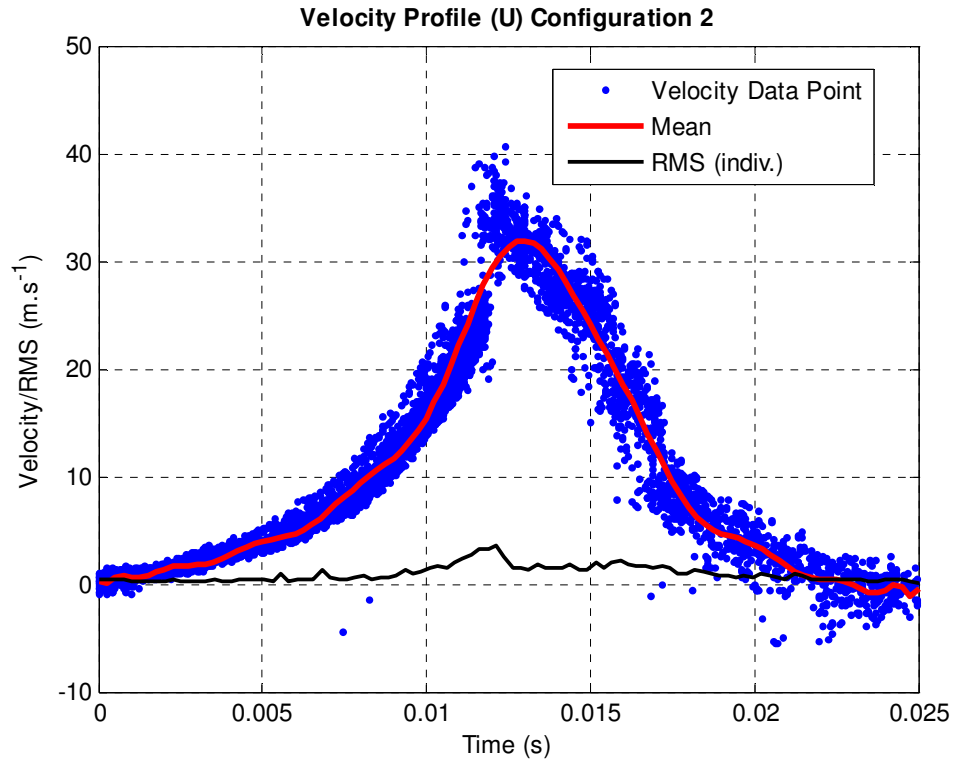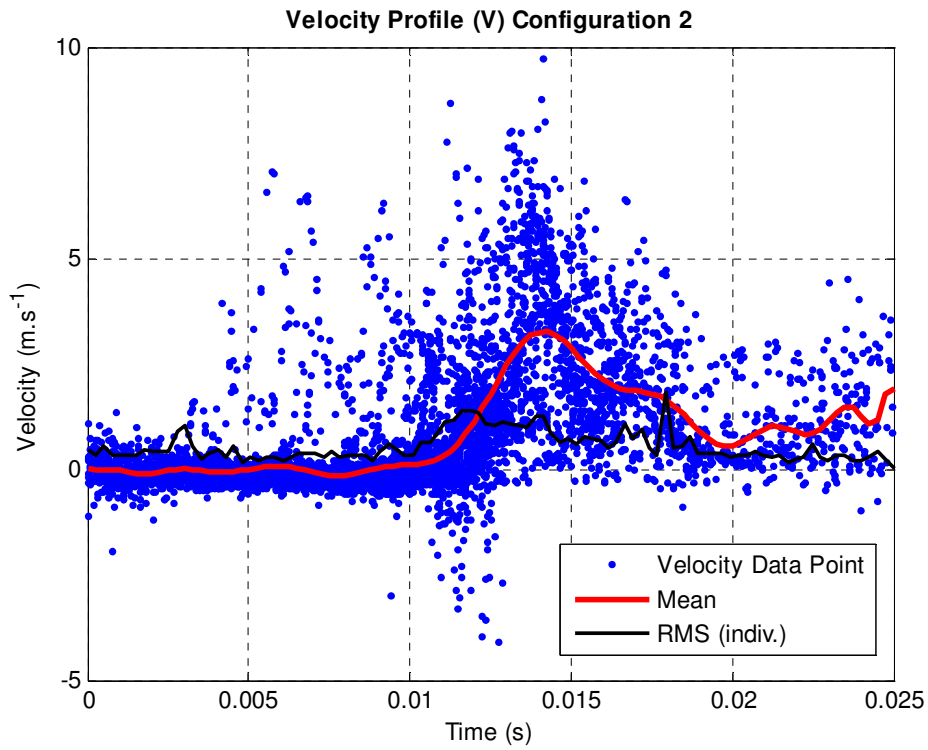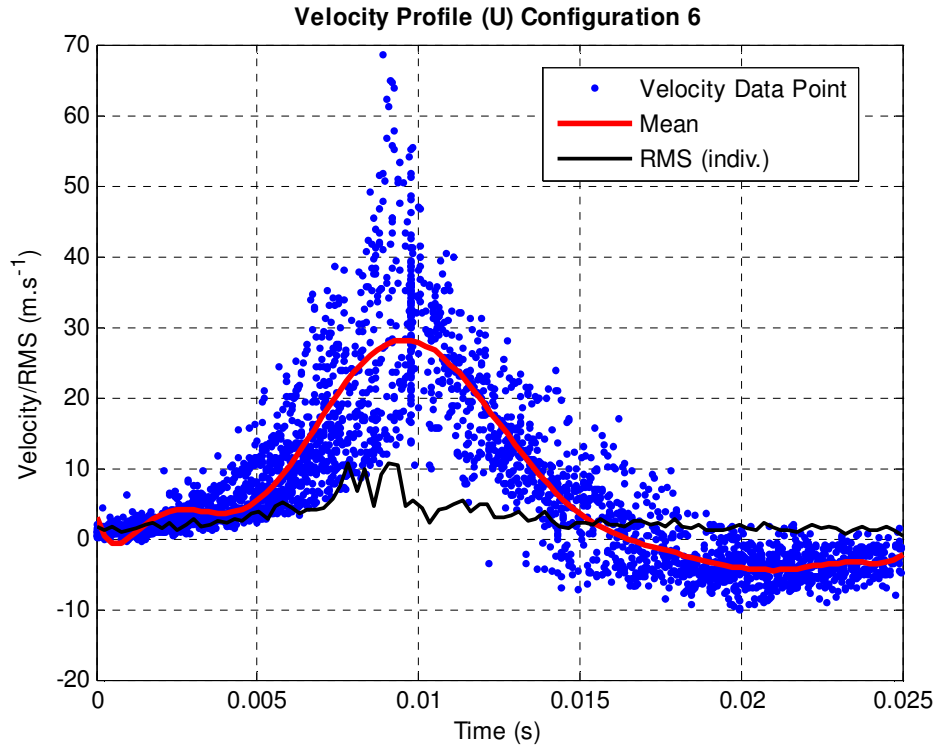Figure 6.14: Configuration 2 Transverse Velocity

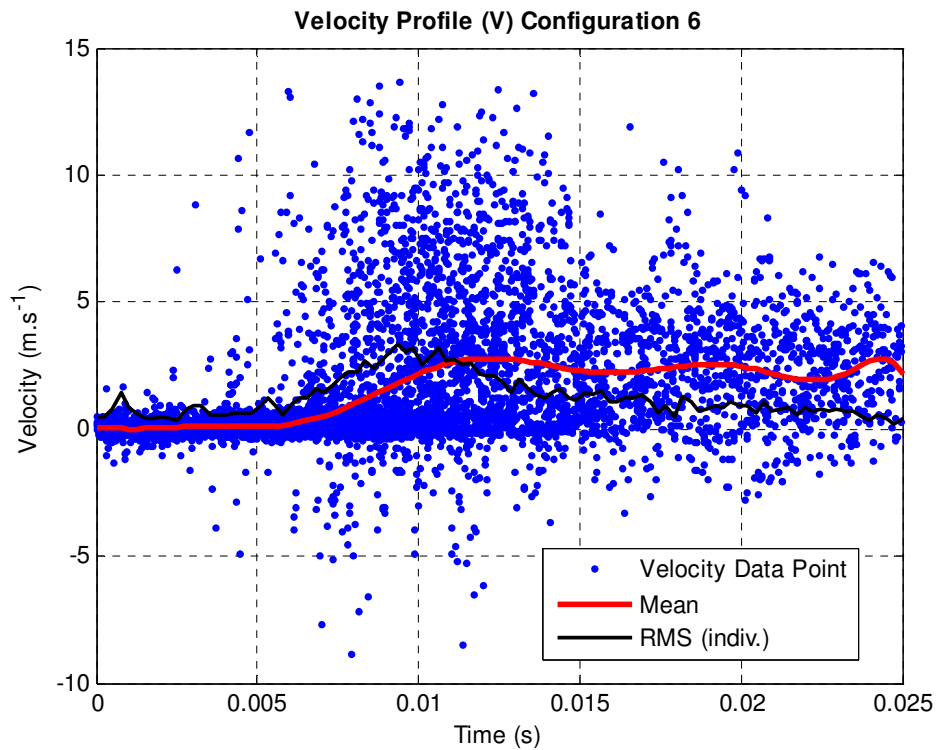Figure 6.15: Configuration 6 Longitudinal Velocity

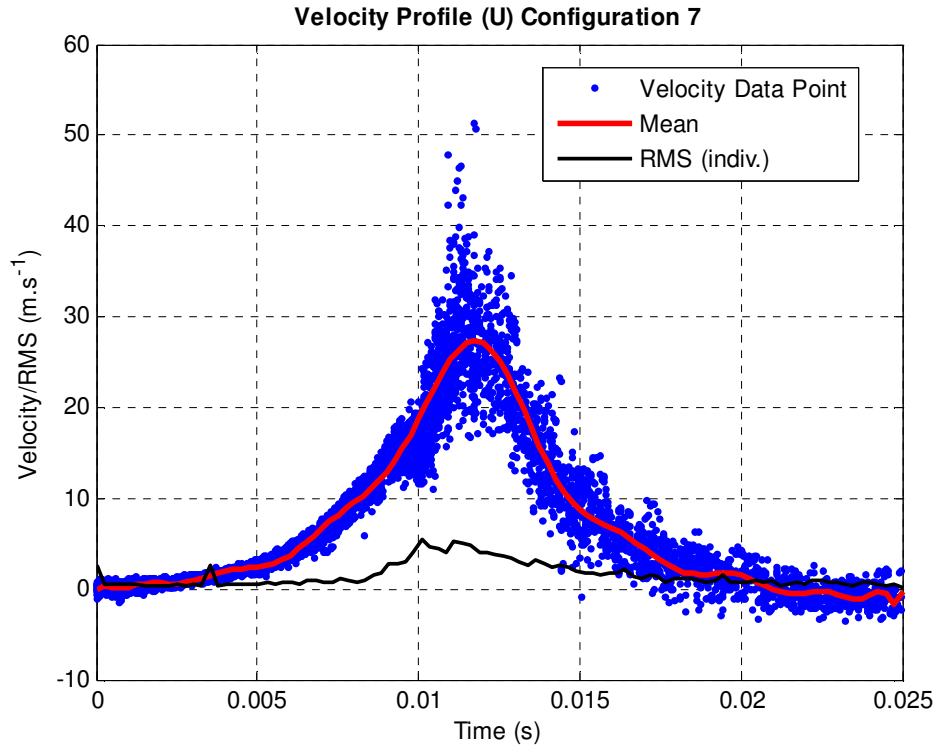Figure 6.16: Configuration 6 Transverse Velocity

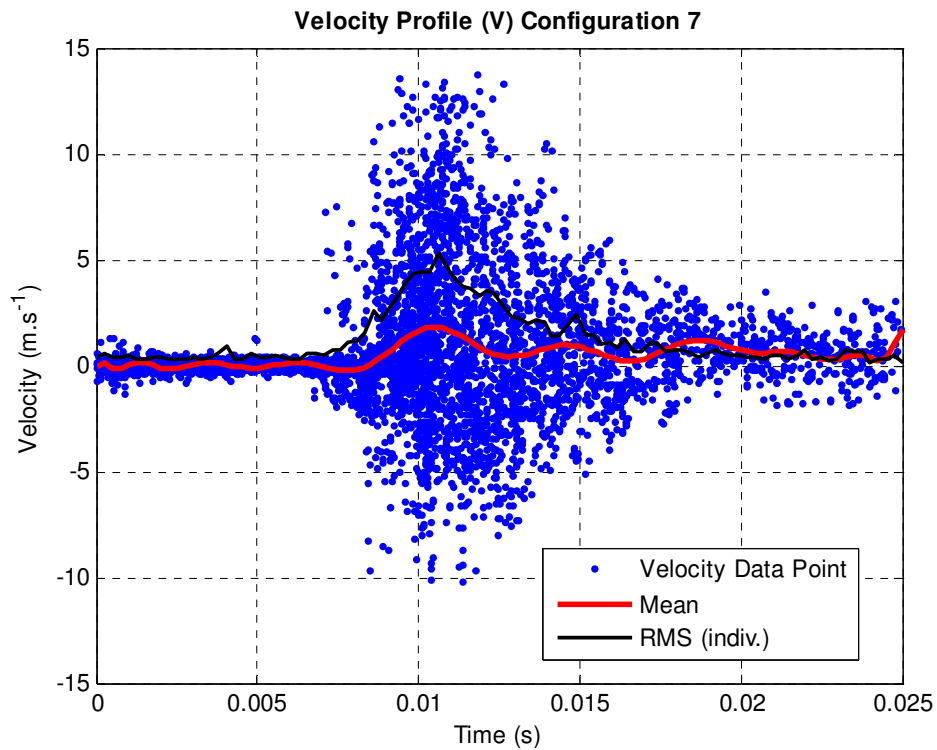Figure 6.17: Configuration 7 Longitudinal Velocity

Figure 6.18: Configuration 7 Transverse Velocity
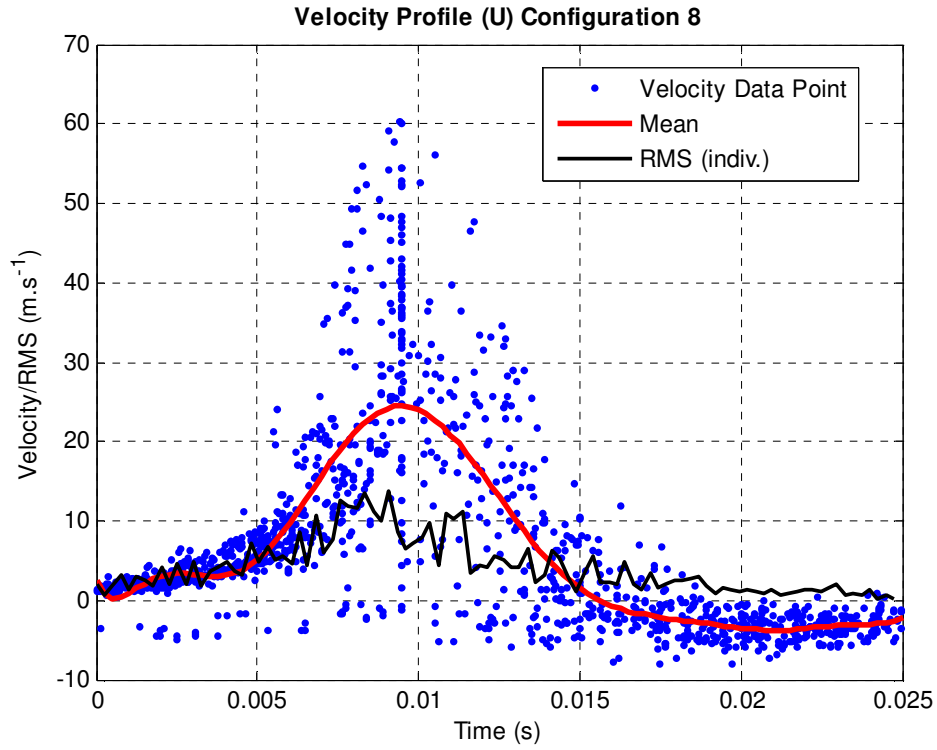
Figure 6.19: Configuration 8 Longitudinal Velocity
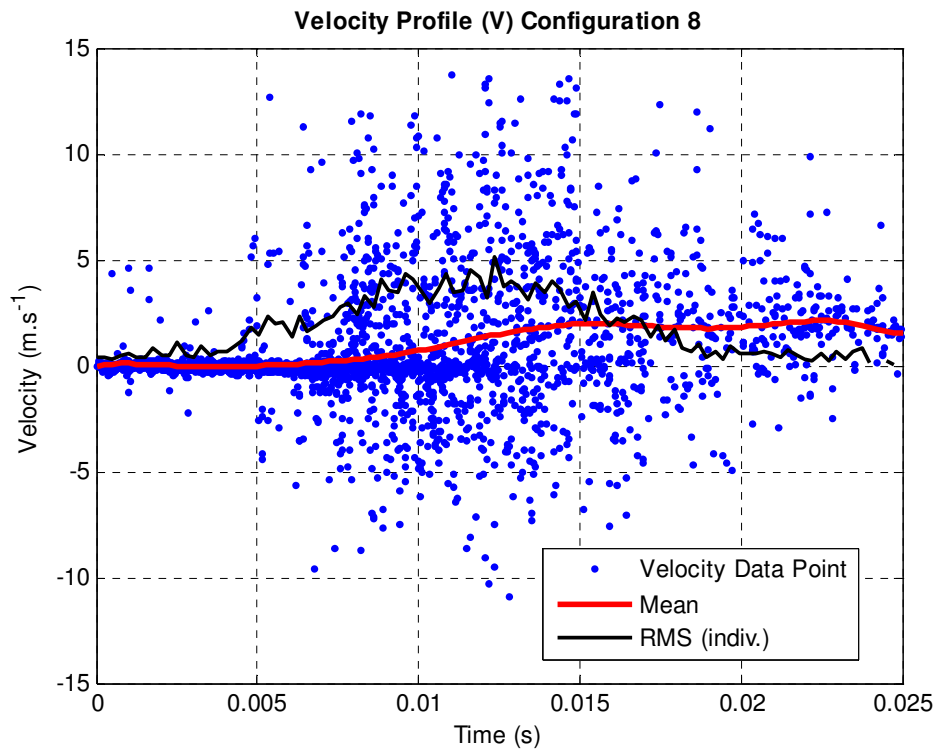
Figure 6.20: Configuration 8 Transverse Velocity

6.5 FLAME FRONT IMAGES

Laser-Induced Fluorescence images are the final independent data set used for flow field analysis. Again data was only collected for a limited number of configurations chosen to create a conglomeration of results with the velocity and pressure data already collected. In all cases the image bounds are confined by the quartz window inlayed into the side of the combustion chamber and include a portion of the obstacle along the lower edge. The location of the obstruction on the image does not remain constant due to the necessity to relocate the rig every time normalisation is required. Although 200 images were captured for each configuration only a select few have been reproduced in this section with the majority appearing in Appendix H. In all cases a selection of data has been used to give an indication of the flame fronts progression down the chamber and as it interacts with the recirculation zone behind the obstruction. All results are available on the accompanying data compact disc.
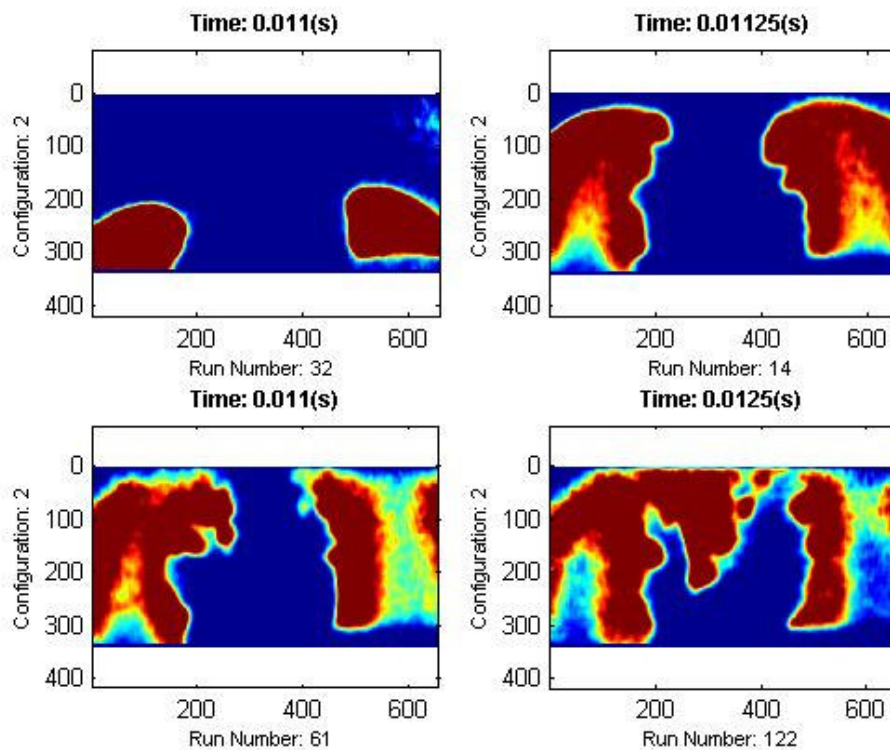
Figure 6.21: LIF Images for Configuration 2
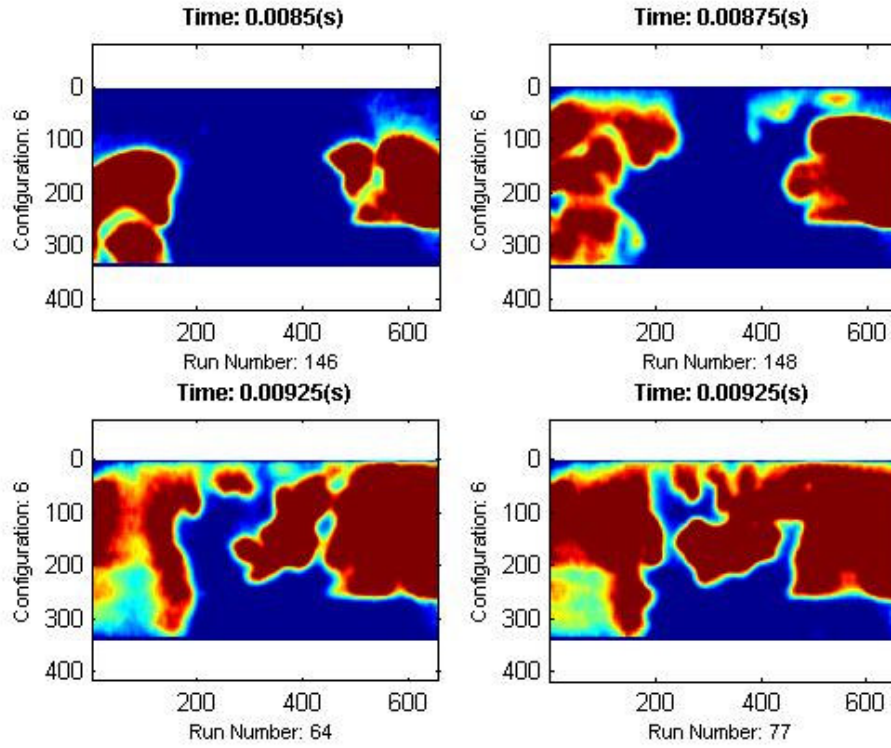
Figure 6.22: LIF Images for Configuration 6
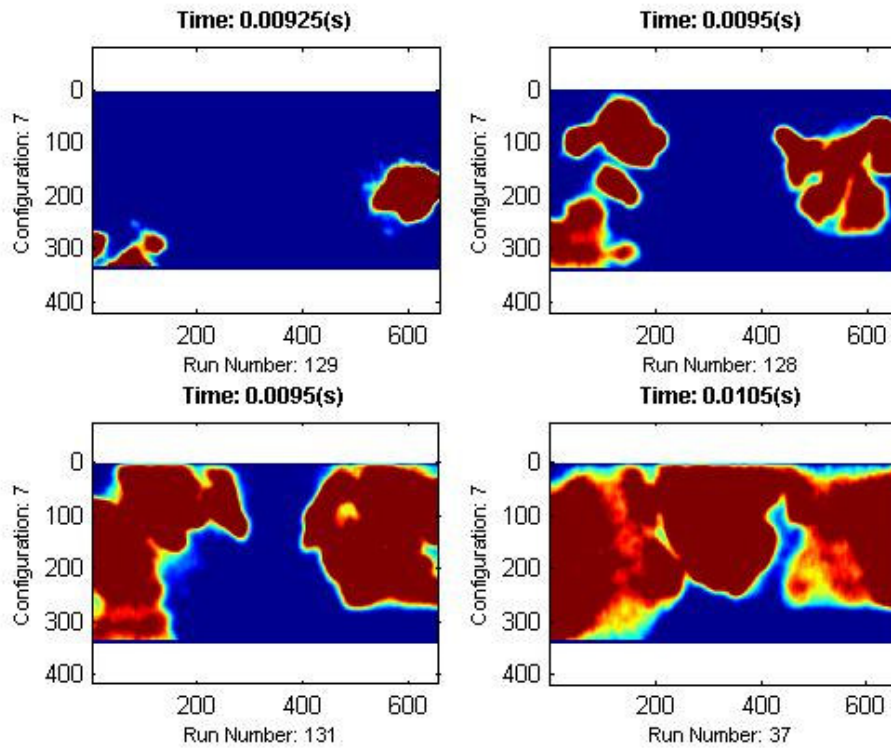
Figure 6.23: LIF Images for Configuration 7
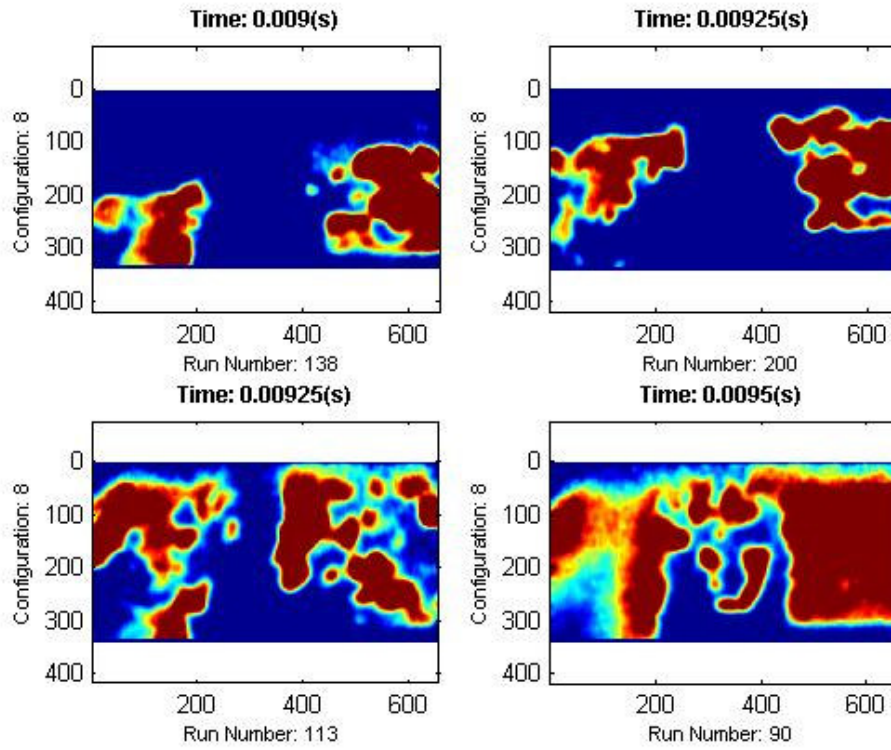
Figure 6.24: LIF Images for Configuration 8
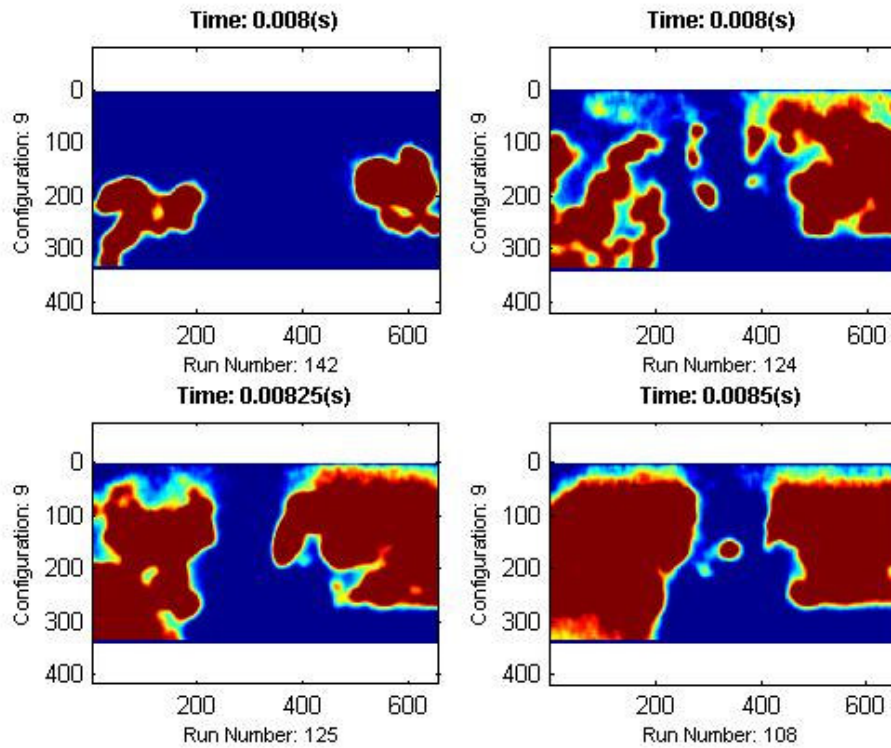
Figure 6.25: LIF Images for Configuration 9

7. DISCUSSION

7.1 EXPERIMENTAL HYPOTHESIS

This research combines data from past works with those recently colleted using current advanced laser diagnostics techniques, both utilising the smaller more practical combustion chamber, and therefore providing further insight into the nature of turbulent premixed combustion. The experimental hypothesis of this thesis combines additional laser diagnostics to improve and develop theories specifically associated with a transient premixed flow. This thesis is proposing the hypothesis that:-

1. Large number of grids will affect the flame front structure and characteristics in ways that heighten and inflate maximum pressure and RMS values.
2. The location of the grid is also responsible for inflating values related to peak pressure and velocity.
3. Turbulence is an underlying critical parameter that is affected directly by the above conjectures (1) and (2).

The following section discusses the results presented in Section 6 above and provides insight into the various hypothesises proposed. The discussion examines and expands on individual detail within the time profiles, flame front images and RMS calculations.

7.1 PEAK PRESSURE VARIATION

7.1.1 Effects of Grid Position (Single Grid)

Single grid configurations allow analysis of grid location specifically on peak pressure values. For this research obstruction size and therefore blockage ratio was also examined to determine the underlying factors influencing the flow parameters. With reference to Figures 6.8 and 6.9 in section 6 and Figure 7.1 below, analysis of the effect of the inclusion and then progressive distal variation of a single baffle plate is possible. In the case of the small obstacle, a positive tend is observed as the grid location is displaced further downstream from the ignition point. The non-linear nature of the curve is also noted, thus highlighting the influential location to be further downstream and just ahead of the main obstruction.
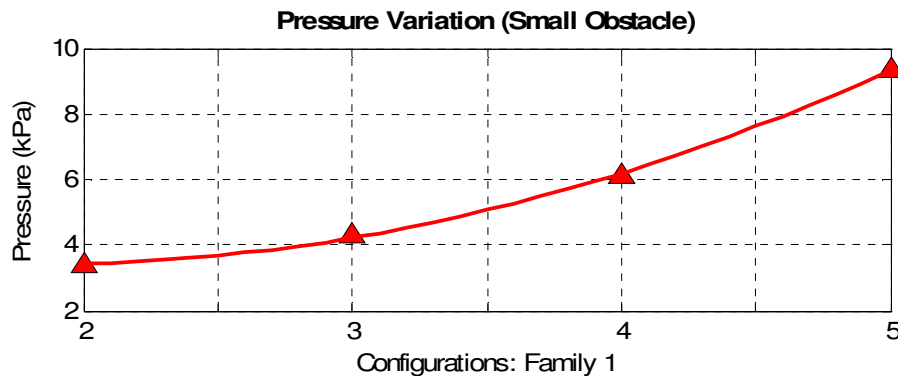
Figure 7.1: Family 1 Pressure Variation

Closer examination of the peak values for the configurations in relation to the non-linear trend shows that from the absence for any grid to the inclusion of a baffle plate just down stream of the ignition point only slight peak increases are observed. From configuration 2 (no grid) to configuration 3 (1 grid, location 1) a 26% increase results from peak pressures of 3.4 and 4.28 kPa respectively. Conversely, configuration 4 (1 grid, location 2) with a peak pressure of 6.14 kPa and configuration 5 (1 grid, location 3) with a peak pressure of 9.35 kPa, illustrates a significant 52% rise. This represents a substantial result suggesting that grid location has a more

important role to play in peak overpressures than simply the addition of a grid proximal to the ignition point.

This trend is also true for the large obstacle results over the same pattern of grid configurations, thus altering the blockage ratio of the chamber. Figure 7.2 shows the results for peak pressure plotted to accentuate the effect of a change in blockage ratio. Although the aforementioned argument regarding grid placement still holds, the absolute values have increased by approximately 30%. Thus the 25% increase in blockage ratio has an effect on peak values of a similar order to that of distal grid placement.
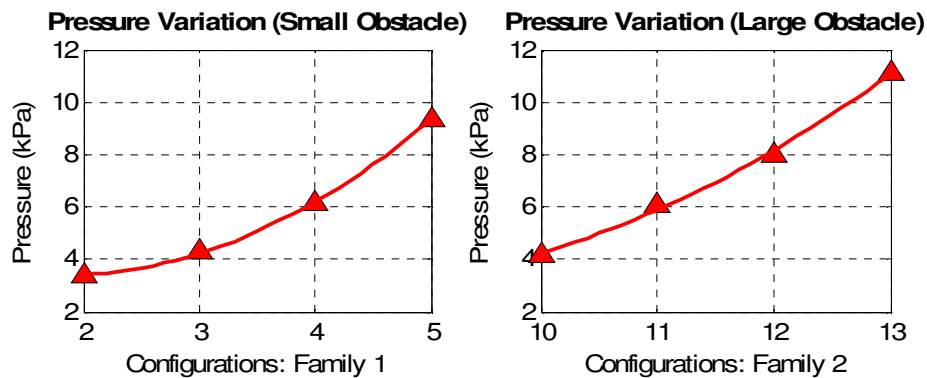
Figure 7.2: Small to Large Obstacle Comparison for Single Grid Configurations

Considering the flame front interactions on a local level, theses results can be justified. In the case described above with the comparison between a no-grid configuration (2) and that of a single grid located just downstream of the ignition point (3), both theoretically have a similar degree of disturbances by the time the front impacts the main obstacle and hence similar pressure results. For configuration 2 the initial kernel develops without impediment and propagates down the chamber to finally impact with the main obstacle causing the flow to split and progress through the channels. This, as can be seen by the pressure time traces in figure 6.2, is very slow in comparison due the relatively small hemispherical reaction zone. In contrast, configuration 3 has a developing kernel that immediately impacts with the first grid, creating a low level localised turbulence field with presumably a relatively low Reynolds number due to the slow forward velocity as can be seen from the calculation below. As the flame front egresses from the baffle plate and due to the low Reynolds

number, the flow has enough time to potentially re-laminarise before impacting the obstacle. Therefore the fingers that are produced at the exit of the baffle plate have limited effect on the flow as it enters the channels and into the recirculation zone. Assuming a temperature of 1200K and the incompressible density of air at an approximate egression velocity of 30m/s the follow equation estimates the Reynolds number.

$$Re = \frac{\rho VD}{\mu}$$
$$Re = \frac{1.2 \times 30 \times 0.012}{1.5 \times 10^{-4}}$$
$$Re = 2880$$

<div align="center">Equation 7.1: Reynolds Number Approximation</div>

Using this theory, configurations with grids further downstream are producing a more stochastic flow upon channel entry and thus modifying the upstream properties. This is due partly to the higher velocities at the grid location and therefore high Reynolds numbers, approximated as in Equation 7.1 to be in the order of 4320. As the flame front now has longer to develop and due in part to the proximal location of the obstruction, that is possibly preventing re-laminarisation the increase is justified. This conjecture is further developed with reference to the Laser Induced Fluorescence images taken downstream of the obstruction in the recirculation zone (reproduced in Appendix H).

7.1.2 Effects of Grid Position (Multiple Grids)

Analysis of dual and triple grid configurations further accentuates the previously discussed phenomena by inflating the peak flow values. This arises from already turbulent flow impacting on several downstream obstructions increasing the flows velocity as discussed above, before final interacting with the main obstacle. The flow dynamics now become complex as the departing fingers from the first grid propagates as a contorted flame front into the second and even third grid with out the possibility of re-laminarising. For configurations 6 through 8 inclusive, the trend proposed for single grid configurations still holds. This is that the progression of one

or more grids downstream towards the obstruction causes an increase in the peak overpressure. The dashed blue line in Figure 7.3 show that without the inclusion of configuration 9 (3 grids), the trend line for a polynomial of second order identical in nature to that of family 1 (Figure 7.1).
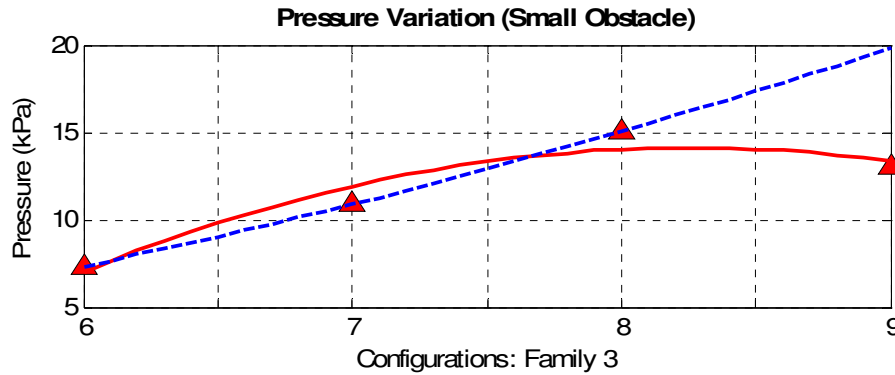
Figure 7.3: Family 3 Pressure Variation

Closer examination of the addition grids effect on the flow field parameters can show how the continual disruption of the flow prior to entering the channel, has a significant effect on the flow characteristics downstream in the recirculation zone. By considering the value of 9.35 kPa (Table 7.1) for a single grid adjacent to the obstacle and then comparing this to configurations 7 and 8, the effects for the second downstream grid can be examined. As stated previously, if a grid encountered a baffle plate while the kernel is still developing, the consequence is minimal as the flow has more time to re-laminarise. This is evident with configurations 5 and 7 only presenting a 16% pressure increase with the inclusion of the baffle plate in location 1, whereas for configurations 5 and 8, a considerable 61% peak pressure increase is observed. This characteristic accentuates both the significance of the second grid as well as the importance of location. Looking at Table 7.1 to reaffirm the notion that re-laminarisation occurs in a flame front left to propagate unimpeded, configurations 3, 6 and 7 are referenced. The addition of an adjacent grid, although interacting with a relatively slowly moving reaction zone, increases the maximum from 4.3 to 7.3 kPa which as a percentage is 69.7%. Introducing the downstream grid to location 3 however results in an immense 251.2% rise in overpressure and proves that without further interaction, the flame front has the time and space to re-laminarise before impacting the main obtruction.

Config.		1	2	3	Obs.	Peak Pressure (kPa)	Time to Peak (ms)
Family 1	3	Y	-	-	S	4.2804	3.9221
	4	-	Y	-	S	6.1396	3.8596
	5	-	-	Y	S	9.3491	7.9034
Family 3	6	Y	Y	-	S	7.332	4.1711
	7	Y	-	Y	S	10.8838	9.1472
	8	-	Y	Y	S	15.0504	12.7128

Table 7.1: Peak Pressure Comparison For Families 1 & 3

Finally considering the comparison between the small and large obstructions for the multiple grid configurations, a similar trend is established. In Figure 7.3, the increase in blockage ratio is independent of grid layout and simply results in an overall pressure increase, where as in Figure 7.5 below this same conjecture does not universally apply. For the less turbulent models such as configurations 6, 7, 14 and 15 the aforementioned conjecture is still applicable with an increase in peak pressure for corresponding grid layouts observed. The increased turbulence intensity in the remaining configurations follows the same positive trend when considering the dual grid configurations. The results for the three grid configuration however no longer follow the positive trend associated with increase flow disruption due to addition grids. As the flame front contortion intensifies, the effect on peak pressure becomes more benign and a reduction in values is observed. This is evident with corresponding configurations 8 and 16, and 9 and 17, where a 6.2% and 18.6% diminution results. These results suggest that although the turbulence is intensifying, the development and size of the eddies and vortices is now limited to the width of the channel between the obstacle and the chamber wall. Thus, the heightened contortion in the flow restricts the forward propagation into the recirculation zone and results in a reduction in overpressures. In addition to this, as the effect is more noticeable with the large obstruction as the great blockage ratio and therefore more constricted channel. Considering this situation in relation to the premixed regime diagram, configuration 17 maybe more complex than outlined above. Since the peak pressure is lower than that of configuration 9, which has a smaller obstacle, the flame maybe moving into, or indeed already has moved into a new regime of broken reaction zones.

Pressure Variation (Small Obstacle) | **Pressure Variation (Large Obstacle)**
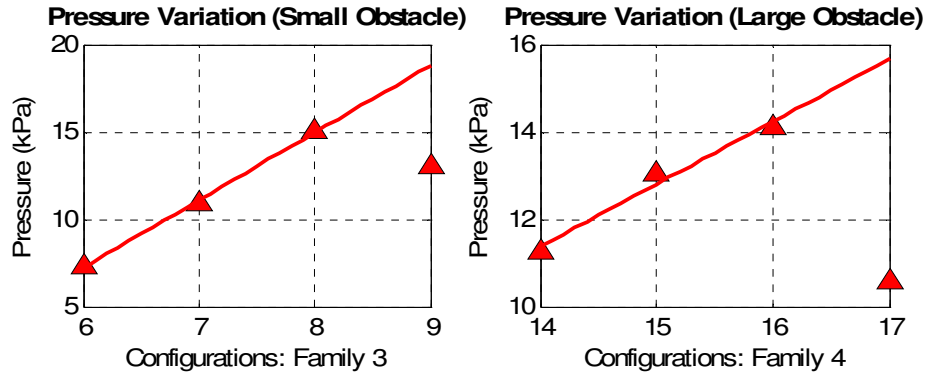
Figure 7.4: Small to Large Obstacle Comparison for Multiple Grid Configurations

7.2.3 Peak Pressure and Time to Peak.

Now considering the time taken for the flame to propagate through the various obstructions within the chamber gives an indication of the affect of grid location on flame speed and acceleration. Analysis of the time taken for the pressure time traces to reach peak overpressure values reveals trends inverse to that of raw pressure values as expected. The results for all families are plotted in figures 7.5 and 7.6 below with families being grouped so as to contain like sized obstacles. As can been seen both graphs show remarkable similarities between corresponding configurations in all cases. This then suggests that the down stream obstruction has little to no effect on the flame front development and propagation speeds, which must therefore be entirely influenced by the number and location of the grids. As a result it can be concluded that the by the time the flame front reaches the main obstacle the front is fully developed and propagating at similar velocities.

With reference to the absolute values of the time to peak from table 7.1 and graphically from the below figures, the influence of grid placement can be determined. For this analysis the progression of the reaction zone will be deconstructed into two stages, namely stage one, a laminar flame front and stage two, turbulent development from the first obstruction to the recirculation zone. From past work at the University of Sydney [36] high speed video camera images can be correlated with the presented data to confirm the location of flame front before entering the image bounds of the LIF image. It can be seen that whilst the reaction

zone remains laminar, the propagating flame front has little effect on the overall pressure values, and therefore an initial subtle increase in pressure can be attributed to the first obstruction or baffle plate. From the correlation established between LIF images and pressure time traces it can be concluded that the point of maximum pressure corresponds consistently to the consumption of the unburnt fuel behind the obstacle. This then provides a reference point for the commencement and conclusion of stage two.
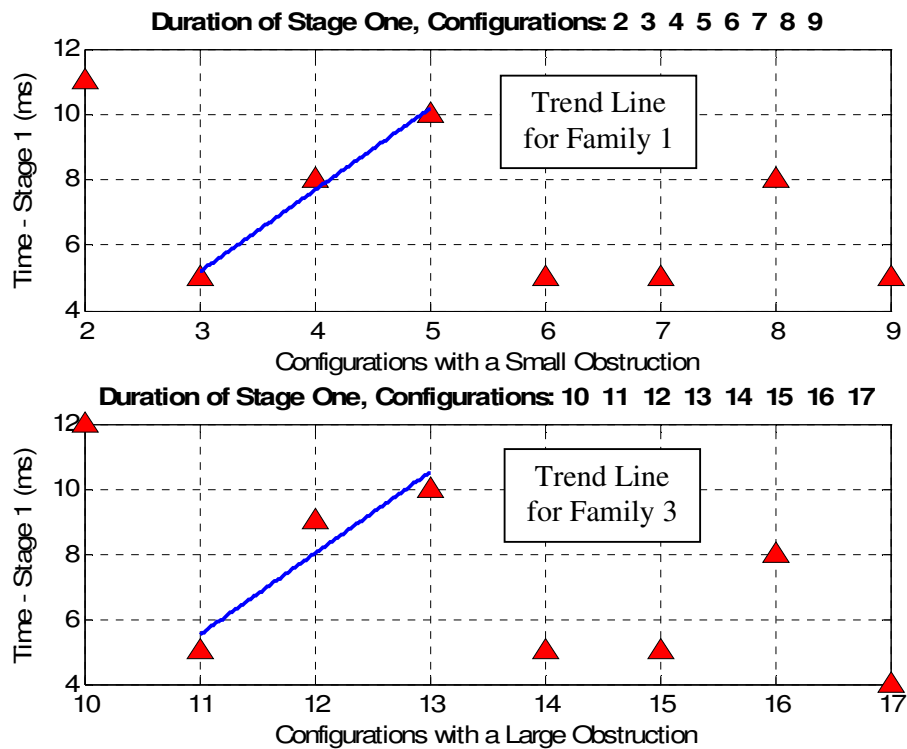
Figure 7.5: Duration Variation for Stage One

Firstly looking at the single grid configurations from both families, the flame speed is seen to increase dramatically with the introduction of a grid adjacent to the ignition point and continue in this trend until the grid is located in the most distal location. This is not directly proportional to that of the pressure values, which require the flame front to have already full developed before impacting a solid boundary in order to have maximum influence. In terms of speed and acceleration, disrupting the flow closer to the ignition point increases the acceleration and therefore the downstream velocity, with the maximum values occurring shortly after the kernel has

fully developed. In the case of configurations 3 and 11, the initial kernel is underdeveloped when the flame front impacts the first baffle plate thus limiting the overall flow disturbance. In contrast to this, configuration 13 shows how the flame front is aloud to propagate unimpeded down the chamber thus increase the duration of stage one before impacting the grid and obstruction. Examining the results for the duration of stage one in Table 7.1 and Figure 9 show this unequivocally, that is as the location of the first grid is moved down stream the time taken to impact the first grid increases positively. Therefore the duration of stage two from the exit of the first grid to peak pressure has to be non-linear thus accounting for the trends seen in Table 7.1. Although the effect of the downstream boundaries has a greater influence in terms of flow disturbance, the effect of speed and acceleration is minimal.
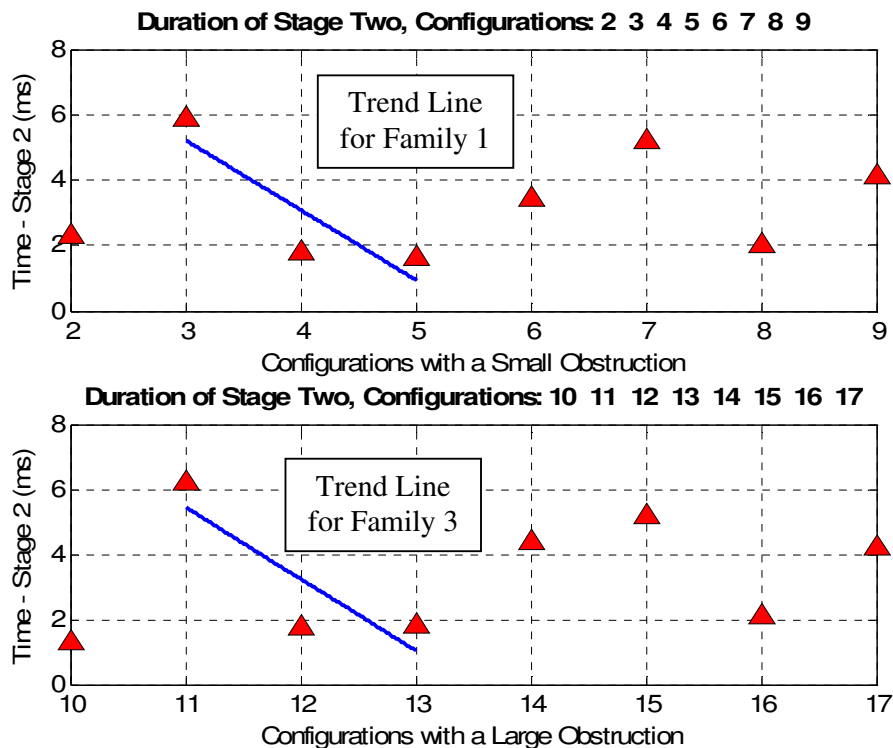

Figure 7.6: Duration Variation for Stage Two

Applying the same reasoning to the dual grid configurations, highlights the notion that the acceleration of a flame front is influenced most in the development stages. Configurations 6 and 14, where 2 grids were positioned adjacent to the ignition point, therefore limiting stage one and consequently reducing the time spend

in the laminar flame regime. This also demonstrates how the repeated disruption accelerates the flame front significantly, instead of allowing the front to partially re-laminarise and ultimately slow down as is evident in configurations 7 and 15. Considering this in terms of the flame fronts progression between the various development stages, in can be seen from the pressure time traces in section 6 that the location of the second grid is the crucial in ultimately accelerating the flow. As stated, the time to peak for configuration 6 is less than that of configuration 7, however closer examination of the data shows that the duration of stage one is identical and the variation entirely occurs during stage two. Specifically the absence of the immediate disruption in configuration 7 adds approximately 2 ms to the resulting plateau and therefore the time to peak, although the gradient may be enhanced in relation to that of configuration 6.

As expected, the results for single and dual grid configurations show remarkable correlation for the duration of stage and therefore confirm the conjecture that upstream obstructions have no effect on the developing flame front. Although the accuracy of the data presented for stage one duration in Table 7.1 is only to the nearest millisecond, the trends for upstream grid relocation and correlation between obstruction size still stands.

7.2 CALCULATED RMS AND TURBULENCE LEVELS

7.2.1 Calculated Turbulence Intensity Analysis

As LDV data is only available for a limited number of configurations, the theories developed describing peak pressure variations are going to be further analysed with reference to velocity trends. The multi-grid, small obstruction family is considered with deliberation to the base no-grid layout, configuration 2. Above it was established that the as the baffles plates progressed closer to the downstream obstacle the peak over pressure increased thus suggesting that the over all turbulence intensity had also increased. Simply by considering the peak values for RMS (Figure 7.7), it is evident that the conjecture does not apply as rigidly as for pressure trends. The graph

demonstrates no positive trend as is evident with the corresponding pressure data, especially for the longitudinal component of velocity and therefore an alternate analysis into the nature and shape of the RMS data needs to be sort. Simply considering the peak values, as in Figure 7.7, does not accurately describe the turbulence intensity or RMS because of the following reasons:-

1. The uncertainty in the RMS.
2. The fact that this data is a mean made at only a single location in the chamber. Realistically, turbulence should be measured just downstream of the baffle plates and at several locations to identify any correlation with overpressure results.
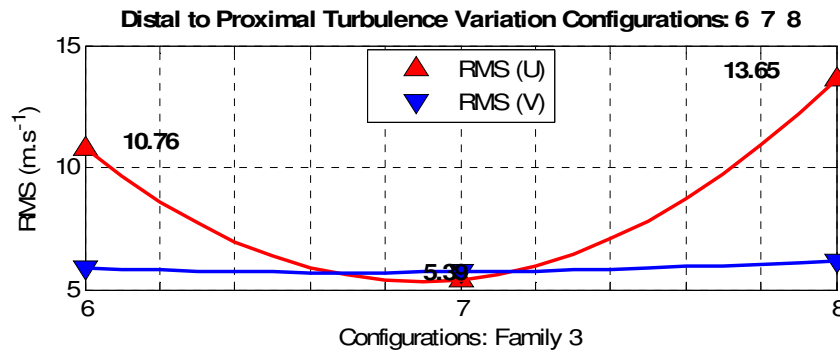

Figure 7.7: Peak RMS Values (Longitudinal and Transverse)

Due to the errors associated with the RMS calculation, spikes and oscillations in the data are common and primarily a result of the ensemble averaging and limited validation rates that are unavoidable. By examining the RMS profiles in detail, trends and characteristics can be deduced for individual configurations that lend to an educated analysis. Figure 7.8 illustrates the turbulence profile for the reference configuration without any baffle plates and only the small downstream obstruction. The profiles demonstrate low turbulence intensity in both longitudinal and transverse directions, specifically during the flame front development stages and acceleration to peak velocity from 5 to 15 milliseconds. Through this stage of propagation the flame front is progressing up the chamber to the obstruction and into the re-circulation zone. As expected the main variation and therefore maximum RMS occurs around the time the flame front enters the re-circulation zone as the length of the reaction zone

increases dramatically at the exit to the channel and is influenced more by turbulence intensity.

RMS (U) Configuration 2

RMS (V) Configuration 2
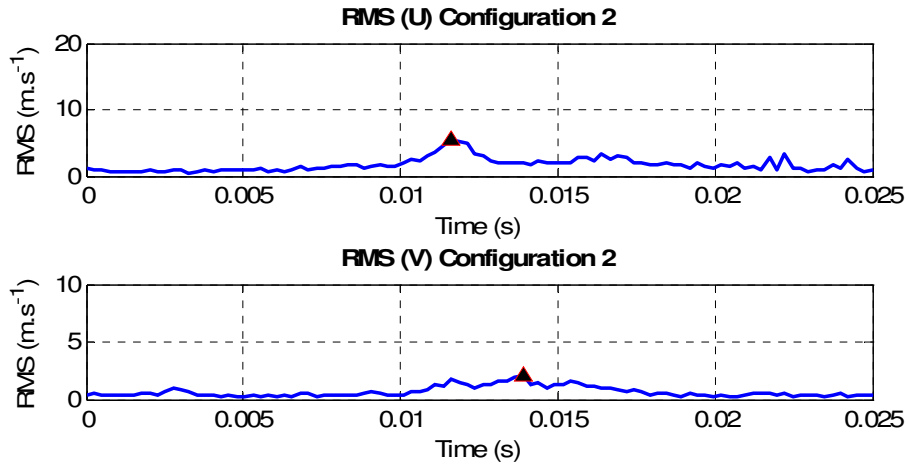
Figure 7.8: Two Dimensional RMS Profile for Configuration 2

Now considering the RMS profiles for configurations 6 through 8 of family 3, the differences and effects of turbulence are more pronounced. In both dimensions of the RMS an increase in the number of non-zero values has significantly changed the shape of the profiles in comparison to that of configuration 2 above (Figure 7.9). Although the point of maximum value is indicated, the feature of primary concern is cumulative summation of the values between 5 and 25 milliseconds.

Figure 7.9: Longitudinal RMS Profiles

Figure 7.10: Transverse RMS Profiles

The first point to emphasise is the quality of the longitudinal data collected for configurations 6 and 7, as a result the profiles are sporadic and do not follow a smooth line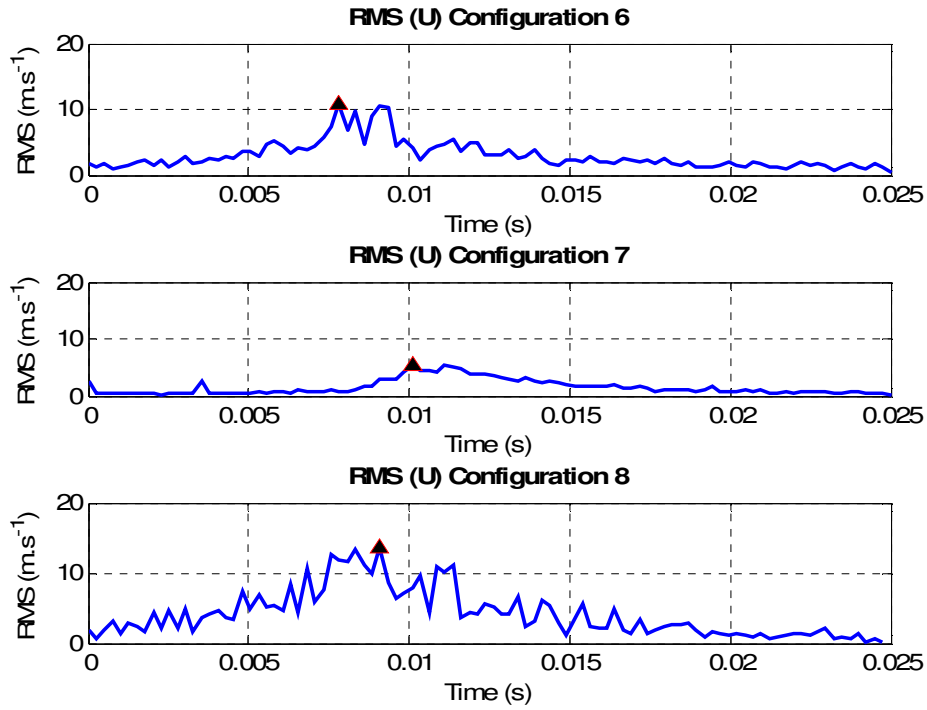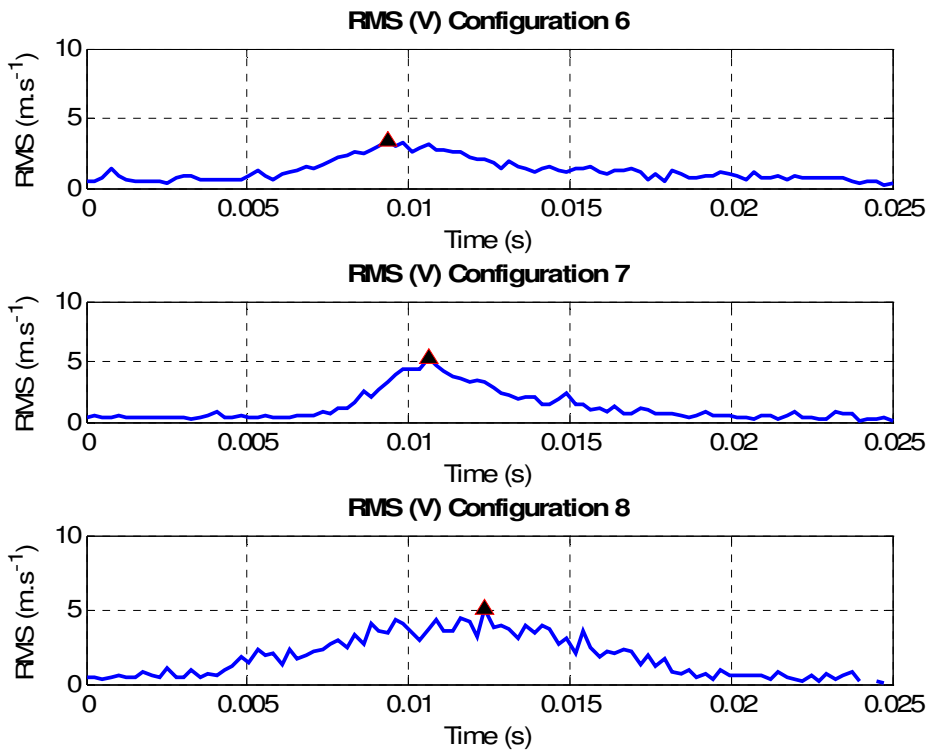. In contrast, the profiles for the transverse RMS are more regular with undulations increasing with turbulence intensity. For each set of RMS results the integral was calculated between 0.005 and 0.015 ms to give an indication of the cumulative turbulence intensity over the period of flame front development and recirculation zone interaction. This time period also eliminates errors associated with badly conditioned polynomials that occur predominately at the extremes for the data sample.

As highlighted, the results for the transverse velocity fluctuations follow the trend establish by the peak pressure values. Fluctuations in the transverse direction represent deviations from a common streamline as a consequence of the turbulent flow, this is in contrast to measured fluctuations in the longitudinal direction that indicate subtle changes in the forward velocity of the flame front. Although the longitudinal velocity changes are partly a result of the turbulence they also included variations due to kernel development as proposed previously and are therefore more susceptible to errors and poor seeding rates. The transverse velocity fluctuations however are independent of kernel size and instantaneous velocity rendering the data more useful for turbulence analysis. By using the trapezoidal rule to determine the area under the RMS curves, an indication into how the turbulence is influencing the flow in the long term can be determined. Collecting an integral of stage 2 (first grid to peak pressure) shows if the flow is being significantly influences over the course of this period. Table 7.2 below clearly demonstrates a positive correlation in both the peak pressure and the integrated RMS results for the transverse direction. Thus the notion that downstream grid location has a great effect on turbulence is again reaffirmed.

Configuration		1	2	3	Obs.	Peak Pressure (kPa)	Peak RMS (U)	Integrated RMS (U)	Integrated RMS (V)
2		-	-	-	S	3.4005	4.268	0.0135	**0.0067**
Family 3	6	Y	Y	-	S	7.332	9.551	0.0479	**0.0200**
	7	Y	-	Y	S	10.8838	6.099	0.0254	**0.0227**
	8	-	Y	Y	S	15.0504	10.47	0.0713	**0.0321**

Table 7.2: Integrated RMS Results

7.3 TURBULENCE AND FLAME FRONT CONTORTION

Finally the Laser-Induced Fluorescence images are used to examine in detail the formation and degree of flame front contortion as the reaction zone egresses from the channel and propagates into the wake behind the obstruction. Although quantitative analysis has not been performed on the presented images, detailed qualitative analysis gives an insight into the flame front shape, which provides a firm basis for discussion. The most significant comparison between corresponding images across the range of configurations is the enhanced contortion as the forward velocity increases and the average eddy size decreases. In all the LIF images reproduced for this analysis, the obstruction is located centrally along the lower edge of the figure with a slight variation in the longitudinal direction. Also the direction of the 283 nm pulse used to induce fluorescence traverses the image from left to right. The Laser-Induced Fluorescence images are explained in terms of flow direction and obstacle location in Appendix G.
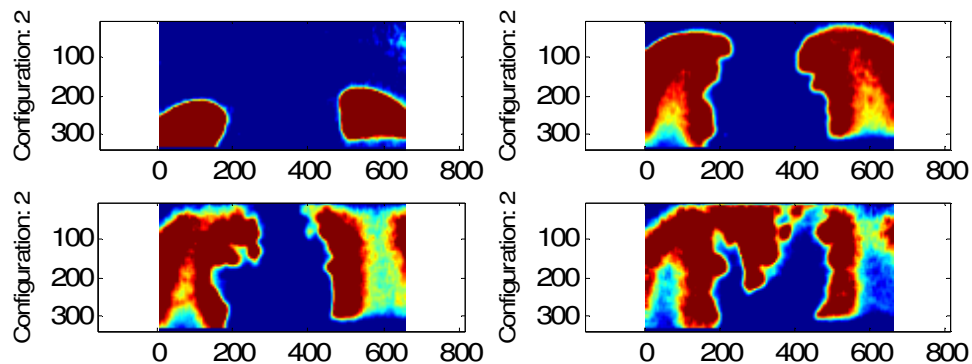

Figure 7.11: LIF Images for Configuration 2

Beginning the analysis by examining the control configuration (configuration 2), it can be seen that as the flame front egresses from the channel, little to no contortion is observed. This is typical and highlights the absence of upstream baffle plates disrupting the flow. As the propagating reaction establishes a shear layer between the fast moving flow from the channel and the static unburnt fuel in the wake, instabilities and eddies begin to form. These disturbances allow analysis of the flow within the recirculation zone as the unburnt mixture begins to be influenced by the adjacent flame front. This is highlighted in the lower left image of Figure 7.11 above, as the flame front curves back into the wake the unburnt fuel is forced to advance into the flank faster than the reaction rate, producing the swirling pattern as seen. The degree of contortion at this point indicates the size and number of the eddies in the turbulence and is dependent on both the shape and speed of the flame front at the exit of the channel.

Now by introducing baffle plates to the upstream flow, the shape and velocity of the front as it enters the image is drastically modified in contrast to the control data discussed above. The images below provide a comparative analysis of four images typical of those within data sets for each configuration and are displayed such that a single series progresses down a column of the given figure. From the emergence of the flame front into the image bounds it can be appreciated that the degree of contortion and flame front wrinkling has increased with the addition of the turbulence generating grids. Qualitatively, it can be seen that the integral length scale has increased relative to that of configuration 2 and that the amount the flame front has filled the space or the statistical fractal dimension has also been amplified. Examining the corresponding images from configurations 6 through 9, Figures 7.12 and 7.13, shows that this increase in flame front contortion is quite apparent. As the turbulence intensity increases at the entrance to the channel the degree of recirculation within the reaction zone also intensifies, as is demonstrated in the upper right hand image of Figure 7.13. The LIF in this case suggests that the major component of velocity is not in the longitudinal direction as expected and instead is following a contorted and closed loop streamline. This, in comparison to the semicircular flame front of configuration 2, indicates the significant downstream disturbances and thus reaffirms the conclusion obtained from both the pressure and velocity data.

It should also be noted that the final images of each set do not exhibit the equivalent degree of flame front variation and in fact begin to present very similar results. Even for configuration 2, by the time the reaction zone impacts the recirculating wake behind the obstruction the degree of flame front wrinkling has increased significantly. Although not conclusive from figures 7.11 through 7.13, results reproduced in Section 6 do indicate such a phenomena and insinuate independence between recirculation properties and those downstream.
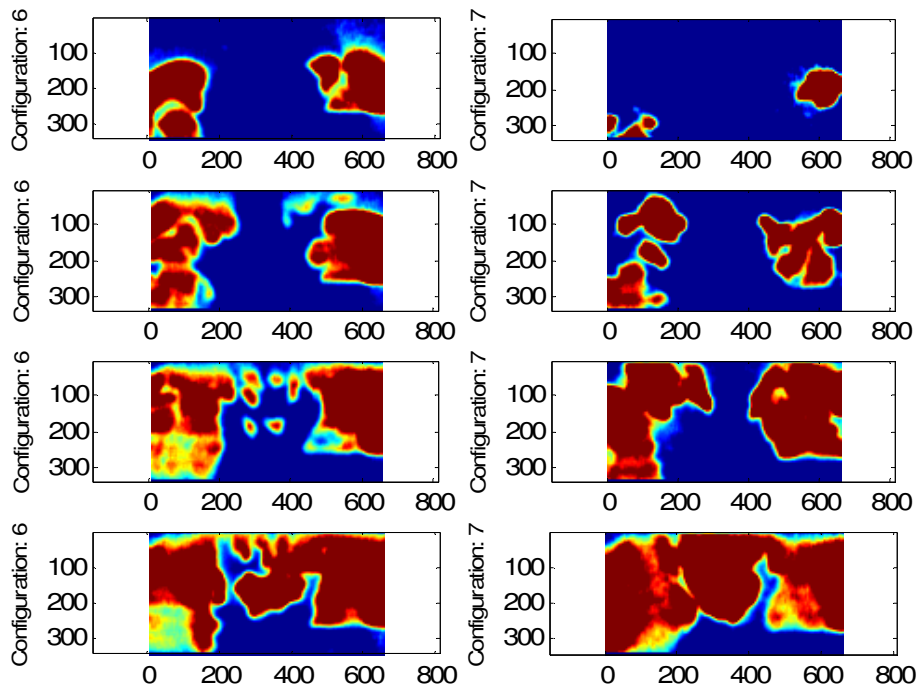

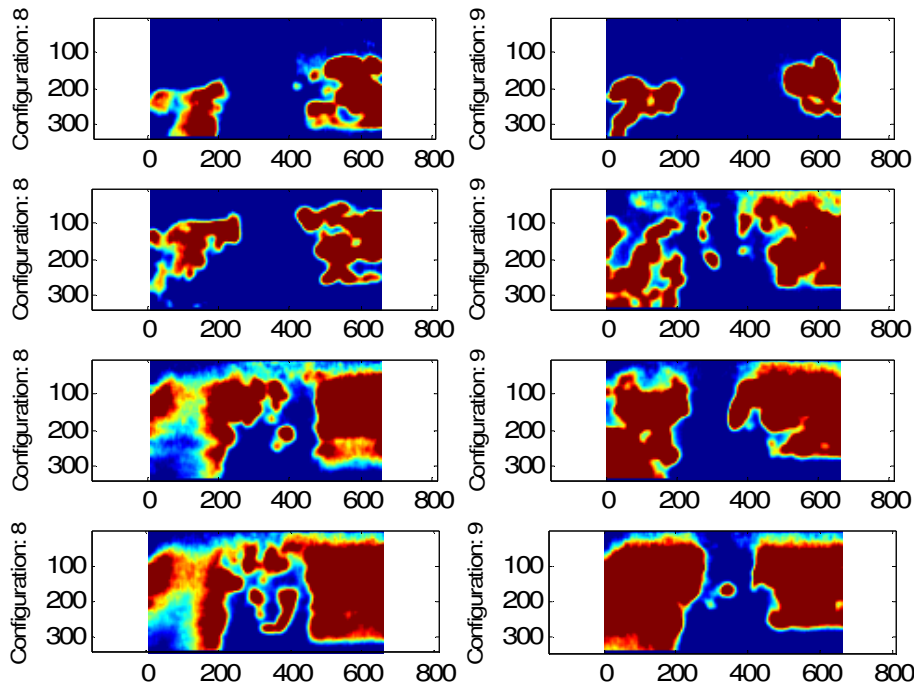Figure 7.12: Comparative LIF Images for Configurations 6 & 7

Figure 7.13: Comparative LIF Images for Configurations 8 & 9

One feature of these images that is accentuated above that is a direct result of increase turbulence intensity is the development of flame front contortion in the third dimension or out of plane motion. In a large portion of the images the third dimension of the flow out of plane produces effects that are apparent with the abundance of high concentration OH in small pockets. Closer investigation of these pockets in relation to location, size and flame front wrinkling reveals several possible reasons for such results:-

1. Flame front wrinkling in the third dimension
2. Detached flamelets
3. Auto-ignition or spontaneous combustion

In many cases the presence of out of plane wrinkling is obvious from inspection however distinguishing between detached flamelets and auto-ignition without further data, namely temperature and LIF of alternate reaction products, is inconclusive. Images such as 1 of configuration 6 and 2 of configuration 7 in

Figure 7.12 are fantastic examples of three dimensional flame front contortions that the laser sheet has cut through. The presence of this wrinkling further implies the heightened levels of turbulence with the addition of baffle plates as the combustion chamber only has a two dimensional variation. Typically results for the flow should be two dimensional, disregarding boundary effects, and thus independent of transverse location as demonstrated for configuration 2 and to a lesser degree configuration 6. This result changes with the progression of grids downstream as previously outlined, the extent of which is seen again in the LIF images, further supporting the turbulence generation arguments.

Below are selections of images from a range of configurations that demonstrate either the presence of detached flamelets or indeed auto-ignition. Figure 7.14 poses potential cases where a detached flamelet has been imaged, both show how a finger (shown in Figure 7.14) extends into unburnt fuel with concentrations of OH at the leading edge of the flame front. As indicated, the direction in which the flame front adjacent to the OH concentration is propagating is approximately in the direction of the circled point of interest. This suggest that the two regions of OH where indeed a single identity moments before the images was captured.
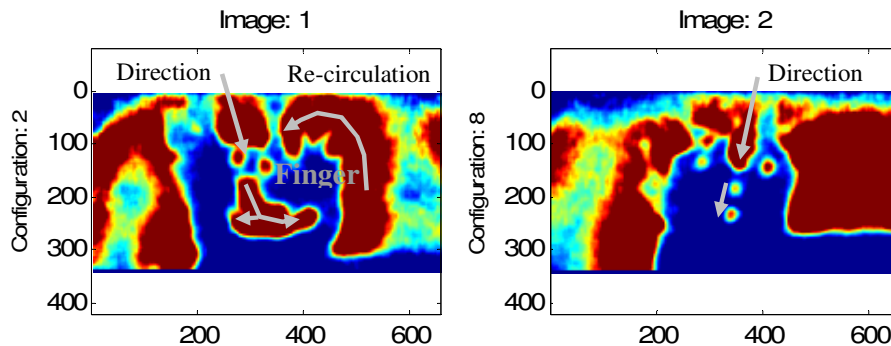

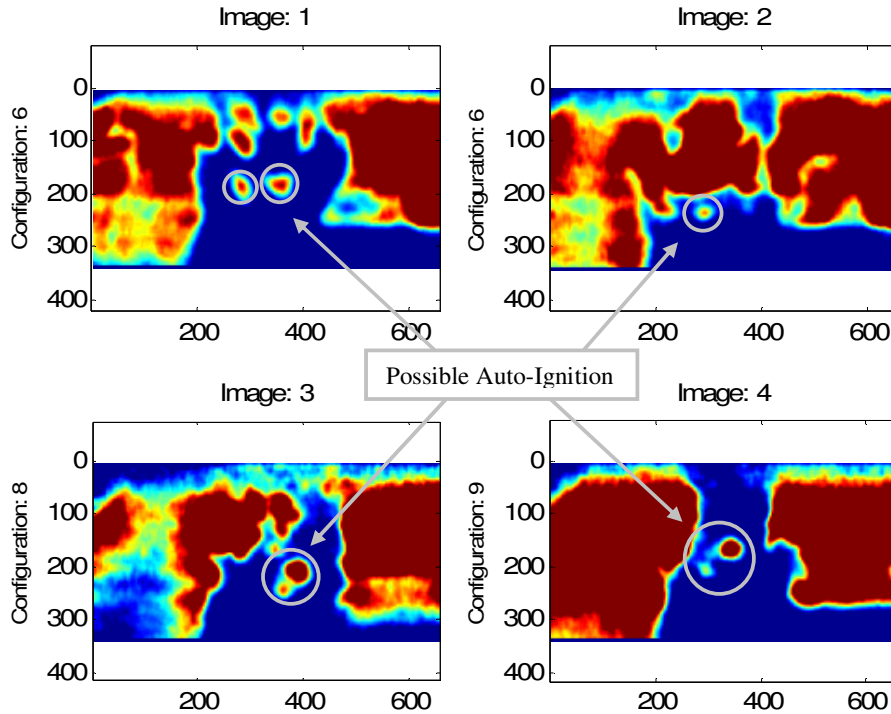Figure 7.14: Possible Examples of Detached Flamelets

Figure 7.15: Possible Examples of Auto-Ignition

Alternatively analysing similar OH concentrations under different circumstances, the possibility of auto-ignition is plausible. In the images above (Figure 7.15), the indicated regions of OH concentrations seems to possess no dominate flame front direction and in effect are developing reaction zones propagating spherically. In all cases the OH concentration appears to be independent for the main flow field and thus unlikely to be a result of three dimensional contortions. For auto-ignition to occur in a flow, temperatures must be able to pre-heat the fuel ahead or adjacent to the main flame front enough that the mixtures ignition temperature is reached. In the above cases, especially 1 and 4, the front departing the channel establishes a region of unburnt fuel bounded by an intense reaction zone thus pre-heating the re-circulation zone. Before the flame front begins to envelope the unburnt mixture caught behind the obstruction, pockets of reaction products are observed. Although this analysis is not conclusive, it does suggest that the properties and interactions of a transient deflagration in a premixed fuel is complex and surrounded by uncertainty.

7.4 FLOW FIELD INTERACTIONS

Compiling all three forms of data provides a unique insight into the interactions occurring between flow field properties. By considering the flame front location at significant positions on both the velocity and pressure graphs, influential parameters can be seen to either be dependent or independent variables. Initial examination of configuration 2, Figure 7.16, reveals that not only does the point of peak pressure correspond with that of peak velocity, but is also coincides with the combustion of the fuel caught behind the obstruction. The relatively large surface area of the flame front at this point means that the reaction rate is significantly higher as it consumes the fuel on several fronts. It can then be concluded that the peak values occur as the flame front enter and consumes the re-circulation zone most likely as a result of the increased rate of reaction. In addition to this, the smooth acceleration through the channel and relatively low velocities and RMS combine with the low degree of flame front wrinkling observed in the images. Again this confirms the conjecture that the grid placement is the essential factor governing the development of intense turbulence.
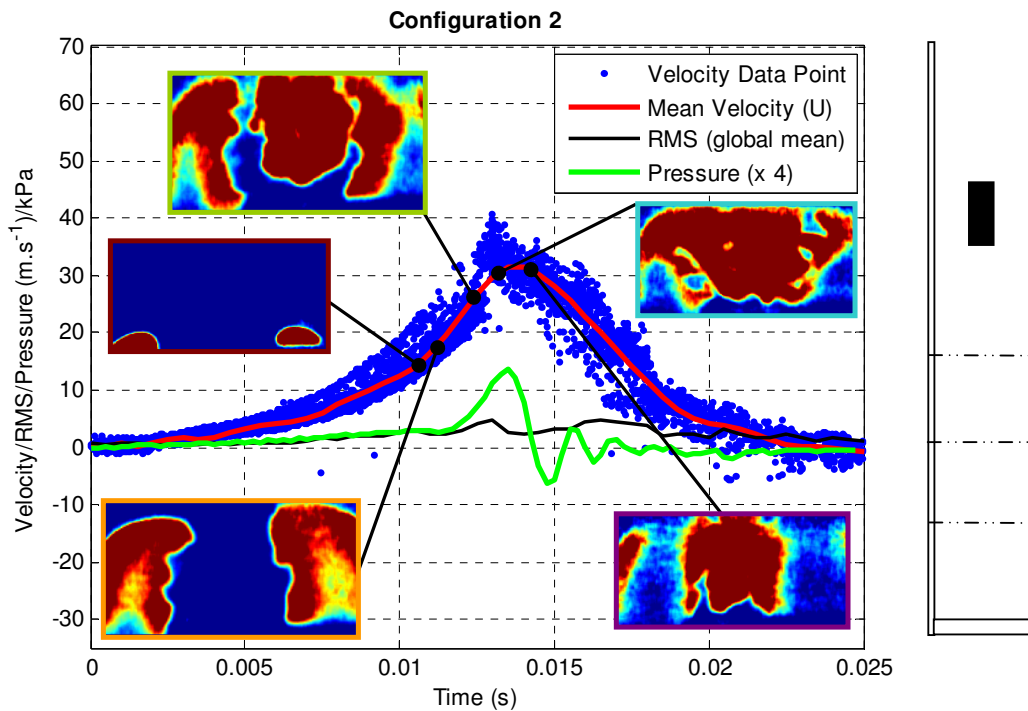

Figure 7.16: Flow Field Interactions; Configuration 2

Now considering the remaining dual grid configurations (Figures 7.17 through 7.19) in relation to the above control, several significant flow field modifications have occurred. Firstly note how the mean pressure profile has multiple local maximums with any subsequent pressure oscillations exhibiting the high gradient rise to peak as well as this inflection points after the peak value are common. In terms of timing, peak pressure is occurring in most cases before peak velocity, with the difference, specifically between configurations 2 and 7, equating to approximately 2 ms before hand. As the surface area of the flame front increases, so does the flame speed, but so to does the acceleration of the reaction rate and hence the advancing pressure graph. By looking at the LIF images for the turbulent configurations it is evident that as the first fingers propagate into the re-circulation zone, further expanding the integral length scale, the peak values are obtained.
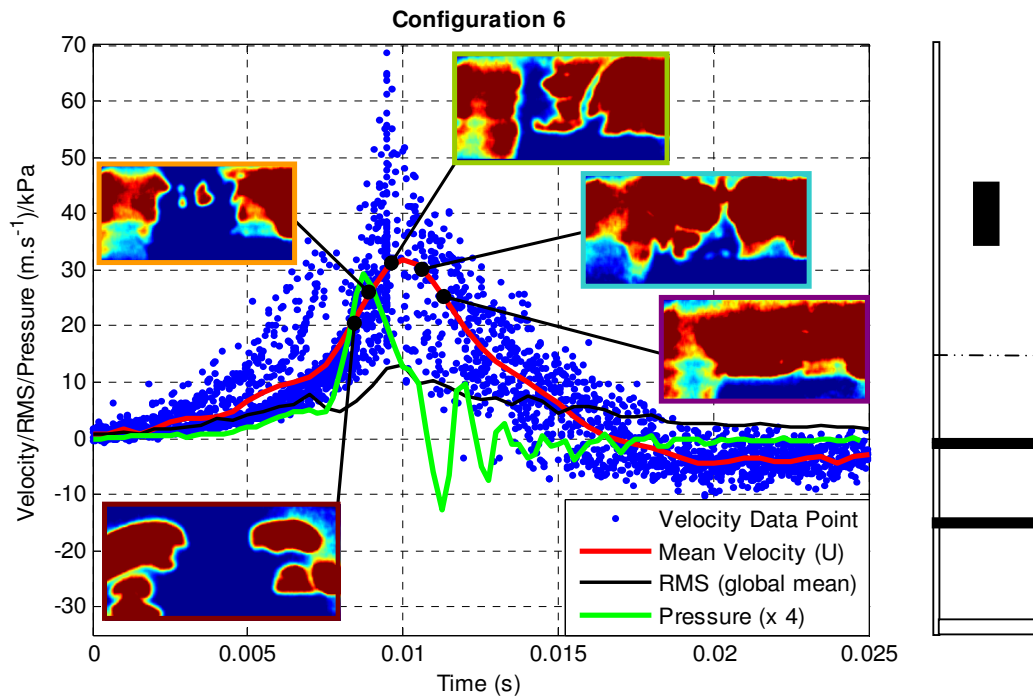

Figure 7.17: Flow Field Interactions; Configuration 6

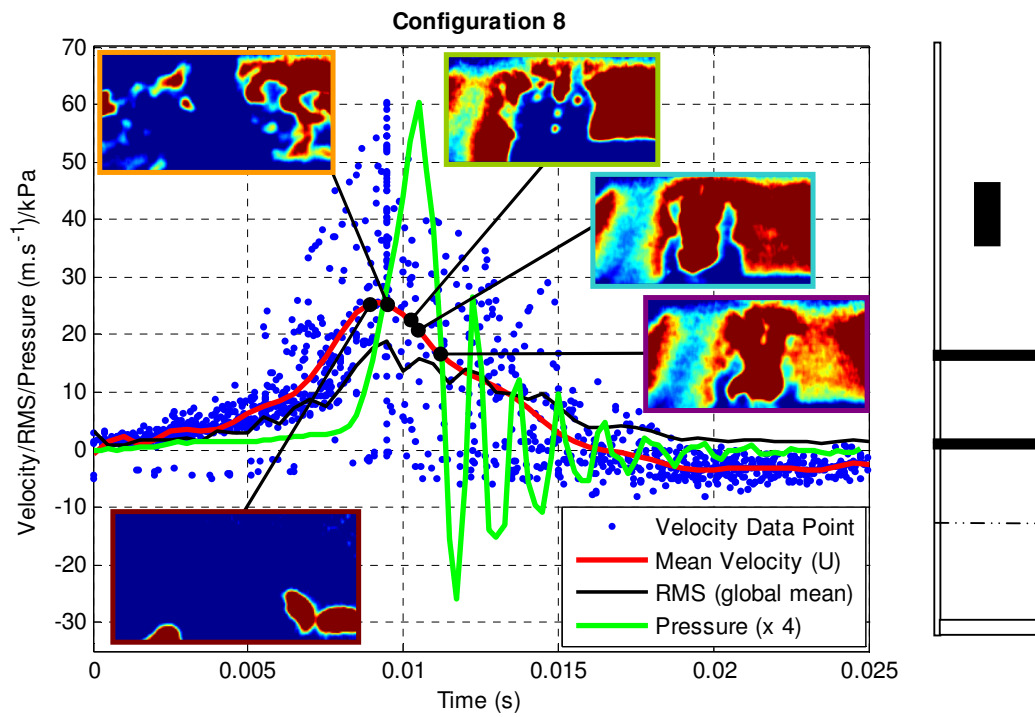Figure 7.18: Flow Field Interactions; Configuration 7

Figure 7.19: Flow Field Interactions; Configuration 8

8. CONCLUSION

This thesis has extended current knowledge in the field of turbulent premixed combustion. It has elucidated aspects of the interaction between solid surfaces and the flame front by applying advanced laser diagnostic methods to such transient processes. The following conclusions are deduced:-

1. The overpressure is not only affected by the obstacle blockage ratio but also by the number of obstacles and their location with respect to the ignition source.

2. Generally, overpressure increases as the distance of obstacle from the ignition source increases.

3. The speed of the reaction zone as a laminar flame front increases when the flow encounters a baffle plate.

4. Flame front structure, as given by the reaction zone imaged by using LIF-OH, is more distorted and patchy when the number of baffle plates and the distance from the ignition source is increased.

5. The correlation with turbulence is explored but this needs to be confirmed with further and more thorough measurements.

Expanding on the above, it has been conclusively proved that the significant factor influencing the pressure time traces of the flow is the location and number of the turbulence generating grids. In addendum to grid locality, the blockage ratio of the main square obstruction was also examined resulting in an additional degree of freedom that was able to show that by reducing the size of the channel for which the flow has to traverse and increase in peak pressure was observed. By considering a single grid relocating downstream from the ignition point towards the obstruction (as in family 1), peak pressure results convincingly demonstrate a positive trend. Correspondingly the results for dual grid relocation exhibit the same trend thus presenting the conclusion that by allowing the initial kernel to develop and gain speed, the grids influence on the flow dynamics is increased and turbulence intensity

in amplified. Comparing the peak overpressure results between the single and dual grid configurations highlights the possibility for the flame front to re-laminarise given time. This is consistent with the positive pressure trend suggesting that the upstream grid locations have a more influential role on peak values as the flow retains the disturbances at impact and progression through the channel. The results for three grid configurations however show that it is possible to disrupt the flow to the extent that reaction process may move on the regime diagram resulting in a reduction in peak values.

By introducing flame front imaging to the list of available data a further dimension was added to the analysis that further expanded the effectiveness of both the pressure and velocity time traces. The Laser-Induced Fluorescence imaging of the Hydroxyl radical was able to not only accurately provide insight into the integral length scale and degree and size of any flow field re-circulations but also indicate the flame fronts location at the point of peak pressure and velocity. Congregating the data to a common reference time enabled cross referencing and showed that in part the flame front was entering the re-circulation zone at the point of peak pressure. Closer examination of this emphasised the significance of overall reaction rate and integral length scale on peak overpressure. Consistently it was demonstrated that the mean velocity tended to not be as influenced by turbulence intensity as pressure was. As a result peak pressure not only increases positively in amplitude but also for the time taken to reach peak. From the LIF images this time to peak can be seen to correspond with the initial fingers of the flame front entering the re-circulating zone and forcing unburnt fuel into the fast moving flow exiting the channel.

Analysis of the LIF images alone was able to reaffirm the conjecture proposed from the pressure data that grid number and location were the most influential parameters on turbulence intensity. As the pressure values increased and thus turbulence, corresponding LIF images showed how the flame front wrinkling increased proportionally. In addition to this as the grids relocated towards the obstruction the number of eddies and the degree of three dimensional contortions increased, resulting in a high number of detached pockets of OH.

Finally by coupling this analysis for pressure, velocity and LIF with that of the RMS for the transverse component of velocity, a similar conclusion can be obtained. As velocity measurements where collected in the channel, where the flow follows the streamlines through the constriction, any deviation from this path must be attributed to the increase in turbulence intensity. Therefore as expected results for the transverse RMS further accentuate the connection between baffle plates and turbulence generation. The connection between peak pressure, RMS and qualitative results for flame front wrinkling and the integral length scale have been proven to interlink convincingly with degree of turbulence generation. By allowing the kernel to develop before interacting with obstructions and then maintaining the disturbance maximises the overpressure values which suggests heightened turbulence intensity.

The outstanding research issues arising from this thesis stem from the ability to be able to quantitatively analyse High Speed Laser-Induced Fluorescence. This will accurately be able to show the envelopment of re-circulation zone as the flame front curls around to consume the unburnt fuel caught behind the obstruction. Also by coupling sequential images, individual flamelet development can be tracked thus expanding the information available for phenomena such as, auto ignition and local extinction as well as reaction rates and local velocities. Final the ability to couple sequential LIF images with PIV and pressure will provide an invaluable data resource.

REFERENCES

[1] A. Alexiou, G. E. Andrews, and H. Phylaktou, "Side-vented gas explosions in a long vessel: the effect of vent position " *Journal of Loss Prevention in the Process Industries,* pp. 351-356, 1996.

[2] R. Starke and P. Roth, "An experimental investigation of flame behavior during cylindrical vessel explosions," *Combust. Flame,* pp. 249-259, 1986.

[3] J. E. Kent, A. R. Masri, S. H. Starner, and S.S.Ibrahim, "Wrinkling scales of turbulent premixed propagating flame fronts obtained from LIF-OH imaging," in *Conference on Laser Diagnostics in Fluid Mechanics and Combustion* Australia, 2005.

[4] R. C. Aldredge and V. Vaezi, "Premixed-flame propagation in turbulent Taylor-Couette flow," *Combustion and Flame,* vol. 115, pp. 293-301, 1998.

[5] R. J. M. Bastiaans, S. M. Martin, H. Pitsch, J. A. Van Oijen, and L. P. H. De Goey, "Flamelet analysis of turbulent combustion," Atlanta, GA, United States, 2005, pp. 64-71.

[6] L. P. H. de Goey, T. Plessing, R. T. E. Hermanns, and N. Peters, "Analysis of the flame thickness of turbulent flamelets in the thin reaction zones regime," *Proceedings of the Combustion Institute,* vol. 30, pp. 859-866, 2005.

[7] R. Hall, "Flow Field Measurement in Transient Premixed Flames," in *Aerospace, Mechanical and Mechatronic Engineering.* vol. Bachelor Engineering (Aero) Sydney: University of Sydney, 2006, p. 130.

[8] R. Hall, A. R. Masri, and S. H. Starner, "On the correlation between turbulence and peak overpressure in premixed flames propagating past solid obstacles," in *Australian Combustion Symposium* Sydney, 2007.

[9] D. Bradley, T. M. Cresswell, and J. S. Puttock, "Flame acceleration due to flame-induced instabilities in large-scale explosions," *Combust. Flame,* pp. 551-559, 2001.

[10] K. N. C. Bray, "The challenge of turbulent combustion," *Proc. Combust. Inst. ,* pp. 1-26, 1996.

[11] C. A. Catlin and R. P. Lindstedt, "Premixed turbulent burning velocities derived from mixing controlled reaction models with cold front quenching," *Combust. Flame,* pp. 427-439, 1991.

[12] S. S. Ibrahim and A. R. Masri, "The effects of obstructions on overpressure resulting from premixed flame deflagration," *Journal of Loss Prevention in the Process Industries,* vol. 14, pp. 213 - 221, 2001.

[13] A. R. Masri, S. S. Ibrahim, N.Nehzat, and A. R. Green, "Experimental study of premixed flame propagation over various solid obstructions," *Experimental Thermal and Fluid Science,* vol. 21, pp. 109-116, 2000.

[14] M. Fairweather, G. K. Hargrave, S. S. Ibrahim, and D. G. Walker, "Studies of premixed flame propagation in explosion tubes," *Combust. Flame,* pp. 504-518, 1999.

[15] J. E. Kent, A. R. Masri, and S. H. Starner, "A New Chamber to Study Premixed Flame Propagation Past Repeated Obstacles," in *5th Asia-Pacific Conference on Combustion* The University of Adelaide, Adelaide, Australia, 2005.

[16] A. R. Masri, S. S. Ibrahim, and B. J. cadwallader, "On the application of compressible LES in unsteady premixed combustion," in *Third Asia-Pacific Conference on Combustion* Seoul Korea, 2001.

[17] R. Starke and P. Roth, "An experimental investigation of flame behavior during explosions in cylindrical enclosures with obstacles," *Combust. Flame,* pp. 111-121, 1989.

[18] B. H. Hjertager, K. Fuhre, and M. Bjorkhaug, "Concentration effects on flame acceleration by obstacles in large-scale methane-air and propane-air vented explosions," *Combust. Sci. Technol.,* pp. 239-256, 1988.

[19] A. R. Masri, S. S. Ibrahim, N. Nezhat, and A. R. Green, *Exp. Thermal & Fluid Sci. Journal,* pp. 109-116, 2000.

[20] I. O. Moen, H. S. Lee, B. H. Hjertager, K. Fuhre, and R. K. Eckhoff, "Pressure development due to turbulent flame propagation in large-scale methane-air explosions," *Combust. Flame,* pp. 31-52, 1982.

[21] H. Phylaktou and G. E. Andrews, "The acceleration of flame propagation in a tube by an obstacle," *Combustion and Flame,* vol. 85, pp. 363-379, 1991.

[22] M. Fairweather, S. S. Ibrahim, H. Jaggers, and D. G. Walker, "Computational and experimental study of a forced, timevarying, axisymmetric, laminar diffusion flame," *Proc. Combust. Inst.,* pp. 365-371, 1996.

[23] I. O. Moen, M. Donato, R. Knystautas, and J. H. Lee, "Flame acceleration due to turbulence produced by obstacles," *Combust. Flame,* pp. 21-32, 1980.

[24] R. P. Lindstedt and V. Sakthitharan, "Time resolved velocity and turbulence measurements in turbulent gaseous explosions," *Combust. Flame,* vol. 114, pp. 469-483, 1998.

[25] S. N. D. H. Patel, S. Jarvis, S. S. Ibrahim, and G. K. Hargrave, "A temporal PIV study of flame/obstacle generated vortex interactions within a semi-confined combustion chamber," *Proc. Combust. Inst.,* pp. 1849-1854, 2002.

[26] D. R. Ballal, "An experimental study of flame turbulence," *Acta Astronautica,* vol. 5, pp. 1095-1112, 1978.

[27] R. W. Bilger, "Marker fields for turbulent premixed combustion," *Combustion and Flame,* vol. 138, pp. 188-194, 2004.

[28] R. Borghi, "Turbulent premixed combustion: Further discussions on the scales of fluctuations," *Combustion and Flame,* vol. 80, pp. 304-312, 1990.

[29] D. Bradley, M. Z. Haq, R. A. Hicks, T. Kitagawa, M. Lawes, C. G. W. Sheppard, and R. Woolley, "Turbulent burning velocity, burned gas distribution, and associated flame surface definition," *Combustion and Flame,* vol. 133, pp. 415-430, 2003.

[30] C. A. Catlin, M. Fairweather, and S. S. Ibraiim, "Predictions of turbulent, premixed flame propagation in explosion tubes," *Combustion and Flame,* vol. 102, pp. 115-128, 1995.

[31] M. D. Checkel and A. Thomas, "Turbulent combustion of premixed flames in closed vessels," *Combustion and Flame,* vol. 96, pp. 351-370, 1994.

[32] Y.-C. Chen and R. W. Bilger, "Experimental inverstigation of three-dimensional flame-front structure in premixed turbulent combustion II. Lean hydrogen /air bunsen flames," *Combustion and Flame,* pp. 155-174, 2004.

[33] P. Clavin and F. A. Williams, "Theory of premixed-flame propagation in large-scale turbulence," *Journal of Fluid Mechanics,* vol. 589-604 1979.

[34] E. P. Hassel and S. Linow, "Laser diagnostics for studies of turbulent combustion," *Meas. Sci. Technol.,* vol. 11, 2000.

[35]   B. H. Hjertager, "Influence of turbulence on gas explosions," *Journal of Hazardous Materials,* pp. 315-346, 1984.

[36]   M. Z. Kamardin, "Premixed flame propagation past solid obstacles," in *Aerospace, Mechanical and Mechatronic Engineering.* vol. Bachelor Sydney: University of Sydney, 2005, p. 185.

[37]   A. R. Masri, S. S. Ibrahim, and B. J. Cadwallader, "Measurements and large eddy simulation of propagating premixed flames," *Experimental Thermal and Fluid Science,* vol. 30, pp. 687 - 702, 2006.

[38]   A. Palm-Leis and R. A. Strehlow, "On the propagation of turbulent flames," *Combustion and Flame,* vol. 13, pp. 111-129, 1969.

[39]   A. Palm-Leis and R. A. Strehlow, "On the propagation of turbulent flames," *Combustion and Flame,* vol. 47, 1982.

[40]   N. Peters and P. Luc Vervisch, "Turbulent combustion," *Combustion and Flame,* vol. 125, pp. 1222-1223, 2001.

[41]   H. N. Phylaktou, "Gas explosion in long closed vessels with obstacles: a turbulent combustion study applicable to industrial explosions," in *Mechanical Engineering.* vol. Ph.D. Leeds: The University of Leeds, 1993.

[42]   G. Pilla, D. Galley, D. A. Lacoste, F. Lacas, D. Veynante, and C. O. Laux, "Stabilization of a turbulent premixed flame using a nanosecond repetitively pulsed plasma," *Plasma Science, IEEE Transactions on,* vol. 34, pp. 2471-2477, 2006.

[43]   S. S. Shy, S. I. Yang, W. J. Lin, and R. C. Su, "Turbulent burning velocities of premixed CH4/diluent/air flames in intense isotropic turbulence with consideration of radiation losses," *Combustion and Flame,* vol. 143, pp. 106-118, 2005.

[44]   S. R. Turns, *An introduction to combustion*, 2 ed., 2000.

[45]   D. Y. Lai, V. T. Paka, D. P. Delisi, A. V. Arjannikov, and S. A. Khanaev, "An intercomparison study using 3-dimensional electromagnet turbulent velocity probes, a hot-film anemometer, and an airfoil probe," 1999, pp. 174-178.

[46]   S. S. Shy, C. Y. Tang, and S. Y. Fann, "A nearly isotropic turbulence generated by a pair of vibrating grids," *Experimental Thermal and Fluid Science,* vol. 14, pp. 251-262, 1997.

[47]   R. Z. Atobiloye and R. E. Britter, "On flame propagation along vortex tubes," *Combustion and Flame,* vol. 98, pp. 220-230, 1994.

[48]   B. J. Cadwallader, Y.-C. Chen, and A. R. Masri, "PIV and other measurements in unsteady premixed flames," in *Aerospace, Mechanical and Mechatronic Engineering* Sydney: University of Sydney, 2001.

[49]   T. C. Chew, "Aspects of premixed turbulent combustion," in *Chemical Engineering.* vol. Ph.D. Cambridge: Cambridge University, 1988.

[50]   S. A. Filatyev, J. F. Driscoll, C. D. Carter, and J. M. Donbar, "Measuring properties of turbulent premixed flames for model assessment, including burning velocities, stretch rates, and surface densities," *Combustion and Flame,* pp. 415-430, 2005.

[51]   D. W. Guillaume and J. C. LaRue, "The effect of multi-plate array scapingon grid-generated turbulence," *Fluid Structures,* pp. 485-490, 2003.

[52]   M. Z. Haq, C. G. W. Sheppard, R. Woolley, D. A. Greenhalgh, and R. D. Lockett, "Wrinkling and curvature of laminar and turbulent premixed flames," *Combustion and Flame,* pp. 1-15, 2002.

[53]   M. Hermanns, M. Vera, and A. Linan, "On the dynamics of flame edges in diffusion-flame/vortex interactions," *Combustion and Flame,* vol. In Press, Corrected Proof.

[54]   S. Kadowaki, S. H. Kim, and H. Pitsch, "The dynamics of premixed flames propagating in non-uniform velocity fields: Assessment of the significance of intrinsic instabilities in turbulent combustion," in *Annual Research Briefs 2005* Centre for Turbulence Research 2005.

[55]   C. Kortischik, T. Plessing, and N. Peters, "Laser optical investigation of turbulent transport of temperature ahead of the preheat zone in a premixed flame," *Combustion and Flame,* pp. 43-50, 2004.

[56]   C. J. Lawn and R. W. Schefer, "Scaling of premixed turbulent flames in the corrugated regime," *Combustion and Flame,* vol. 146, pp. 180-199, 2006.

[57]   N. Pasquier, B. Lecordier, M. Trinite, and A. Cessou, "An experimental investigation of flame propagation through a turbulent stratified mixture," *Proceedings of the Combustion Institute,* vol. 31, pp. 1567-1574, 2007.

[58]   V. R. Savarianandam and C. J. Lawn, "Burning velocity of premixed turbulent flames in the weakly wrinkled regime," *Combustion and Flame,* vol. 146, pp. 1-18, 2006.

[59]   F. A. Williams and J. Furukawa, "Approximate local mathematical descriptions of turbulent Bunsen flames in the flamelet regime," *Combustion and Flame,* vol. 138, pp. 108-113, 2004.

[60]   R. P. Linstedt and V. Sakthitharan, "Time resolved velocity and turbulence measurements in turbulent gaseous explosions," *Combustion and Flame,* vol. 114, pp. 469-483, 1998.

[61]   D. J. Parka, A. R. Greena, Y. S. Leeb, and Y.-C. Chenc, "Experimental studies on interactions between a freely propagating flame and single obstructions in a rectangular confinement," *Combustion and Flame,* vol. 150, pp. 27-39, 2007.

[62]   A. Soika, F. Dinkelacker, and A. Leipertz, "Pressure influence on the flame front curvature of turbulent premixed flames: comparison between experiment and theory," *Combustion and Flame,* vol. 132, pp. 451-462, 2003.

[63]   D. A. Knaus, S. S. Sattler, and F. C. Gouldin, "Three-dimensional temperature gradients in premixed turbulent flamelets via crossed-plane Rayleigh imaging," *Combustion and Flame,* vol. 141, pp. 253-270, 2005.

[64]   G. W. Koroll, R. K. Kumar, and E. M. Bowles, "Burning velocities of hydrogen-air mixtures," *Combustion and Flame,* vol. 94, pp. 330-340, 1993.

[65]   N. Chigier, "Combustion measurement," H. Publishing, Ed.: Hemisphere Publishing Corporation, 1991.

[66]   G. J. Smallwood, O. L. Gulder, D. R. Snelling, B. M. Deschamps, and I. Gokalp, "Characterization of flame front surfaces in turbulent premixed methane/Air combustion," *Combustion and Flame,* vol. 101, pp. 461-470, 1995.

[67]   Y.-C. Chen and R. W. Bilger, "Experimental investigation of three-dimensional flame-front structure in premixed turbulent combustion--I: hydrocarbon/air bunsen flames," *Combustion and Flame,* vol. 131, pp. 400-435, 2002.

[68]   O. L. Gulder and G. J. Smallwood, "Flame surface densities in premixed combustion at medium to high turbulence intensities," *Combustion Science and Technology,* vol. 179, pp. 191-206, 2007.

[69] Z. Hansheng, Y. Fang-Yu, J. P. Singh, R. L. Cook, and G. W. Loge, "Laser-induced breakdown spectroscopy in a metal-seeded flame," 2000, pp. 595-600 vol.1.

[70] K. Yamamoto, S. Inoue, H. Yamashita, D. Shimokuri, S. Ishizuka, and Y. Onuma, "PIV measurement and turbulence scale in turbulent combustion," *Heat Transfer - Asian Research,* vol. 35, pp. 501-512, 2006.

[71] P. R. Medwell, P. A. M. Kalt, and B. B. Dally, "Simultaneous imaging of OH, formaldehyde, and temperature of turbulent nonpremixed jet flames in a heated and diluted coflow," *Combustion and Flame,* vol. 148, pp. 48-61, 2007.

[72] J. S. Fox and P. M. Danehy, "Validation of a laser-induced fluorescence (LIF) model for mole-fraction imaging," 1999, pp. 159-160 vol.2.

[73] e. E. Fundamentals, "Hot-wire anemometers: Introduction."

[74] "Laser-induced fluorescence." vol. 2007: Wikimedia Foundation, Inc, 2007.

[75] J. W. Daily, "Laser induced fluorescence spectroscopy in flames," 2000.

[76] K. W. Jenkins, M. Klein, N. Chakraborty, and R. S. Cant, "Effects of strain rate and curvature on the propagation of a spherical flame kernel in the thin-reaction-zones regime," *Combustion and Flame,* vol. 145, pp. 415-434, 2006.

[77] A. R. Choudhuri and S. R. Gollahalli, "A numerical study of the structure of methane-hydrogen blended fuel turbulent jet flames," 2002, pp. 422-429.

[78] A. Mura and R. Borghi, "Towards an extended scalar dissipation equation for turbulent premixed combustion," *Combustion and Flame,* vol. 133, pp. 193-196, 2003.

[79] Spectra-Physics, *Quantra-Ray PDL-3 pulsed dye laser instruction manual* vol. Rev. A: Laser Products Division, 1989.

[80] Efunda, "Laser Doppler Velocimeter: Introduction." vol. 2007, 2007.

[81] N. Chigier, *Combustion measurement*: Hemisphere Publishing Corporation, 1991.

APPENDIX A: COMPUTER MACROS

A.1 MACRO CODE FOR LIF EXPERIMENTAL OPERATION

Sequential Commands	Action
out 0	Initial condition
pvc 1	Loads camera data file
imac 0	Inhibit all other computer process
del 545	Allow time for the chamber to fill with the premixed air/fuel
sync 0	Connect to the Camera
del 15	final fill
out 1	Turns off fuel and redirects is to the exhaust
del 45	Delay for mixture to settle in chamber
out 9	Opens flap
del 40	Delay for flap to open
pvcsc	Opens camera shutter
del 2	Delay for ~0.033 seconds to make sure the shutter is open
out 13	Trigger the delay generator; Initiates ignition sequence and LIF Pulse
del 5	Delay for experiment to run
out 9	Flushes chamber
Pvcre	Closes camera shutter
e	Erases any previous image file
d	Displays the current image file
out 1	Closes flap returns to default state
sync 1	Disconnects from the Camera
imac 1	Enable normal computer operations
sa config5_%	Saves data file under "config5_(run number)"

Table A.1: Macro Code

A.2 MACRO CODE FOR LDV EXPERIMENTAL OPERATION

Sequential Commands	Action
imac 0	Inhibit all other computer process
out 16	Fill chamber with air/fuel, inhibit LDV
del 1500	Delay for 25 seconds
out 17	Direct air/fuel through seeding, drains still closed, LDV inhibit still on
del 180	Delay for 3 seconds
out 19	Turn off seeding by opening drain valve (2), seeding valves still set to seed (high pressure check valve prevents seed from flowing)
del 120	Delay 2 seconds for air/fuel mixture to settle
out 26	Keeps drains open and opens flap
del 60	Delay 1 second to allow flap to open
out 10	Enable LDV
out 14	Enable ignition pulse
del 30	Delay ½ second to collect flow data
out 19	Inhibit LDV, close flap and keep drains open (default state)
del 120	Delay 2 seconds to allow flame residue to evacuate
imac 1	Enable normal computer operations

Table A.2: Macro Code

APPENDIX B: SENSOR SPECIFICATIONS

B.1 PRESSURE CALIBRATION

To calibrate the pressure sensor a simple flow system was constructed to deliver a constant pressure to both transducers. The system integrated a pressure dump so atmospheric conditions could be restored between each sequential realisation.
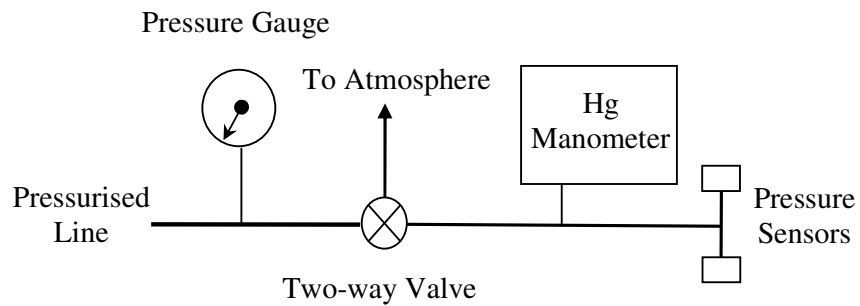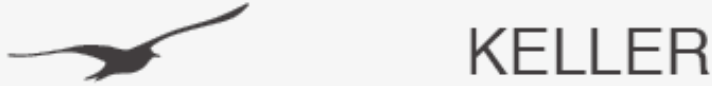

Figure B.1: Pressure Calibration Layout

B.2 PRESSURE SENSOR SPECIFICATIONS[1]
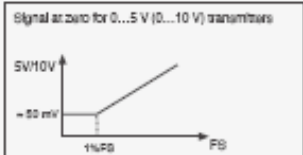
KELLER

SPECIFICATIONS

SERIES 21 R / 21 SR / 21 MR

PR 21 R/SR/MR[1]	0,5	1	2	5	10	16	bar	vented gauge						
PAA 21 R/SR/MR		1	2	5	10	16	bar	absolute						
PA 21 R/SR/MR[2]		1	2	5	10	16	30	50	100	160	200	400	600	bar sealed gauge
Over Range	2	3	4	10	20	25	50	75	150	250	300	500	700	bar

[1] mPm connector only, not cable
[2] Zero at 1000 mbar abs.

Signal Output	4...20 mA	0...5 Vdc	1...6 Vdc	0...10 Vdc	0...100 mV
Supply Voltage		8...28 Vdc		13...30 Vdc	6...28 Vdc · 10 Vdc
Current required	max. 25 mA	4 mA max.			2 mA max.
Zero/Span Tolerance	0,5% FS	0,5% FS [*]	0,5% FS	0,5% FS [*]	± 0,1% FS
Configuration	2 wire	3 wire			4 wire
Electrical Connection:	OUT/GND: Pin 1 / White	GND: Pin 1 / Green			GND: Pin 1 / White
mPm 193 or		+OUT: Pin 2 / White			+OUT: Pin 2 / Red
cable 2 m, 4 core	+Vcc: Pin 3 / Brown	+Vcc: Pin 3 / Brown			+Vcc: Pin 3 / Black
					-OUT: Pin 4 / Blue
Linearity	± 0,2% typ. / ± 0,5% max.				
Total Error Band [x] +18...+22 °C	± 0,5% typ. / ± 1% max.				
Total Error Band [x] 0...+50 °C	± 1,0% typ. / ± 2% max.				
Total Error Band [x] -20...+80 °C	± 2,5% typ. / ± 4% max.				

[x] Total error band includes linearity, hysteresis, repeatability, zero/span offsets and temperature effects.

[*] Signal at zero ≈ 50 mV --> see chart

Signal at zero for 0...5 V (0...10 V) transmitters

Operating Temperature	-20...+80 °C (on demand -40...100 °C)
Pressure Port	G 1/4" male
Pressure Media	Compatible with 316L stainless steel
Weight	≈ 75 g
Electromagnetic Compatibility	CE marked: Fully tested to EN 50081-2 and EN 50082-2
Enclosure Protection	IP 65
Insulation	> 100 MΩ / 500 Vdc
Vibration	20 g (5...2000 Hz, max. amplitude ± 3 mm), according to IEC 68-2-6
Shock	20 g (11 ms)

User Notes: Basic 100 mV transmitters are calibrated at 10 Vdc to produce 0...100 mV signal (nominal), and require a stable voltage supply. They can be operated at 5 Vdc to give 0...50 mV signal or 20 Vdc to give 0...200 mV signal. The circuit is a compensated resistance bridge and is completely passive with no diodes or reactive components. Bridge resistance is 3,5 kΩ nominal.

The 6...28 V supply transmitter is fitted with an internal regulator. The mPm connector has a PG7 cable gland entry suitable for cables between 4 and 6 mm diameter. Screw terminals and solder lugs are provided. The G 1/4 pressure connection has an integral Viton® seal at the shoulder. Alternatively it may be sealed using a face seal on the flat nose of the pressure port.

---

[1] Keller –Druckmesstechnik Type: PR-21S/1 bar/80549.3 www.keller-druck.com

APPENDIX C: DYE TUNING EFFICIENCIES AND RHODAMINE 590 PROPERTIES[2]

Curves show typical performance when the PDL-3 is pumped by a
Quanta-Ray GCR-3.

---
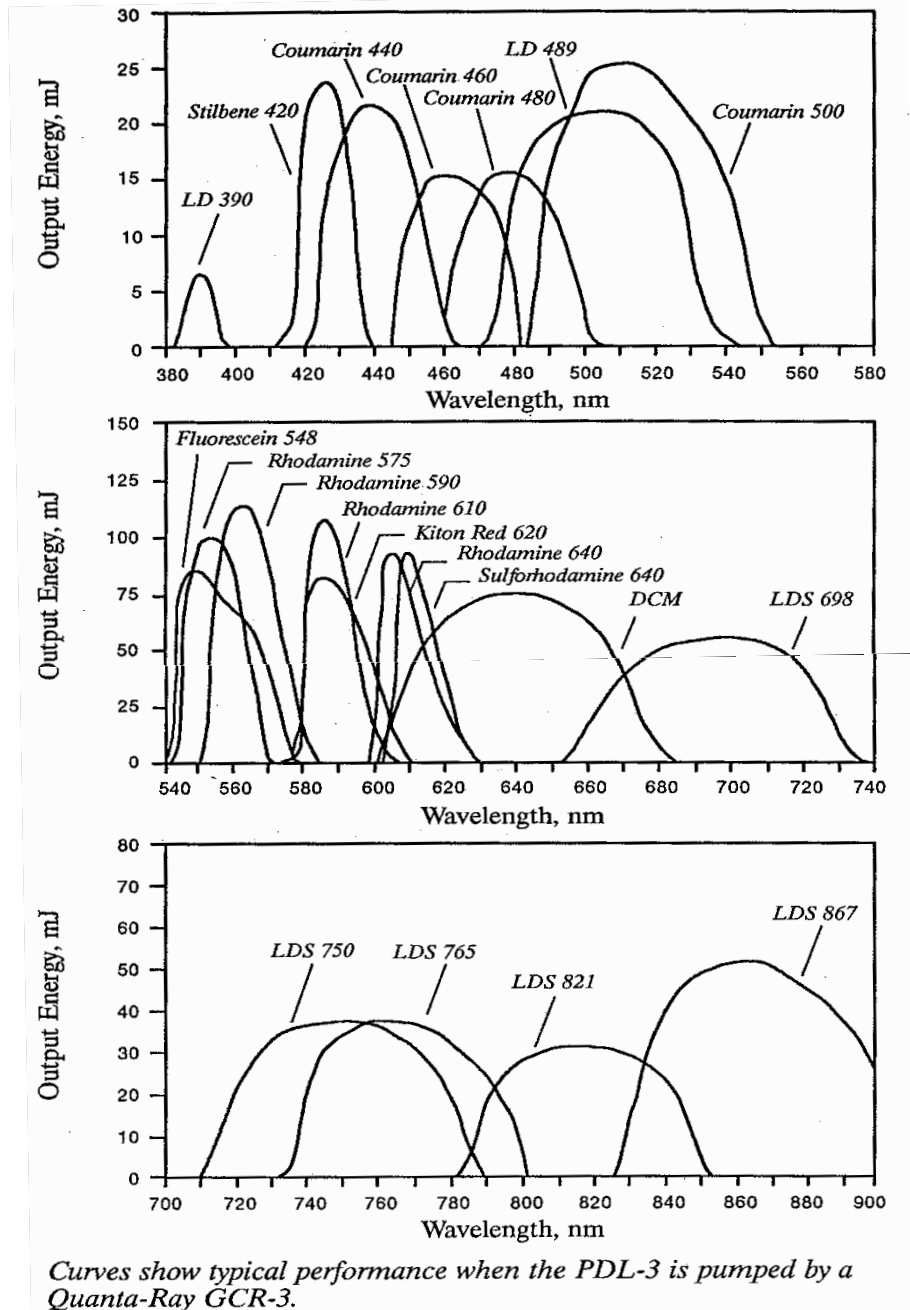
[2] Spectra-Physics, *Quantra-Ray PDL-3 pulsed dye laser instruction manual* vol. Rev. A: Laser Products Division, 1989

Rhodamine 590

•

Dye Mixture

S-P Part Number:	1609-0010
Manufacturer:	Exciton
Molecular Weight:	530.38
Concentration:	115 mg/l (oscillator)
	17 mg/l (amplifier)
Solvent:	Methanol

Configuration

Delay Line:	None
Preamplifier:	No
Amplifier:	Longitudinally Pumped

Performance

Pump Wavelength:	532 nm
Pump Energy:	360 mJ and 500 mJ
Peak Wavelength:	560 nm DCR 4 C(10)
Peak Conversion Efficiency:	28%
Tuning Range:	553 to 577 nm
A.S.E. Near Peak:	0.2%

Comments

1. Rhodamine 590 is a very stable, high gain dye.
2. Dye halflife is > 300 hr @ 10 pps.
3. Use tetrafluoroborate (BF$_4$) rhodamine 590.

132 mg in 1148 ml methanol

⇒ M = 0.115
take 1·l ⇒ oscillator
the rest 148 ml is diluted
by methanol to
1 liter

Output Energy, mJ vs Wavelength, nm. Curves labeled DCR-4D and DCR-3G.

APPENDIX D: INTENSIFIER[3]

Each accelerated photoelectron causes the emission of hundreds more from the MCP. The electrons maintain the conformation of the incident photons.

The secondary electrons are accelerated just sufficiently to excite the phosphor screen.

D.C. 5000V

D.C. 300V

Low intensity light from dark environment

(Not shown tilted)

High intensity image formed

Very thin layer of gallium arsenide photocathode releases 1 electron per photon.

Low energy photoelectrons are accelerated to a high enough energy to cause a secondary emission cascade.

Many more photons are emitted at the phosphor due to the immense number of incident electrons.

---

[3] http://en.wikipedia.org/wiki/Image_intensifier;"Image Intensifier": Wikimedia Foundation, cited 31/10/2007.

APPENDIX E: LDV PARTICULATE MATERIAL OPTIMISATION

For the LDV system to obtain velocity measurements, the flow has to contain suspended particulate material to reflect the light. As the time scale for the experiment is of the order of 20ms the seeding rate and number of valid velocity counts per run is important in maintaining the accuracy of the results. A range of variations to the experimental procedure were examined to derive a maximum seeding combination. The assessed areas include:-

1. Time allowed for seed to enter the chamber
2. Time allow for the seed to settle before ignition
3. Mass flow rate of the fuel air mixture entering the chamber

All three parameters were tested by running the experiment without firing the ignition laser in order to obtain static velocity results and validation levels.

E.1 SEEDING DURATION

By altering the time allowed for chamber seeding to occur, the total amount of particulate material entering the experiment is varied. A range from 0.5 seconds to 6 seconds was examined with the results show in Figure E.1) below.
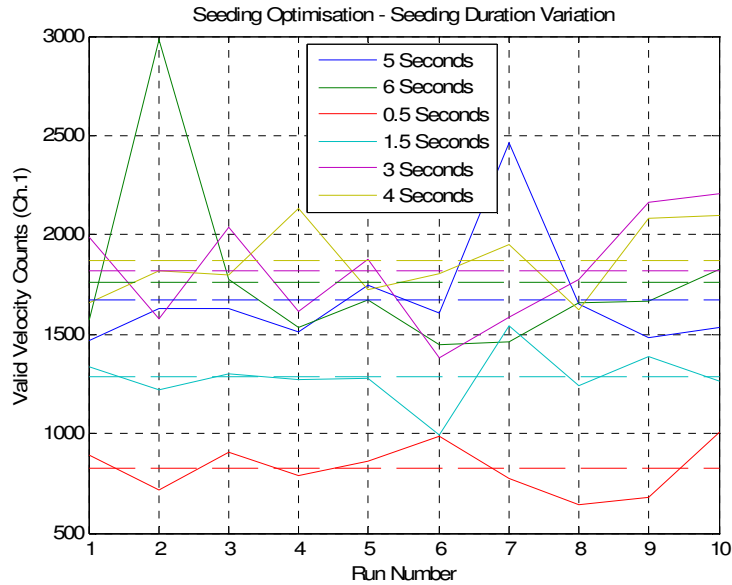
Figure E.1: Seeding Duration Variation

These results show that an increase in seeding duration corresponds to an increased validation rate. The results were acquired over two days with each configuration duplicated for accuracy and repeatability data. Specifically the results outlined the optimum time for seeding is between 3 and 4 seconds.

E.2 SETTLING TIME

Settling time refers to the time interval between the seeding cut off and the ignition laser firing. In this case extending the duration the seed is allocated to settle in the flow allows the particulate material to suspend motionless in the chamber. The graph below (Figure E.2) outlines how the effect of settling time on validation rate is more influential than seeding duration. Examining the data average lines (shown dashed) it can be seen that the increase in settling time corresponds to an increase in valid measurements. The increase continues up to 8 seconds when at 10 seconds the seed begins to collect and settle on the baffle plates reducing the validation rate.
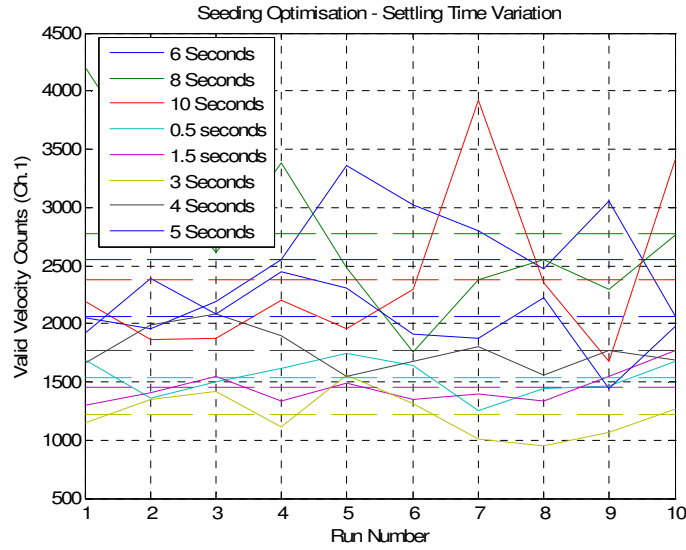
Figure E.2: Settling Time Variation

The consistency of the results obtain for the optimisation were also clarified with all configurations tested twice and over-plotted. Figure E.3) shows a graph of the averages for 3-5 seconds settling time for both runs, under identical conditions. Experimentally the results show a maximum average variation of 500 data points occurring with a three second settling time. Considering the deviation from the average exceeds 1000 data points in some cases, the results are within an expectable level of experimental error.
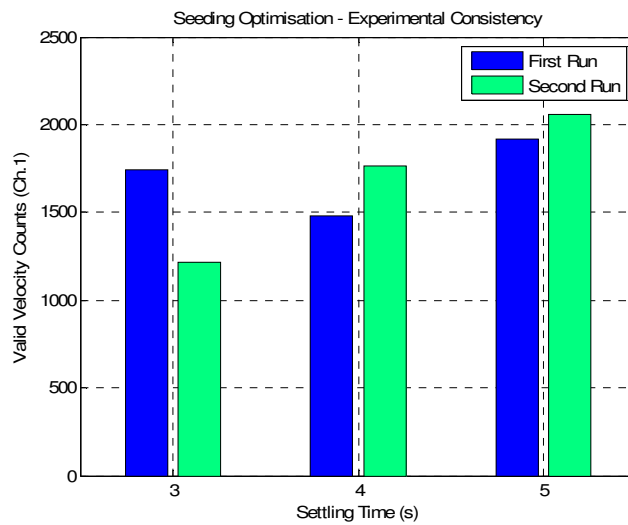
Figure E.3: Experimental Error Validation

E.3 MASS FLOW RATE

The final parameter examined in the seeding optimisation was the mass flow rate which dictates the velocity as well as particulate material entering the chamber over a given time interval. These results reproduced in Figure E.4 show how the mass flow rate has a significant influence on the validation rate. Clearly an increase in mass flow rate has major consequences on the overall data validity; however it produces a wider spread of results.
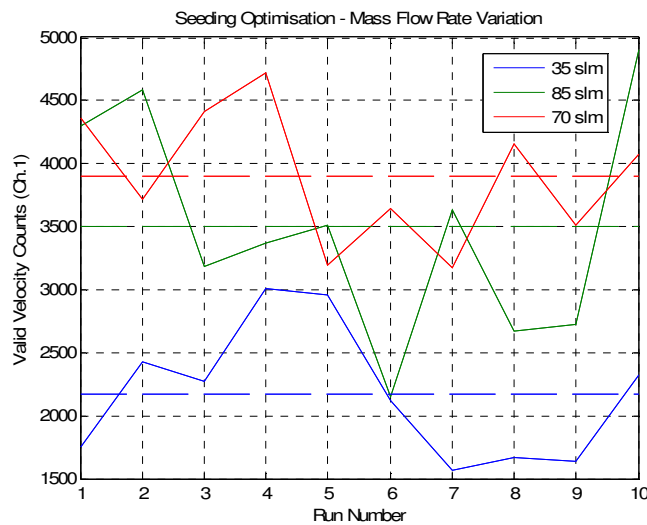
Figure E.4: Mass Flow Rate Variation

Seeding optimisation was concluded to have a significant bearing on the number of valid data points collected during each experiment. This in turn directly affects the accuracy of the results by reducing the experimental error which ultimately improves the turbulent results. From the data above the optimal seeding configuration is shown below in Table E.1. The final configuration also considers the practical nature of the experiment and hence the settling time is caped so as not to unnecessarily increase the total run time.

Seeding Duration (s)	3
Settling Time (s)	3
Mass Flow Rate (SLPH)	80

Table E.1: Optimal Seeding Configuration

E.4 LDV PERFORMANCE QUALIFICATION

Over the duration of the experiment it was found that several aspects of the LDV system where significantly more critical than seeding optimisation. Although adequate seed was required to obtain high validation rates, fine tuning the LDV receiver and the Argon Laser had a greater effect. By introducing excessive amounts of particulate material into the chamber it was possible to saturate the system without a substantial increase in the number of data points per millisecond. Further to this it was observed that the burst efficiency of the system was susceptible to fluctuations resulting in efficiencies of 1 to 2 percent. This means that given a bin of collected data only 1 to 2 percent was being converted into validated results, while the rest was not being processed hence reducing the validation rate.

E.4.1 Argon Laser Power Output

Poor burst efficiency was discovered to be a result of inadequate power output of the Argon Laser resulting in a weaker beam intersection and interference pattern. Although the power of the laser can be altered directly by increasing the current on the main control unit, the efficiency and effectiveness of the output wattage was a result of the internal optical alignment. Figure E.5 below shows a diagram of the internal optical layout of a typical Argon Laser, with the output coupling lens (right), being one of the adjustable parameters. The centre of curvature has a finite location for which to be focused in order to achieve maximum power to output efficiency. By adjusting the centre of curvature in the Cartesian plane the beam can be directed located to maximise available power.
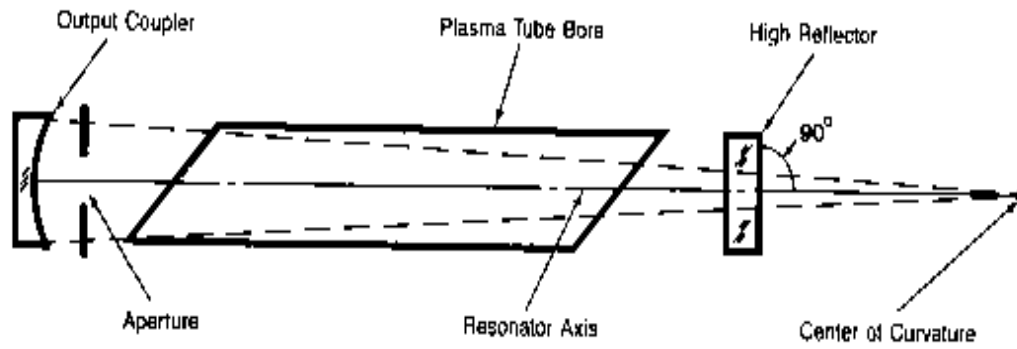
Figure E.5: Argon Laser Optics [33]

E.4.2 Laser Focus

Accurate focusing of the LDV receiver is crucial in obtaining high validation rates as well as a high signal to nose ratio. As outlined in section 3.1.2 above the focal point of the two laser beams must be situated with in the limits of the 150 nm viewing slit in the optical receiver for data collection. Collecting the data is achieved with three sensors that are all focused on the single location and consequently if one of the sensor's is impeded the validation rate is reduced significantly

APPENDIX F: POLYNOMIAL ORDER ANALYSIS

It was found that the order of the polynomial used to smooth the mean velocity profile and to approximate or filter individual realisations, significantly varied the RMS results. For this reason several values were tried in order to establish the most stable and best fitting profile approximation.

A polynomial of order 10 was found not to give the curve enough degrees of freedom to fit the complex curve as the kernel develops. However this particular curve is stable and follows the data as the flame egresses from the chamber well. For order 30 (shown Figure F.3), the instabilities of such a high order polynomial are obvious. As a results a very unstable RMS profile is calculated that has now experimental proof. Finally a polynomial of order 20 was tested (Figure F.2) and found to fit the curves of the velocity profile satisfactorily. The instabilities dominating the profile in Figure F.3) are not longer effecting the approximation whilst the error in the kernel development data, as in Figure F.1, has been significantly reduced.
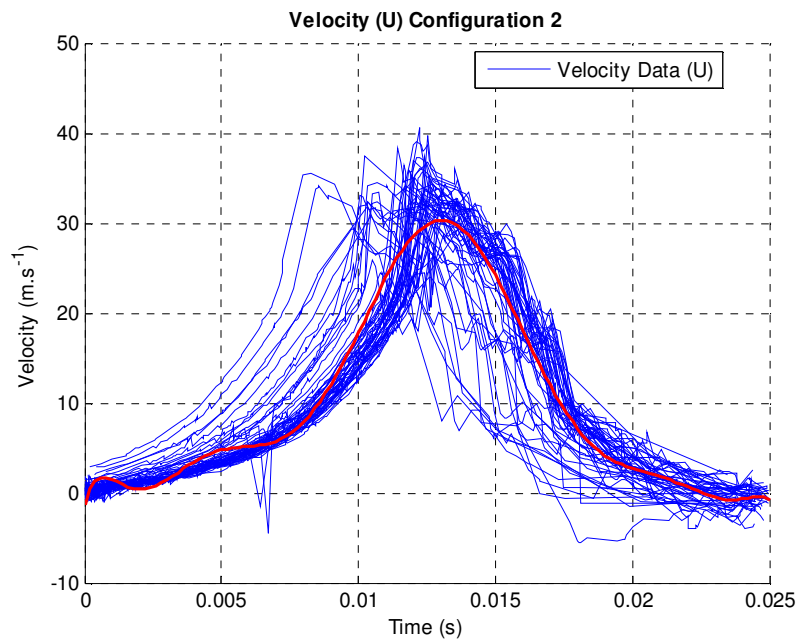
Figure F.1: Polynomial Order 10
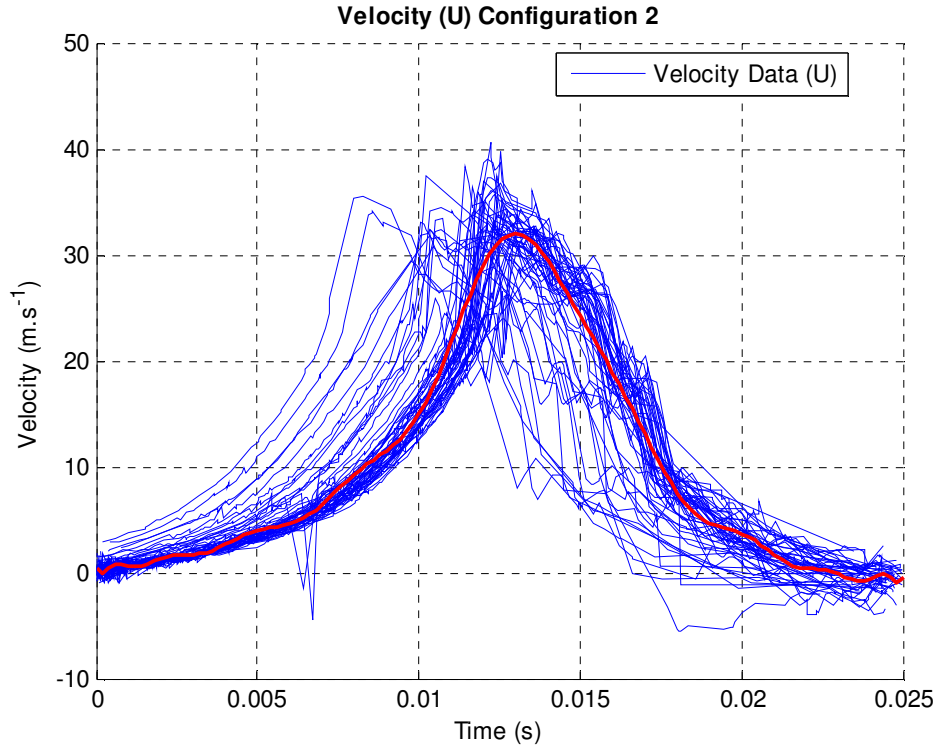
Figure F.2: Polynomial Order 20
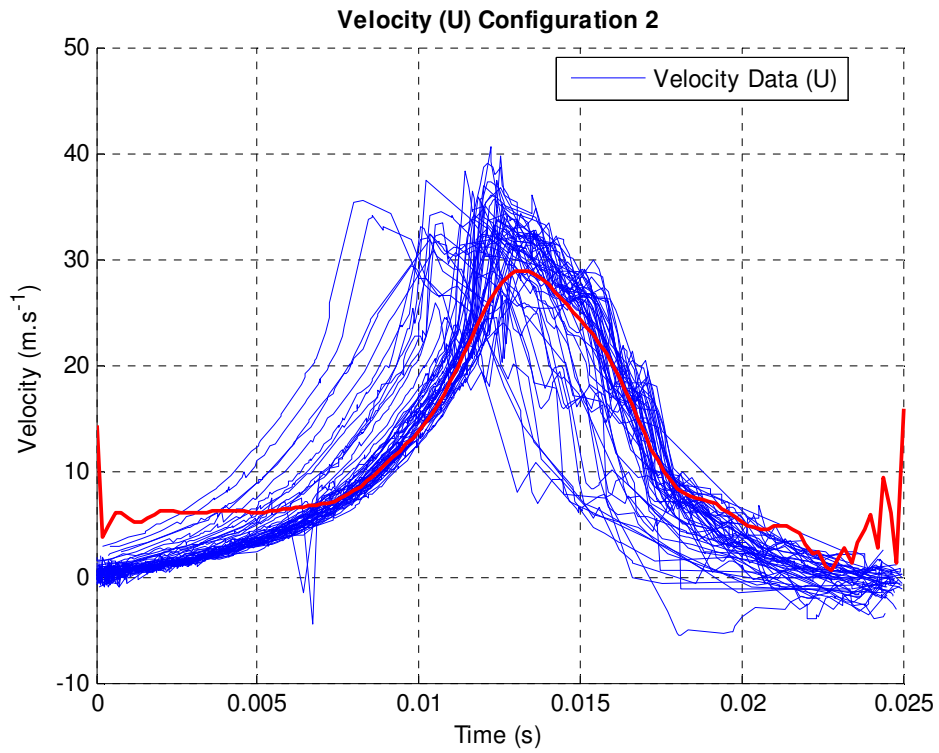
Figure F.3: Polynomial Order 30

APPENDIX G: LIF IMAGE EXPLANATION
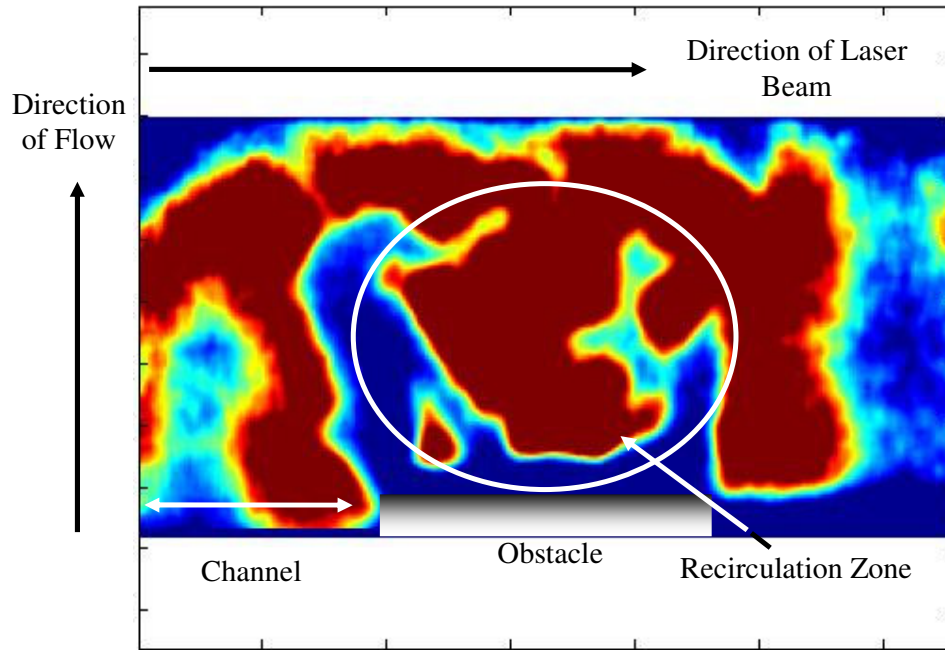
Figure G.1: Characteristics of a Typical LIF Image

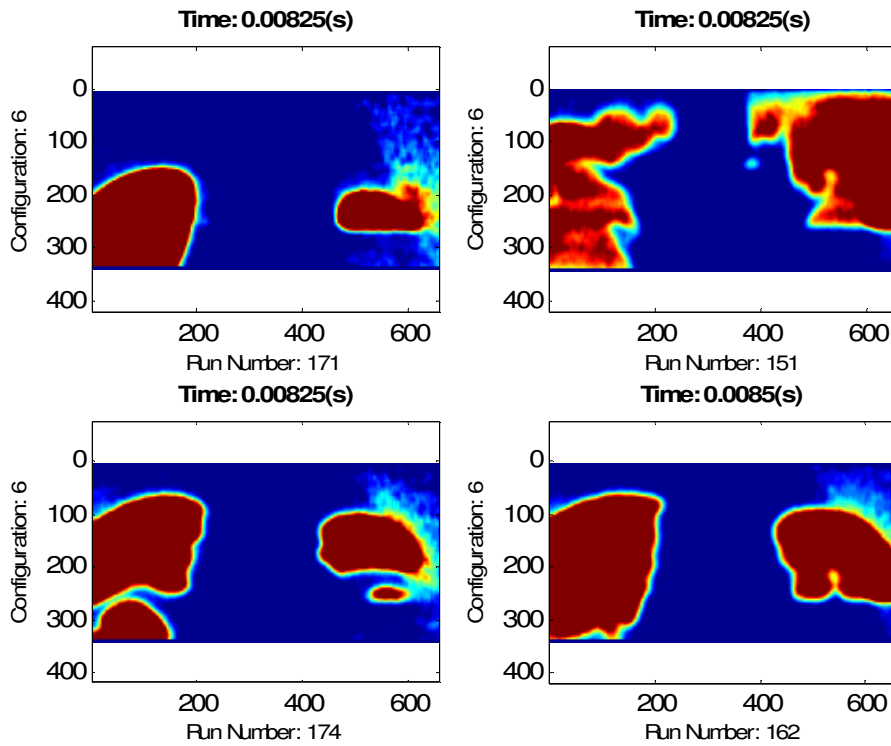# APPENDIX H: LIF IMAGES

H.1 LIF IMAGES FOR CONFIGURATION 2
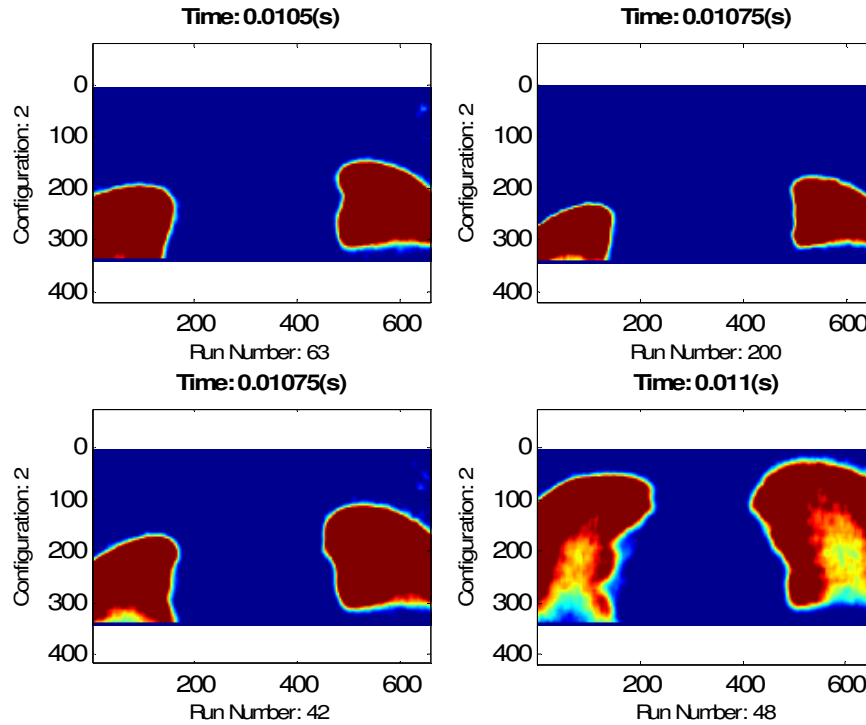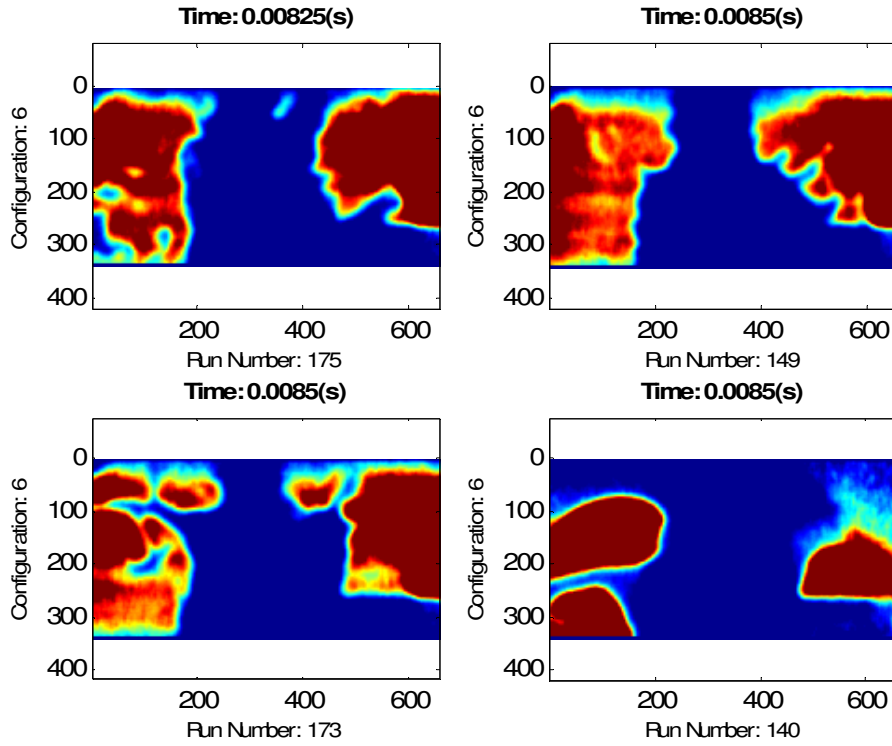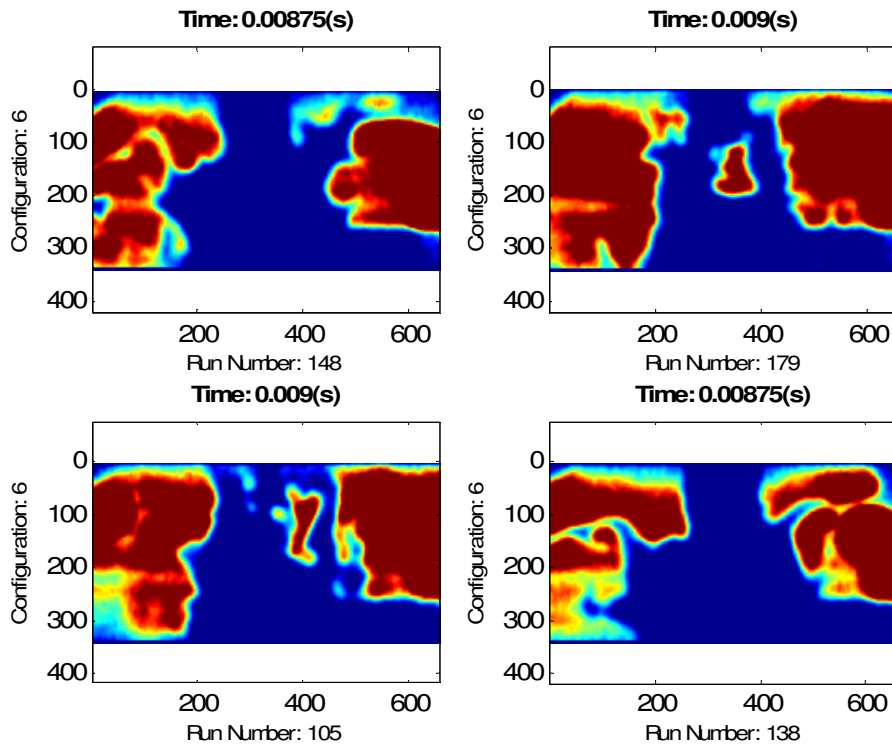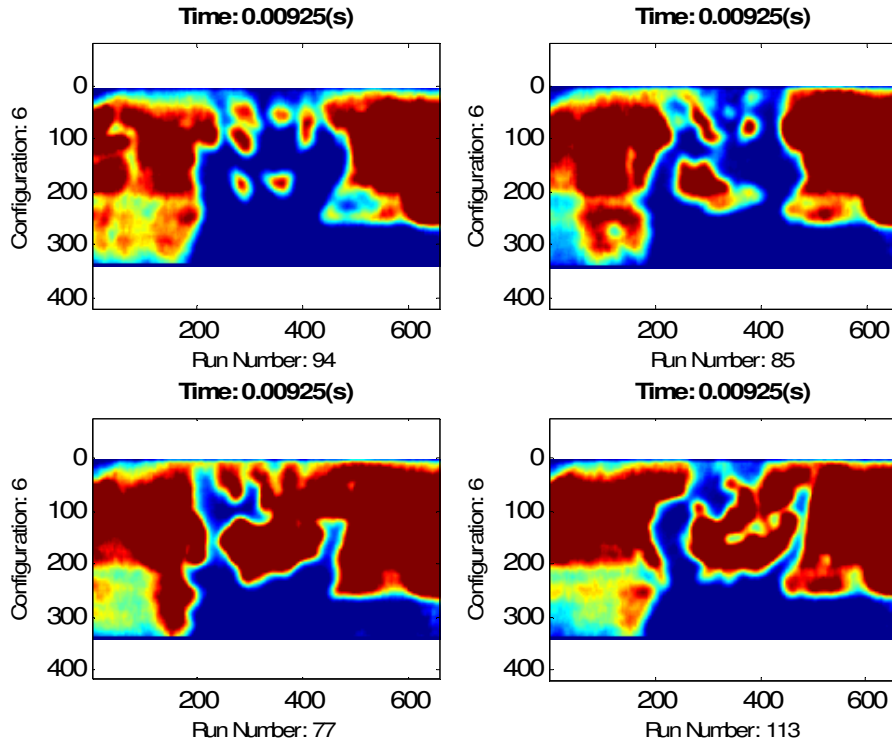

Figure H.1: LIF Images for Configuration 2; 1
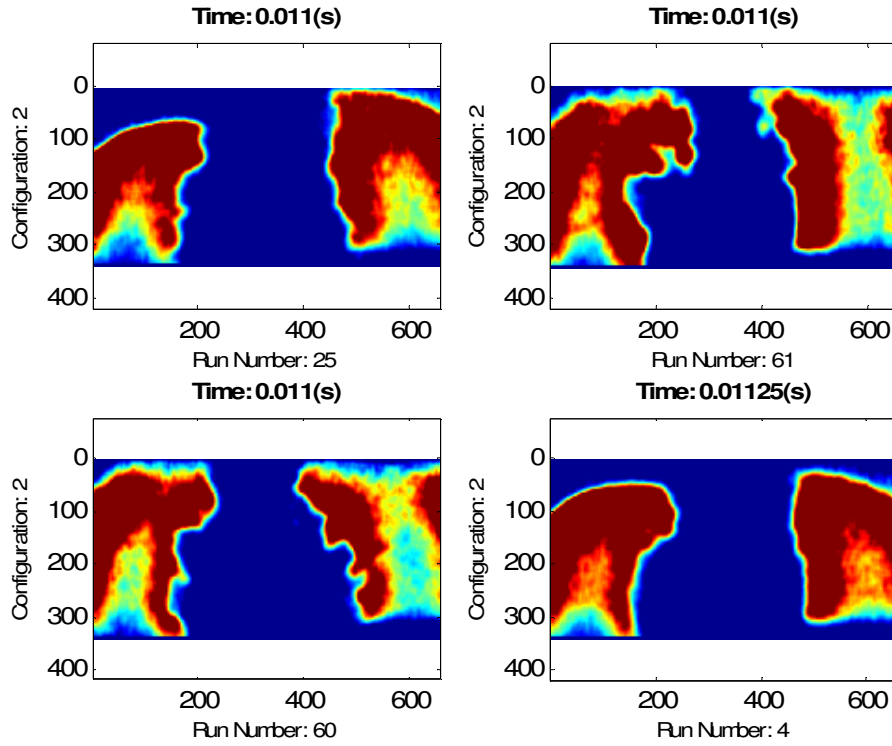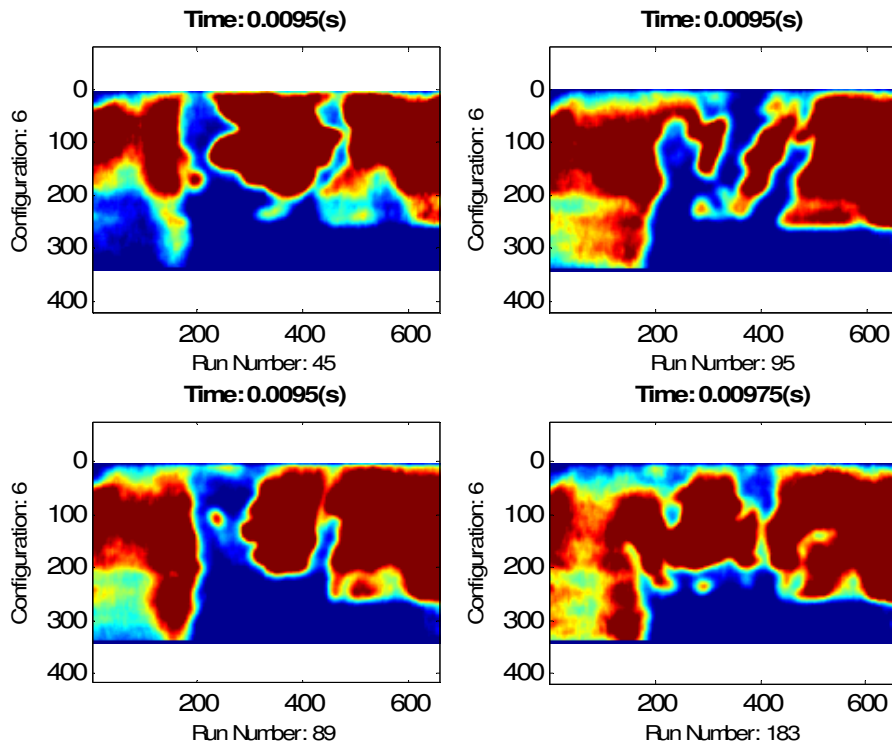
Figure H.2: LIF Images for Configuration 2; 2
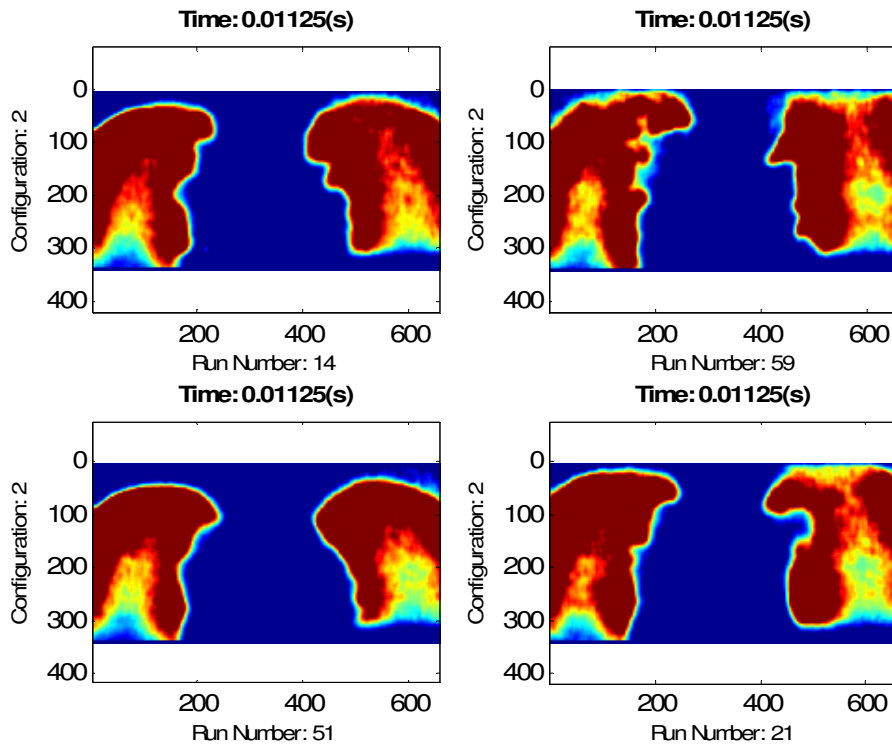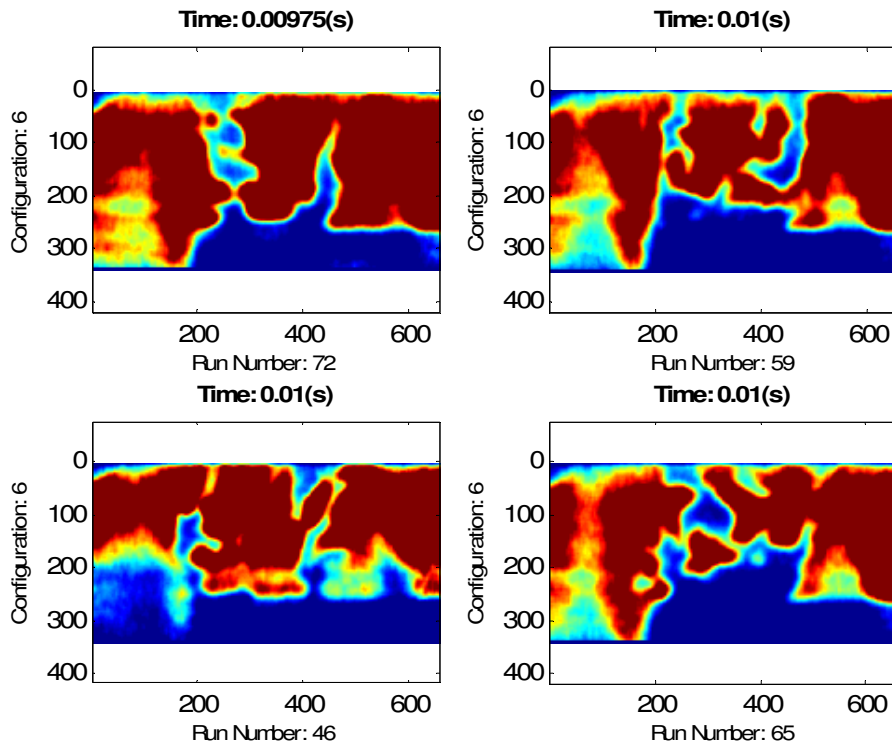

Figure H.3: LIF Images for Configuration 2; 3
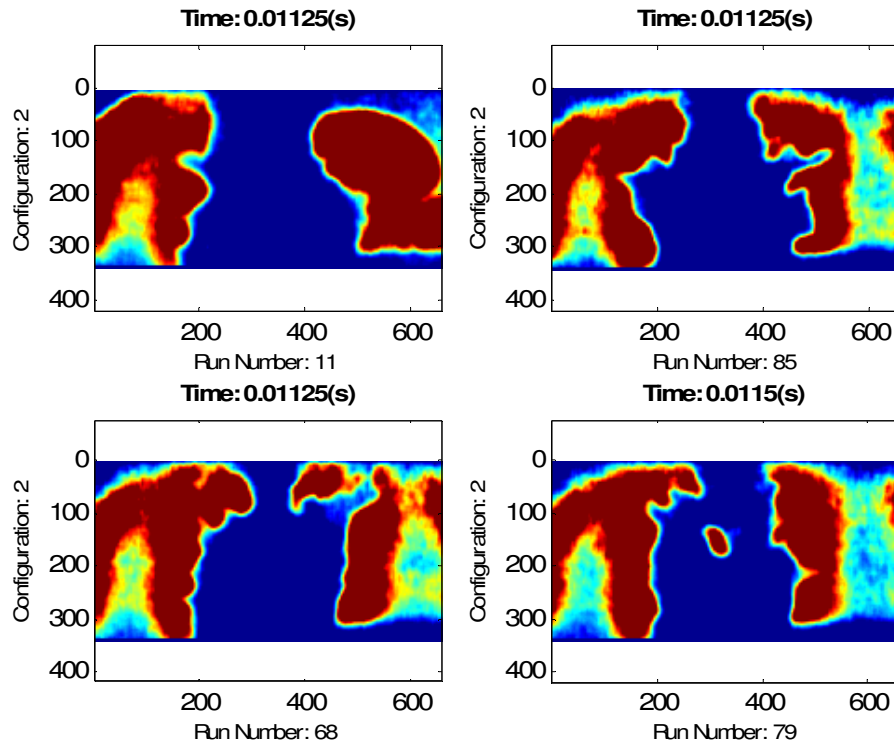
Figure H.4: LIF Images for Configuration 2; 4
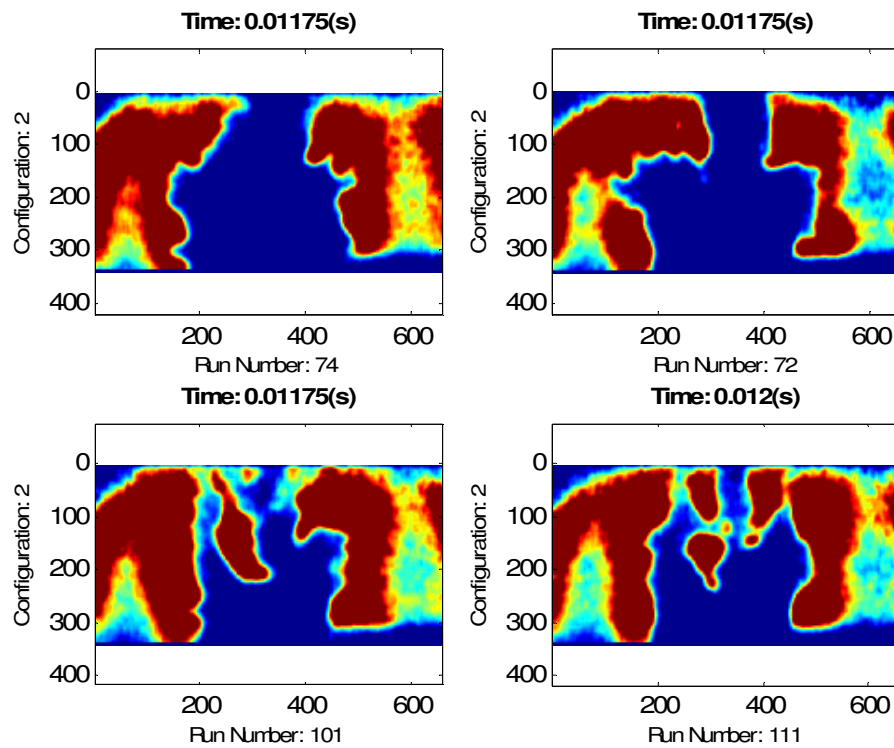
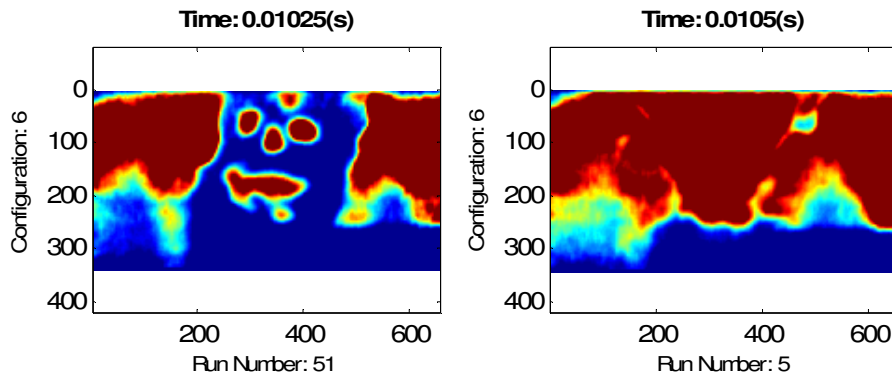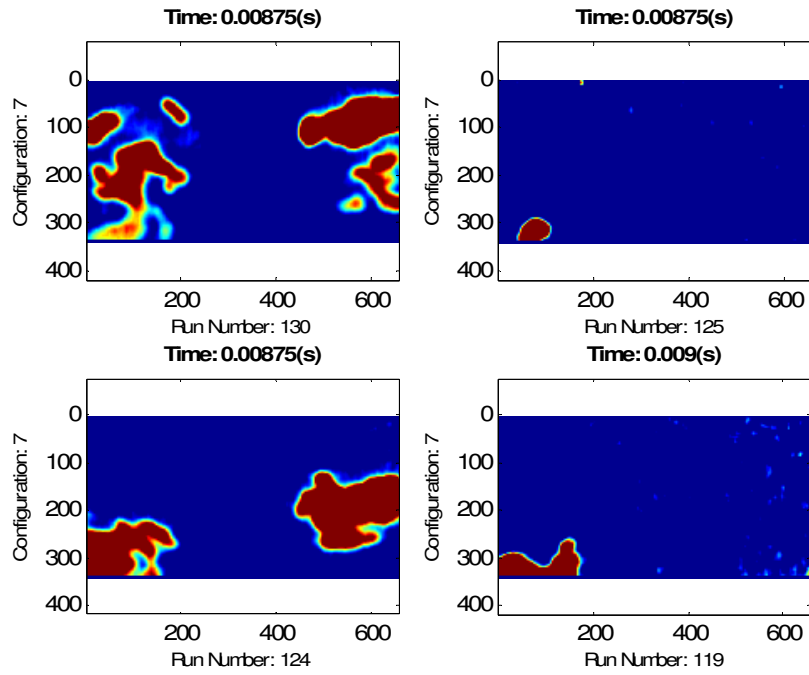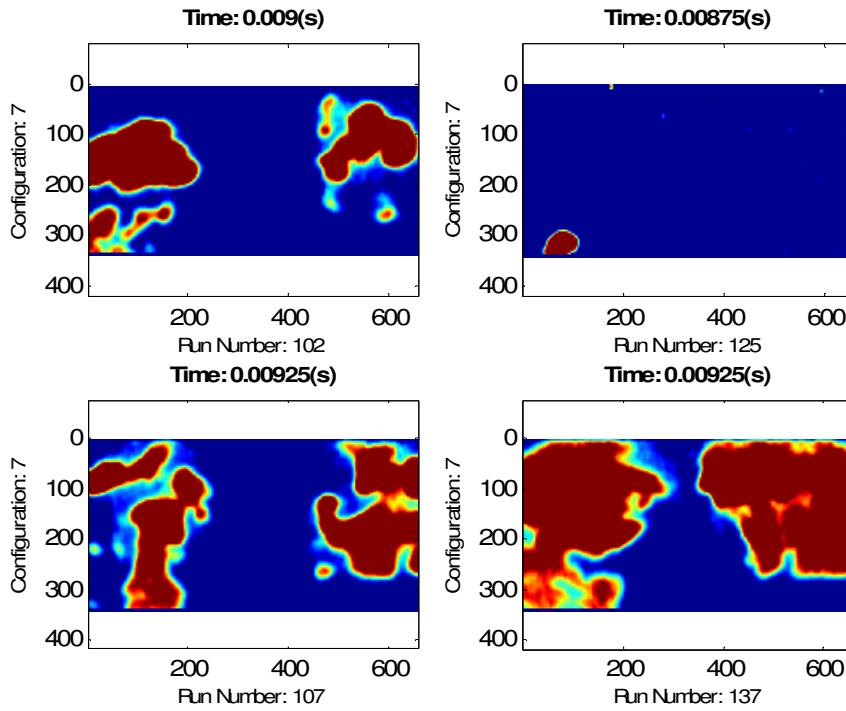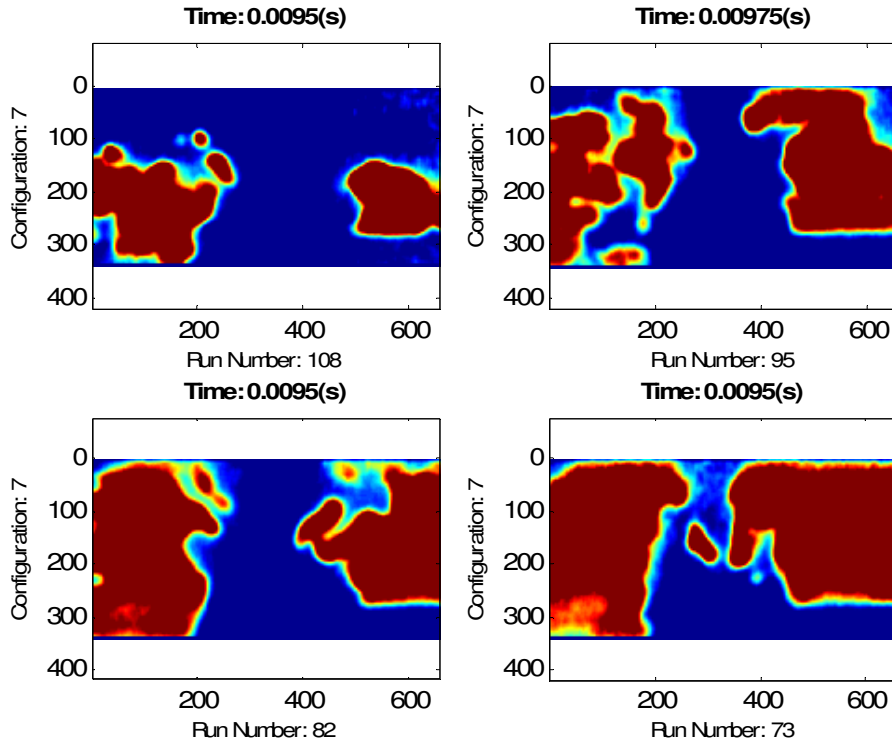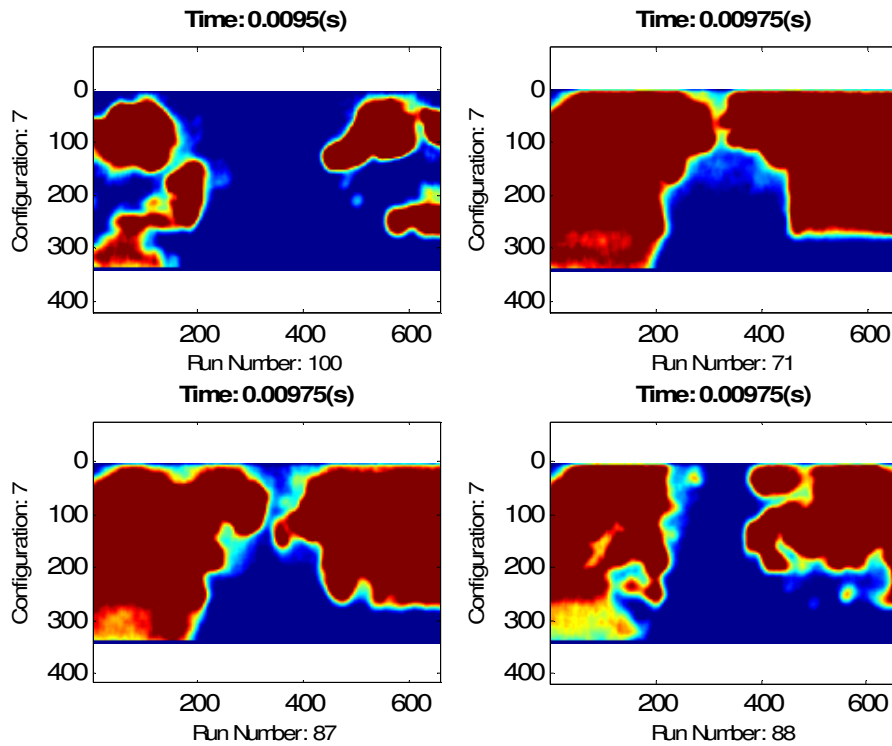Figure H.5: LIF Images for Configuration 2; 5
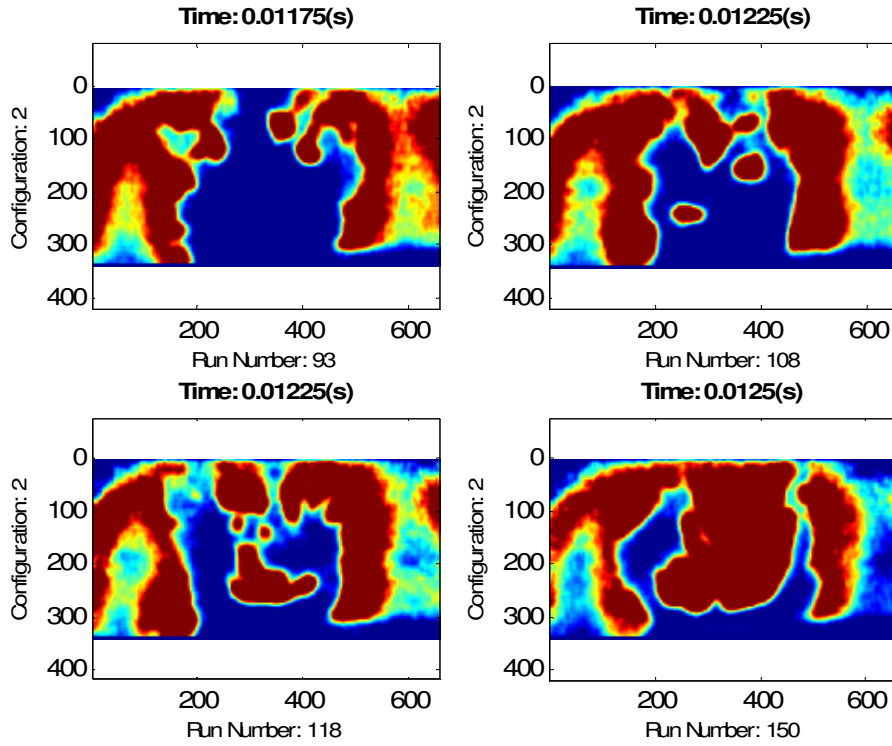
Figure H.6: LIF Images for Configuration 2; 6
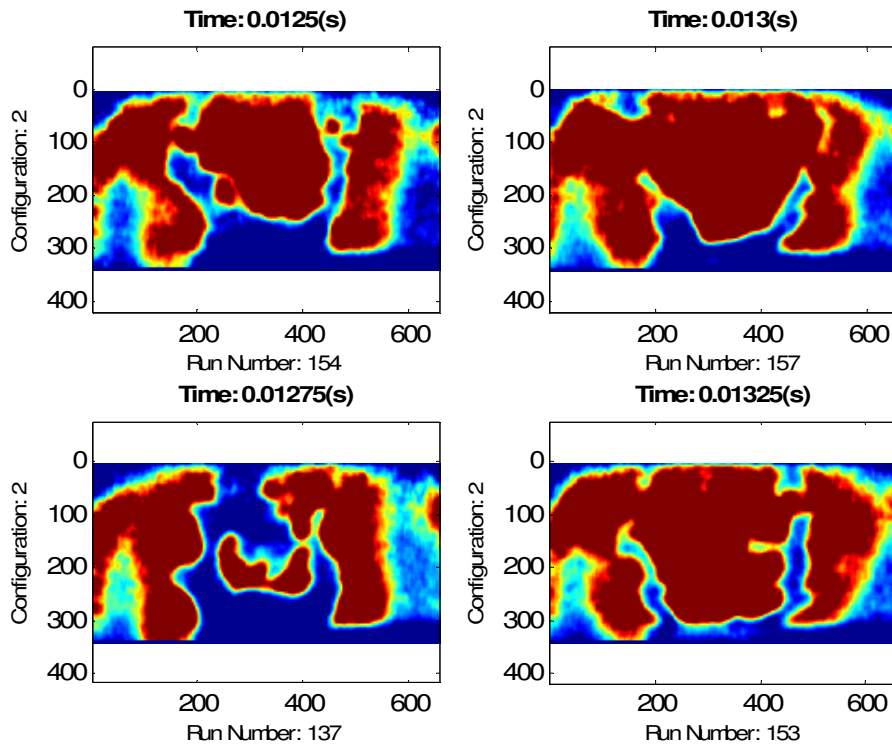
Figure H.7: LIF Images for Configuration 2; 7

Time: 0.01425(s)

Configuration: 2

Run Number: 196
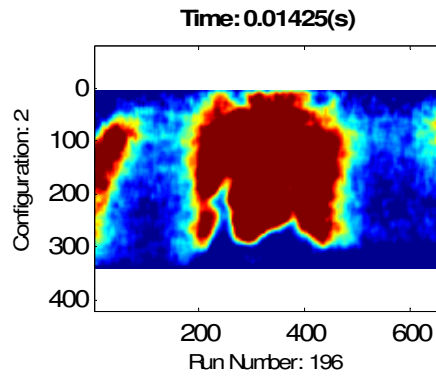
Figure H.8: LIF Images for Configuration 2; 8

H.2 LIF IMAGES FOR CONFIGURATION 6

Time: 0.00825(s)

Configuration: 6

Run Number: 171

Time: 0.00825(s)

Configuration: 6

Run Number: 151

Time: 0.00825(s)

Configuration: 6

Run Number: 174

Time: 0.0085(s)

Configuration: 6

Run Number: 162

Figure H.9: LIF Images for Configuration 6; 1

Time: 0.00825(s)

Time: 0.0085(s)

Run Number: 175

Run Number: 149

Time: 0.0085(s)

Time: 0.0085(s)

Run Number: 173

Run Number: 140

Figure H.10: LIF Images for Configuration 6; 2

Time: 0.00875(s)

Time: 0.009(s)

Run Number: 148

Run Number: 179

Time: 0.009(s)

Time: 0.00875(s)

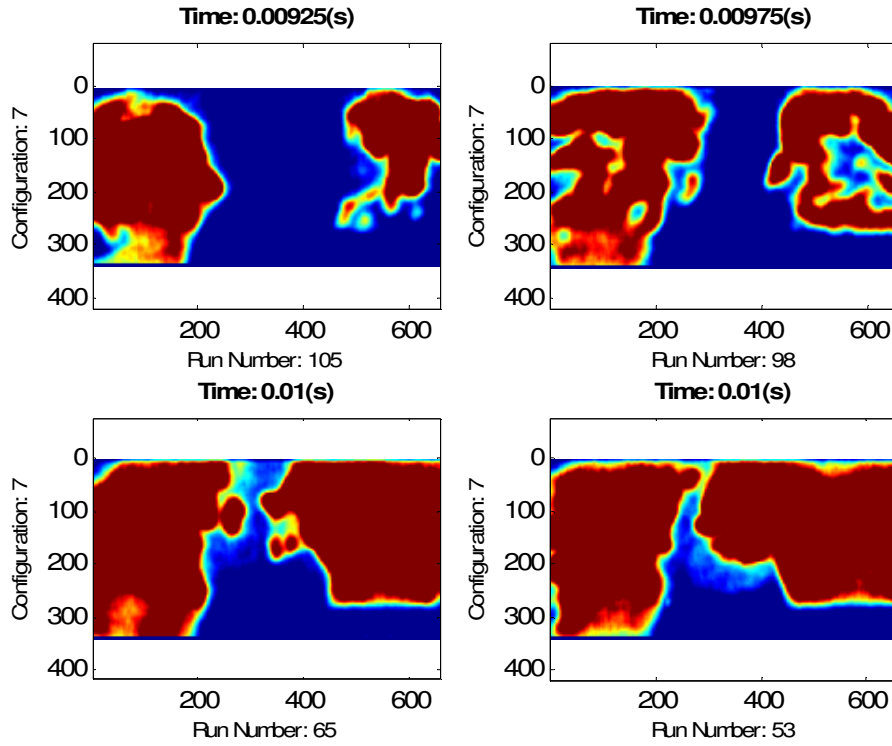Run Number: 105

Run Number: 138

Figure H.11: LIF Images for Configuration 6; 3

Figure H.12: LIF Images for Configuration 6; 4

Figure H.13: LIF Images for Configuration 6; 5
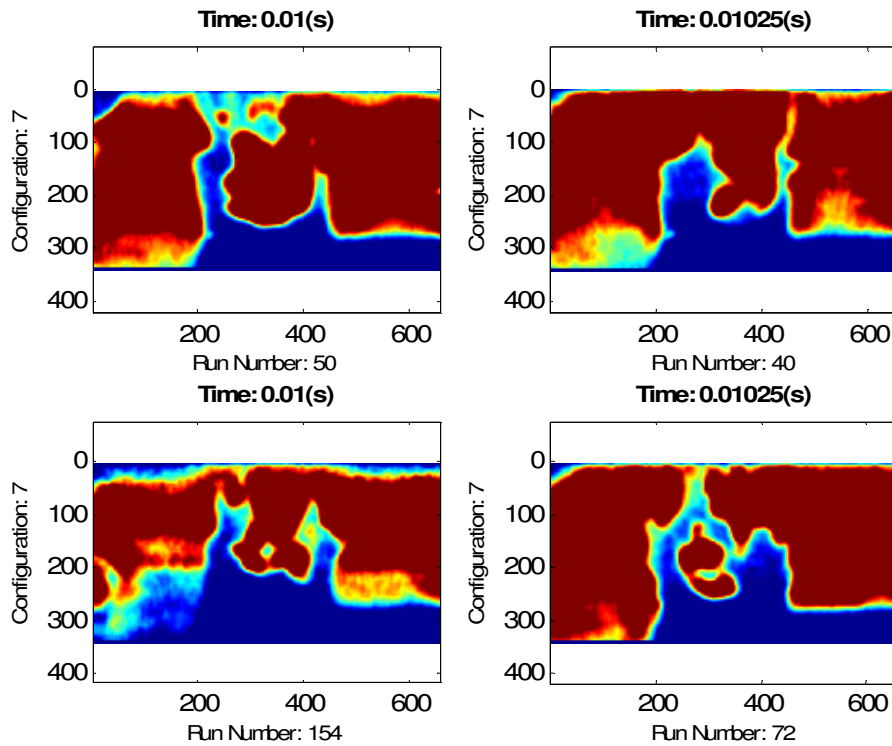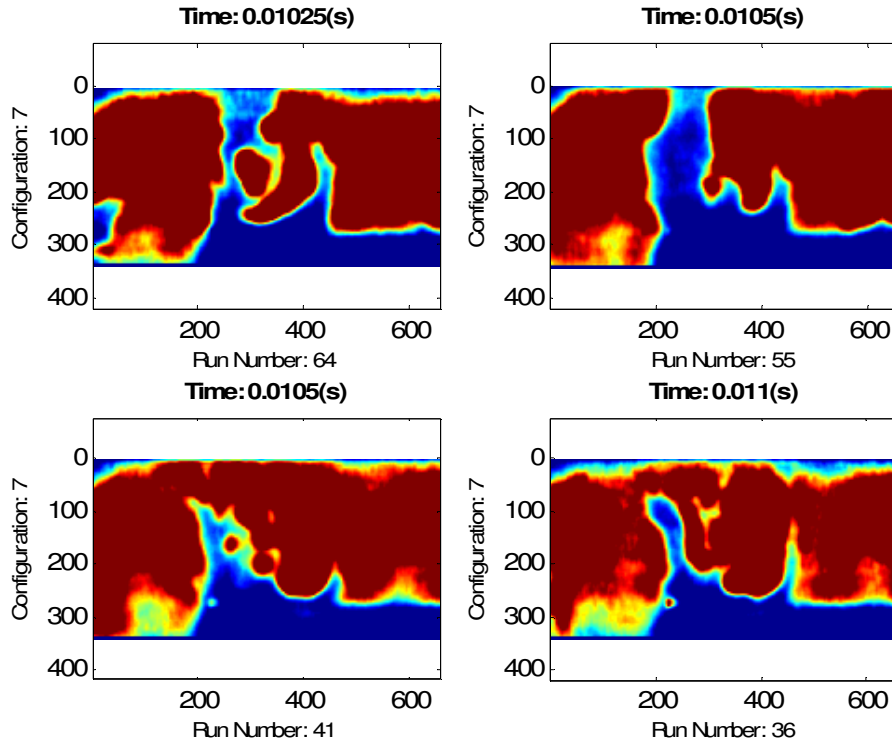
Time: 0.00975(s)

Configuration: 6

Run Number: 72

Time: 0.01(s)

Configuration: 6

Run Number: 59

Time: 0.01(s)

Configuration: 6

Run Number: 46

Time: 0.01(s)

Configuration: 6

Run Number: 65

Figure H.14: LIF Images for Configuration 6; 6

Time: 0.01025(s)

Configuration: 6

Run Number: 51

Time: 0.0105(s)

Configuration: 6

Run Number: 5

Figure H.15: LIF Images for Configuration 6; 7

H.3 LIF IMAGES FOR CONFIGURATION 7

Figure H.16: LIF Images for Configuration 7; 1

Figure H.17: LIF Images for Configuration 7; 2

Figure H.18: LIF Images for Configuration 7; 3
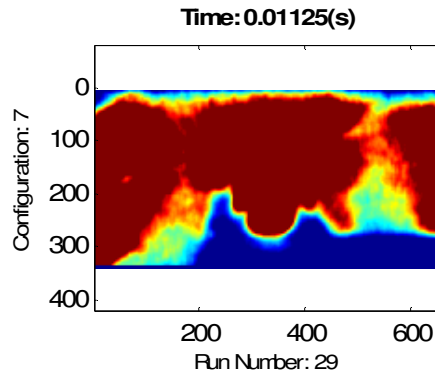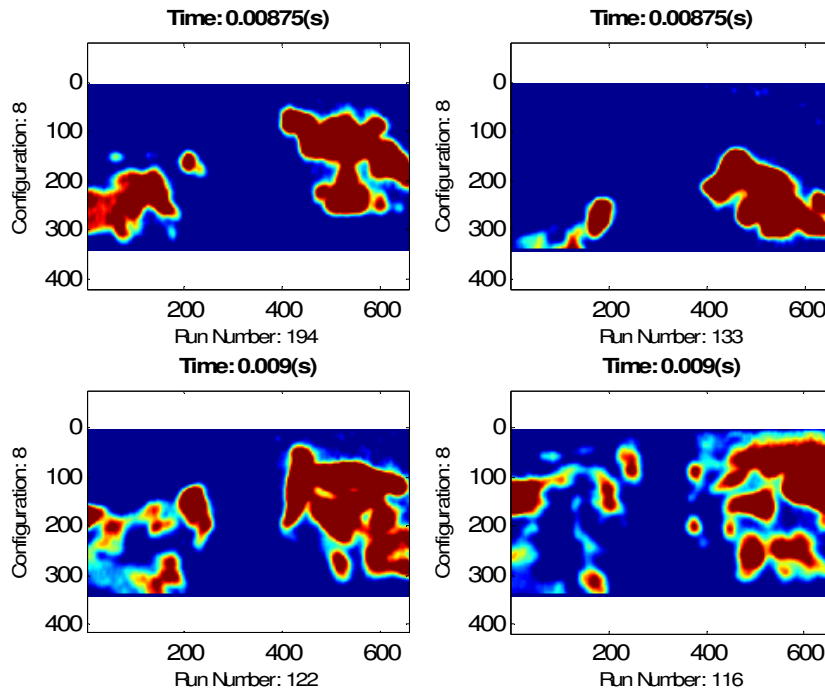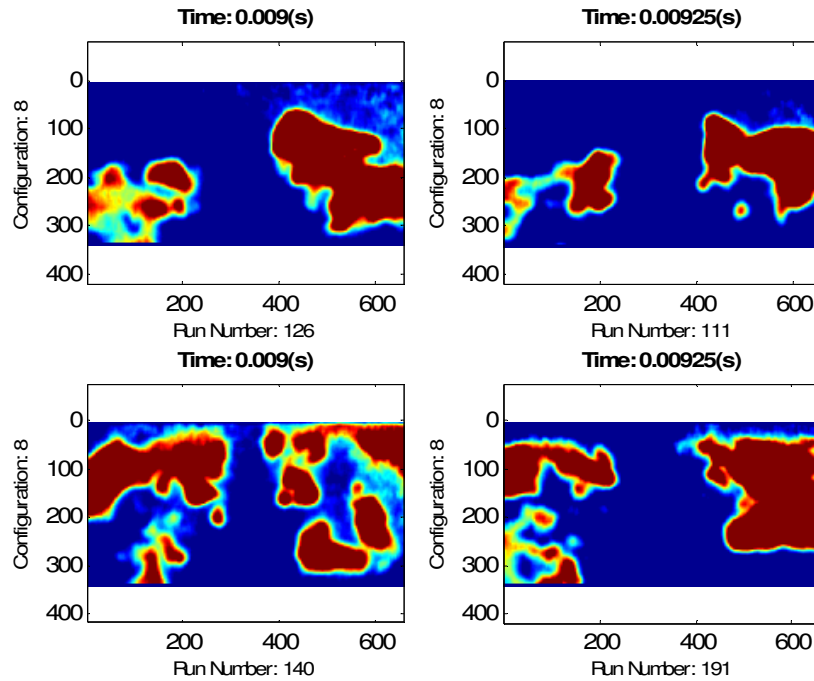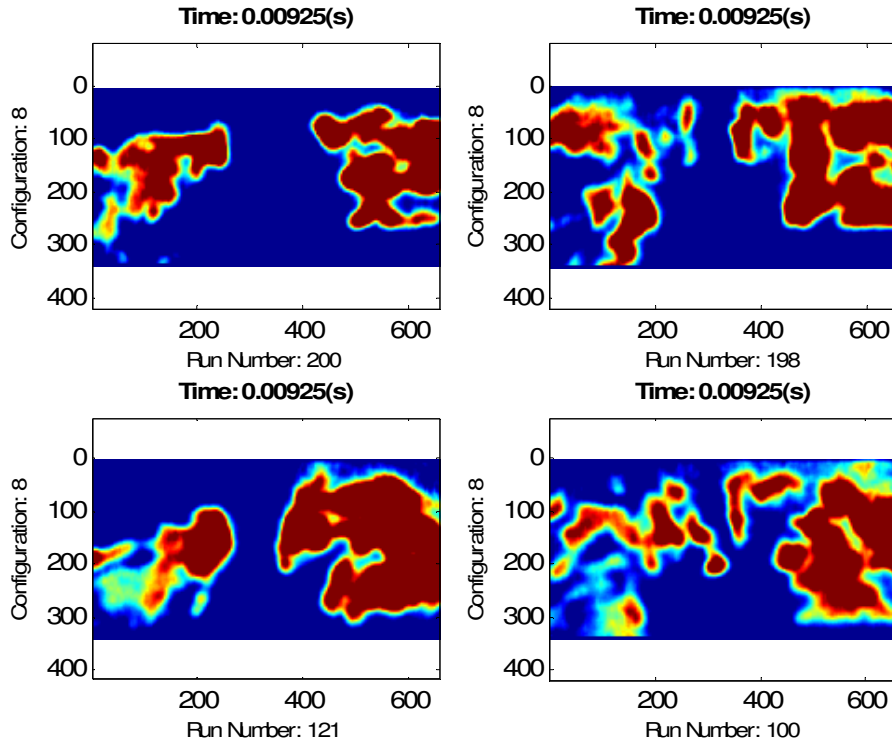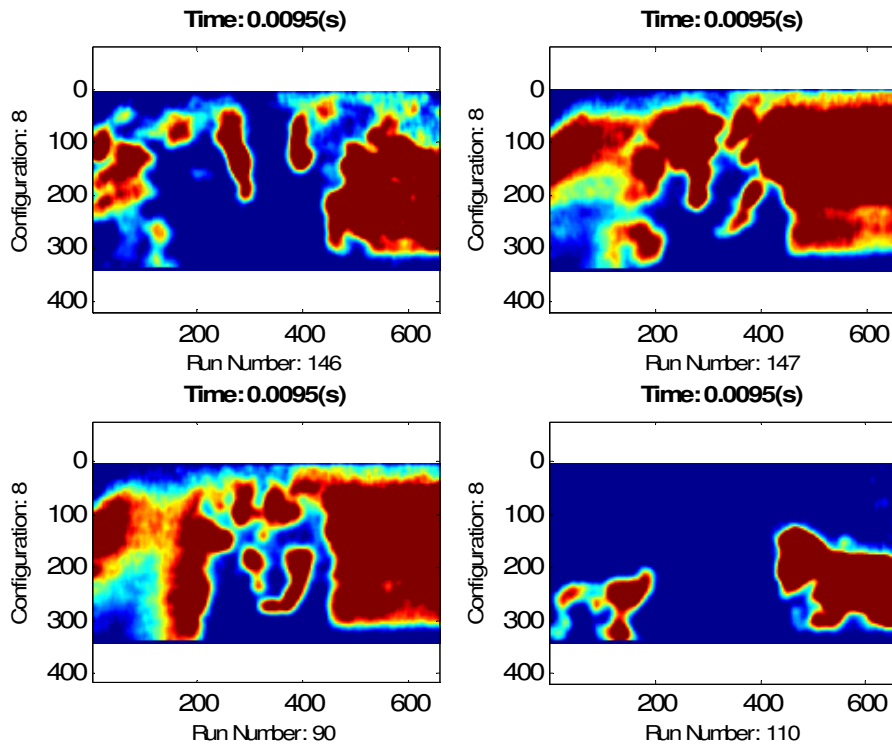
Figure H.19: LIF Images for Configuration 7; 4

Time: 0.00925(s)

Configuration: 7

Run Number: 105

Time: 0.00975(s)

Configuration: 7

Run Number: 98

Time: 0.01(s)

Configuration: 7

Run Number: 65

Time: 0.01(s)

Configuration: 7

Run Number: 53

Figure H.20: LIF Images for Configuration 7; 5

Time: 0.01(s)

Configuration: 7

Run Number: 50

Time: 0.01025(s)

Configuration: 7

Run Number: 40

Time: 0.01(s)

Configuration: 7

Run Number: 154

Time: 0.01025(s)

Configuration: 7

Run Number: 72

Figure H.21: LIF Images for Configuration 7; 6

Time: 0.01025(s)

Configuration: 7

Run Number: 64

Time: 0.0105(s)

Configuration: 7

Run Number: 55

Time: 0.0105(s)

Configuration: 7

Run Number: 41

Time: 0.011(s)

Configuration: 7

Run Number: 36

Figure H.22: LIF Images for Configuration 7; 7

Time: 0.01125(s)

Configuration: 7

Run Number: 29

Figure H.23: LIF Images for Configuration 7; 8

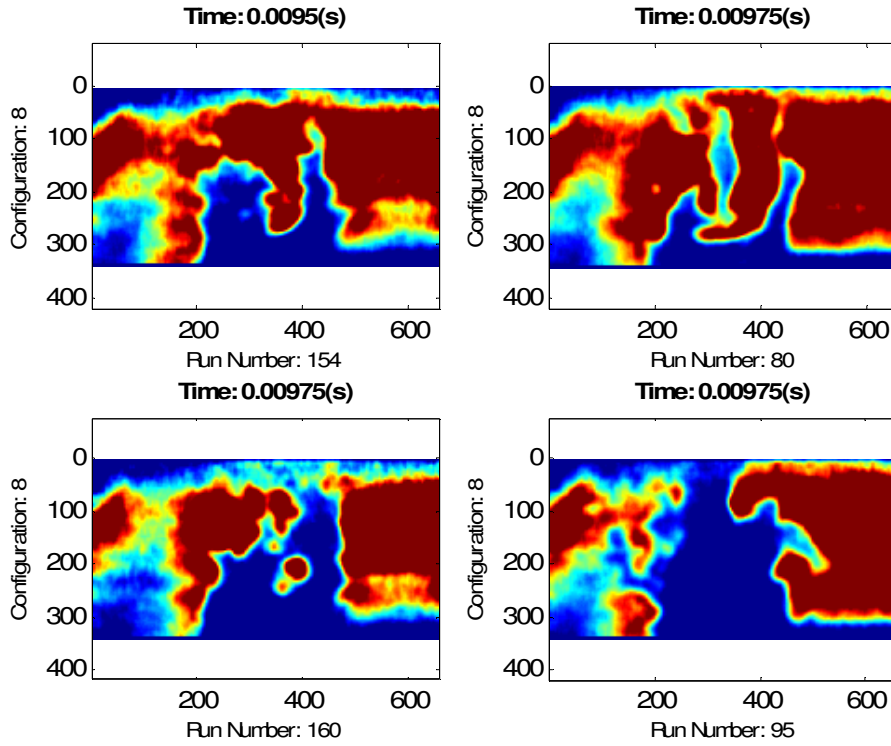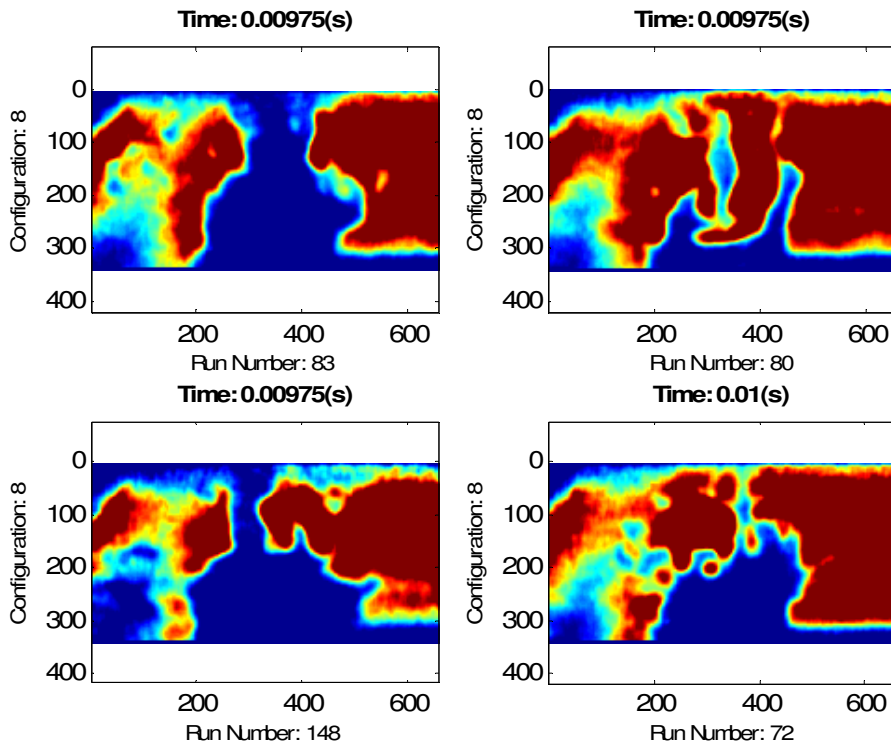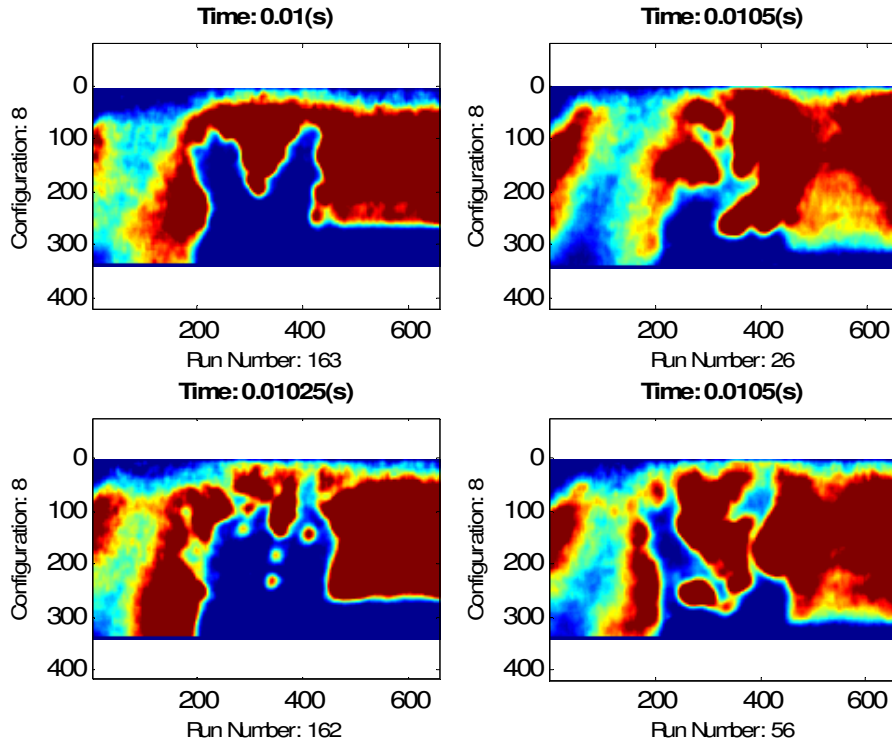## H.3 LIF IMAGES FOR CONFIGURATION 8

Figure H.24: LIF Images for Configuration 8; 1
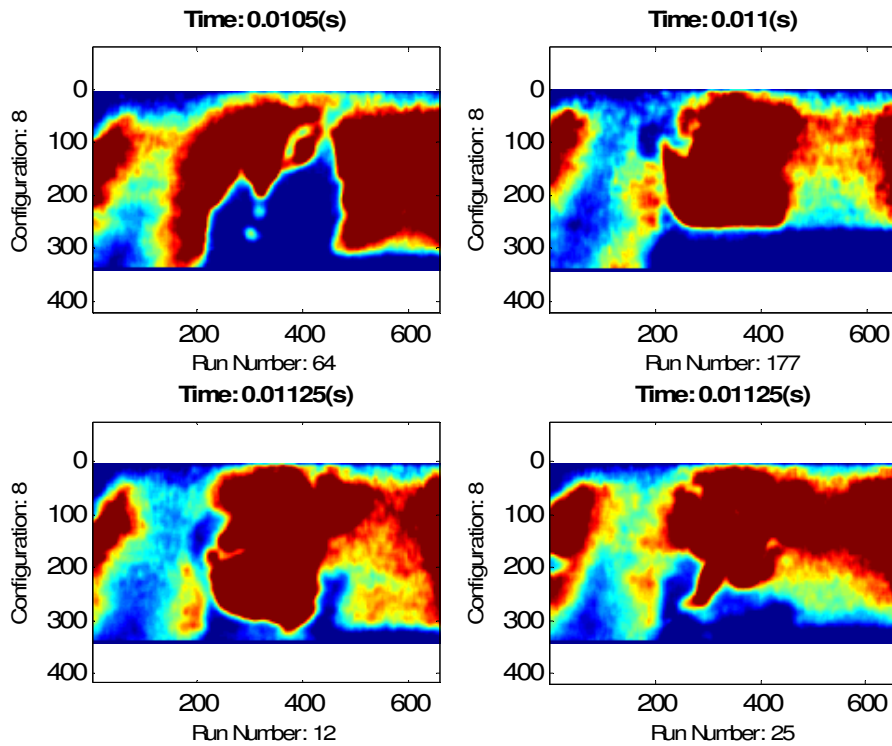

Figure H.25: LIF Images for Configuration 8; 2

Time: 0.00925(s)

Time: 0.00925(s)

Run Number: 200

Run Number: 198

Time: 0.00925(s)

Time: 0.00925(s)

Run Number: 121

Run Number: 100

Figure H.26: LIF Images for Configuration 8; 3

Time: 0.0095(s)

Time: 0.0095(s)

Run Number: 146

Run Number: 147

Time: 0.0095(s)

Time: 0.0095(s)

Run Number: 90

Run Number: 110

Figure H.27: LIF Images for Configuration 8; 4

Time: 0.0095(s)

Time: 0.00975(s)

Run Number: 154

Run Number: 80

Time: 0.00975(s)

Time: 0.00975(s)

Run Number: 160

Run Number: 95

Figure H.28: LIF Images for Configuration 8; 5

Time: 0.00975(s)

Time: 0.00975(s)

Run Number: 83

Run Number: 80

Time: 0.00975(s)

Time: 0.01(s)

Run Number: 148

Run Number: 72

Figure H.29: LIF Images for Configuration 8; 6

Time: 0.01(s)

Configuration: 8

Run Number: 163

Time: 0.0105(s)

Configuration: 8

Run Number: 26

Time: 0.01025(s)

Configuration: 8

Run Number: 162

Time: 0.0105(s)

Configuration: 8

Run Number: 56

Figure H.30: LIF Images for Configuration 8; 7

Time: 0.0105(s)

Configuration: 8

Run Number: 64

Time: 0.011(s)

Configuration: 8

Run Number: 177

Time: 0.01125(s)

Configuration: 8

Run Number: 12

Time: 0.01125(s)

Configuration: 8

Run Number: 25

Figure H.31: LIF Images for Configuration 8; 8

Time: 0.0115(s)
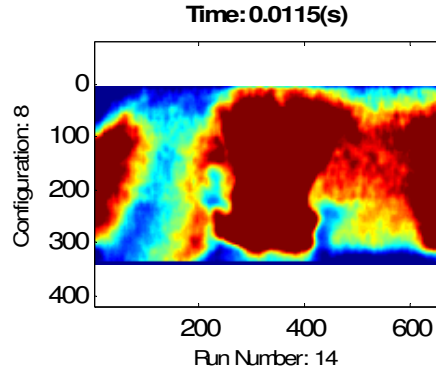
Figure H.32: LIF Images for Configuration 8; 9

H.5 LIF IMAGES FOR CONFIGURATION 9

Time: 0.0075(s)

Time: 0.00775(s)

Time: 0.008(s)

Time: 0.008(s)
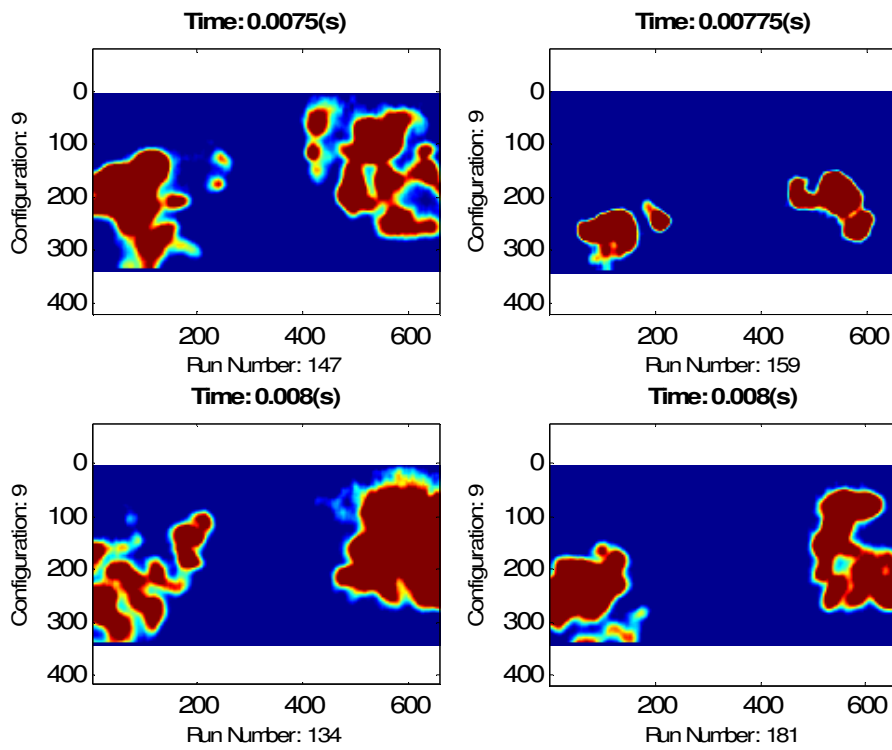
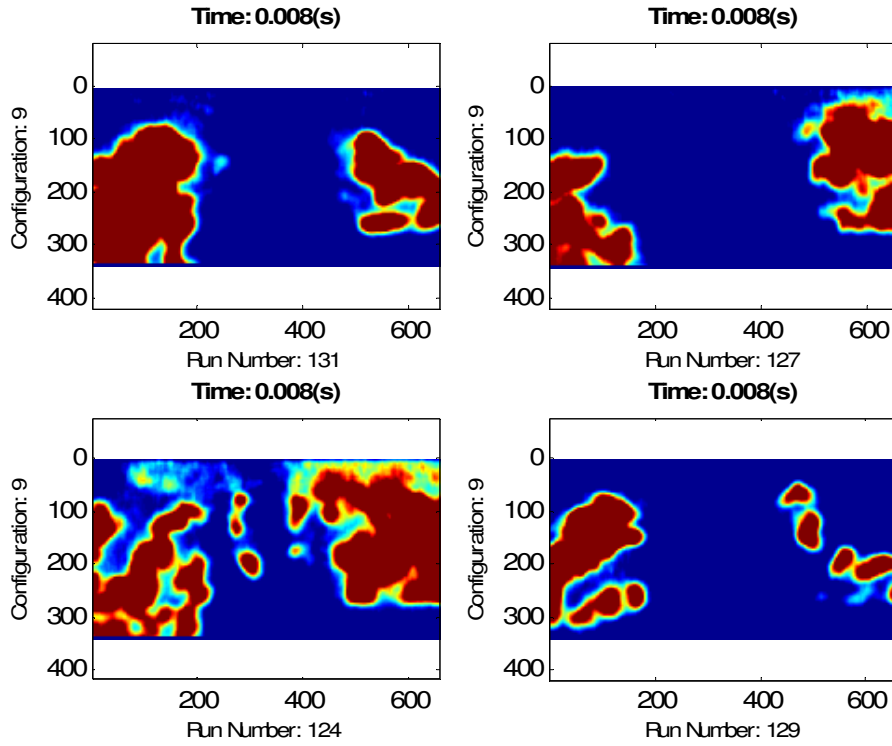Figure H.33: LIF Images for Configuration 9; 1
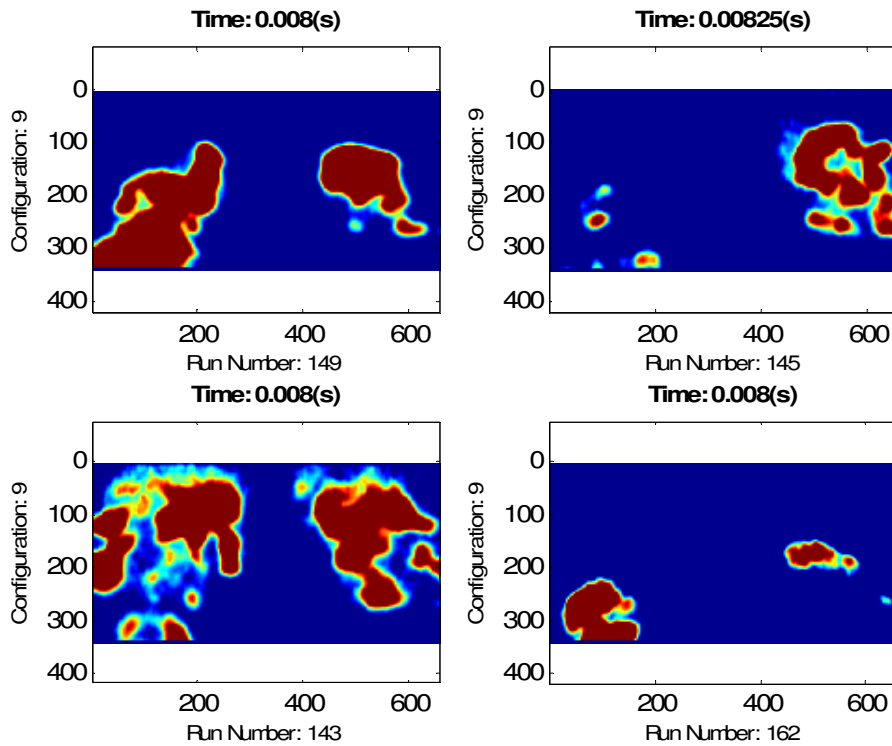
Figure H.34: LIF Images for Configuration 9; 2
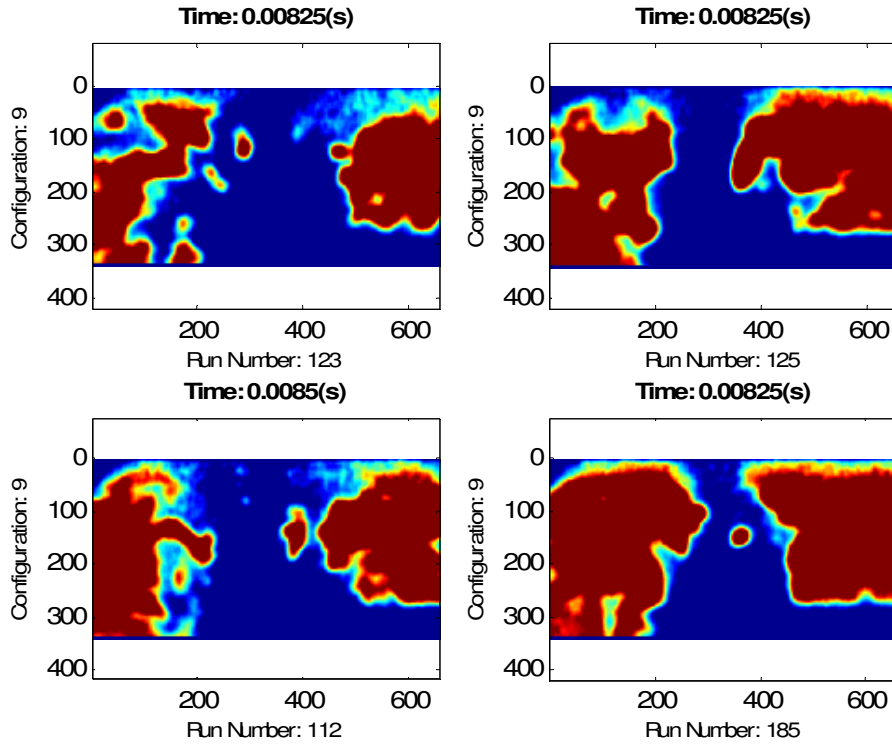

Figure H.35: LIF Images for Configuration 9; 3
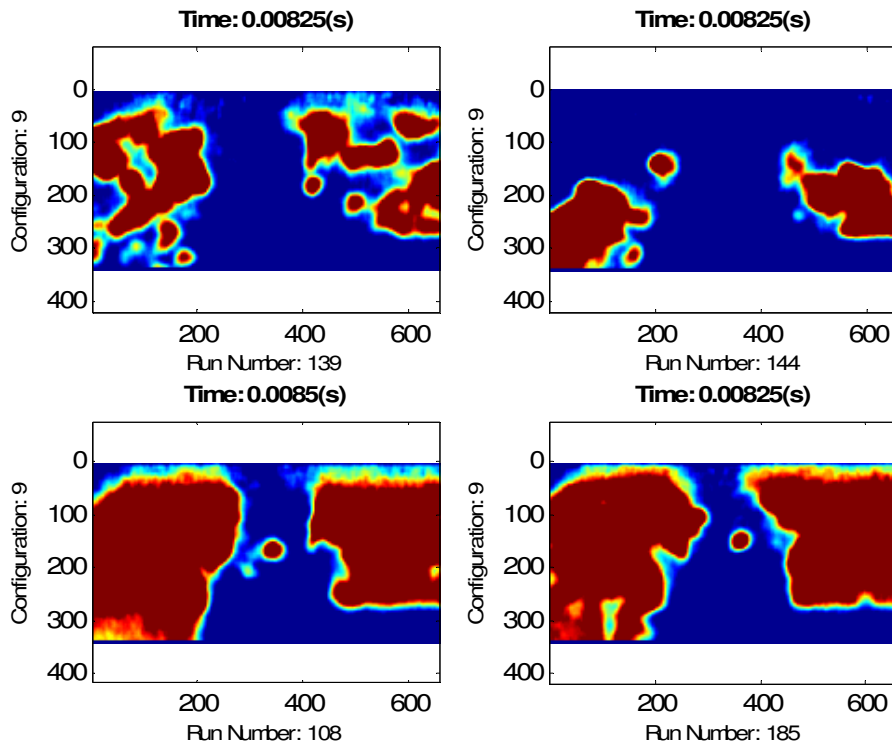
Figure H.36: LIF Images for Configuration 9; 4

Figure H.37: LIF Images for Configuration 9; 5
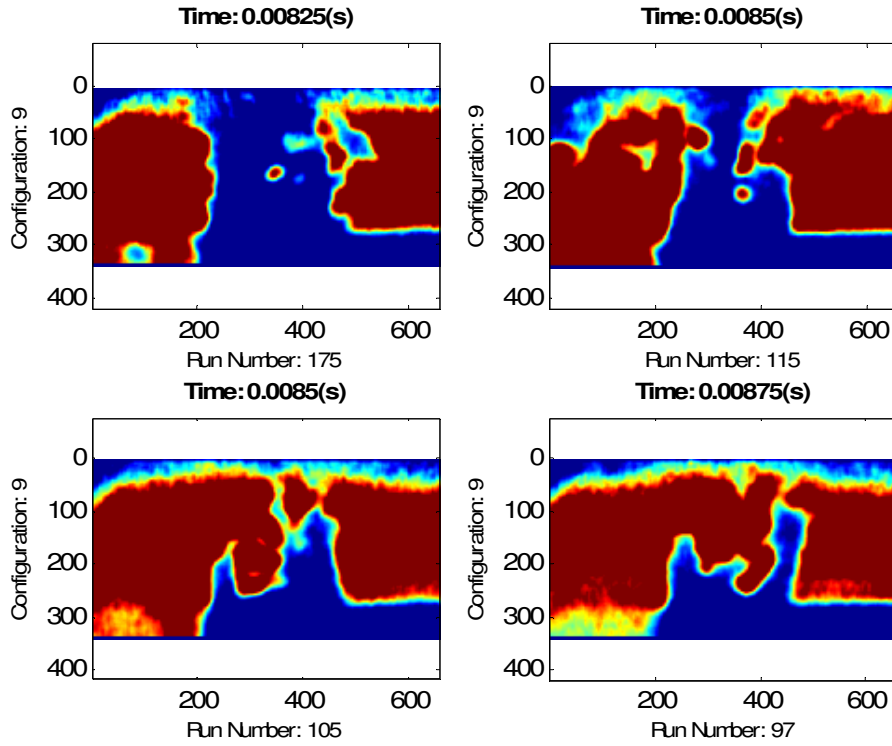
Time: 0.00825(s)

Time: 0.0085(s)

Run Number: 175

Run Number: 115

Time: 0.0085(s)

Time: 0.00875(s)

Run Number: 105

Run Number: 97

Figure H.38: LIF Images for Configuration 9; 6

Time: 0.00875(s)

Time: 0.009(s)

Run Number: 193

Run Number: 78

Time: 0.009(s)
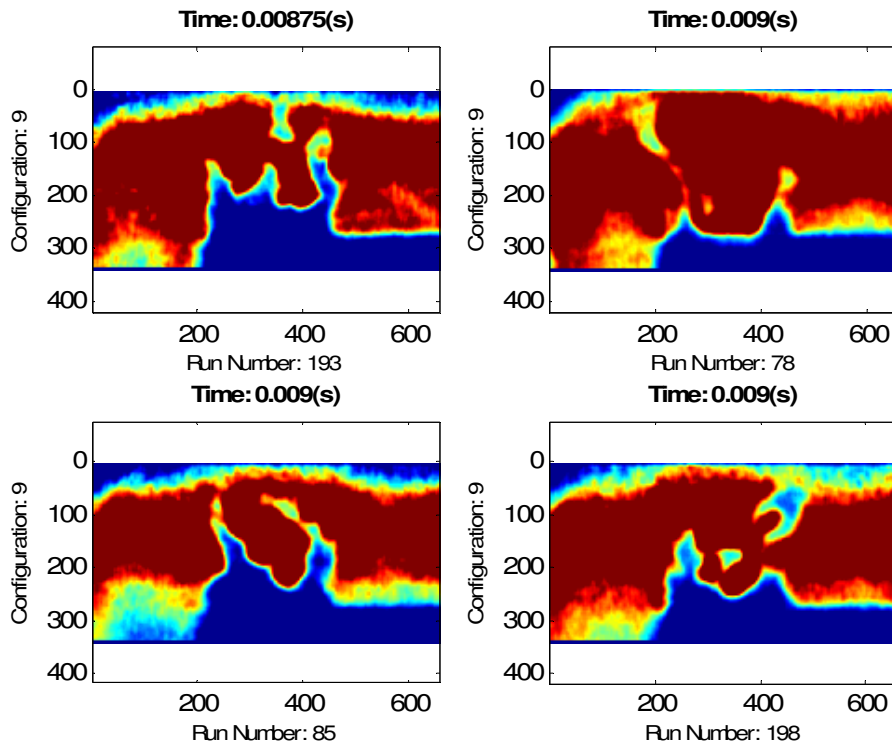
Time: 0.009(s)

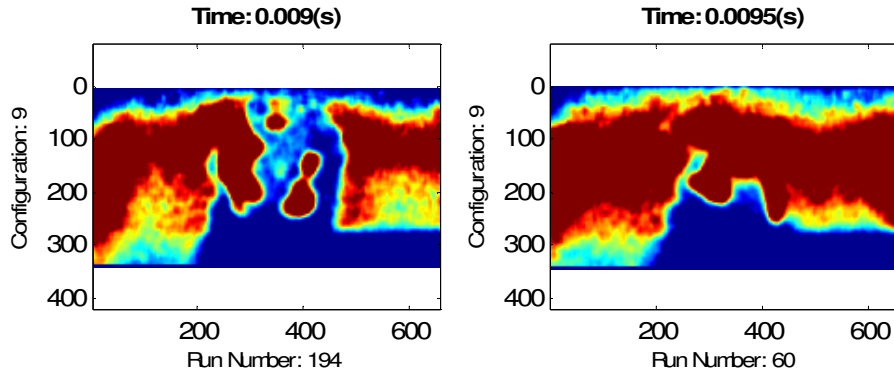Run Number: 85

Run Number: 198

Figure H.39: LIF Images for Configuration 9; 7

Figure H.40: LIF Images for Configuration 9; 8